Hadron muoproduction at the COMPASS experiment

Jean-François Rajotte



München 2010

Hadron muoproduction at the COMPASS experiment

Jean-François Rajotte

Dissertation an der Fakultät für Physik der Ludwig–Maximilians–Universität München

> vorgelegt von Jean-François Rajotte aus Sherbrooke, Kanada

München, den 4. August 2010

Erstgutachter: Prof. Dr. M. Faessler Zweitgutachter: Prof. Dr. O. Biebel Tag der mündlichen Prüfung: 30. September 2010

À ma famille

Contents

Li	List of Figures ix			
\mathbf{Li}	st of	Tables	xiii	ί
Sı	Summary xv			
1	Intr	oducti	on 1	
2	The	COM	PASS experiment 5	ý
	2.1	Physic	s goals of COMPASS 5)
		2.1.1	Physics with the muon beam)
		2.1.2	Physics with the hadron beam	3
		2.1.3	Future physics 8	;
3	Exp	erimer	ital setup 11	-
	3.1	Spectre	ometer overview	_
		3.1.1	Beam 11	_
		3.1.2	Target	2
		3.1.3	Magnets	;
		3.1.4	Tracking detectors	;
		3.1.5	Calorimeters)
		3.1.6	Muon walls	;
		3.1.7	RICH 16	j
		3.1.8	Trigger system	j
		3.1.9	Data acquisition system)
		3.1.10	Data reconstruction	
	3.2	The st	raw drift chambers	,
		3.2.1	General concept	Ŀ
		3.2.2	Components)
		3.2.3	The front-end cooling system	;
		3.2.4	Drift time calibration)

4	The	eoretical framework	33
	4.1	Deep inelastic scattering	33
		4.1.1 Basic variables	34
		4.1.2 Elastic scattering	35
		4.1.3 Muon-hadron scattering	39
		4.1.4 Cross sections	39
		4.1.5 QED radiative effects	43
		4.1.6 The Quark Parton Model	44
		4.1.7 Polarized deep inelastic scattering	46
	4.2	Semi-inclusive deep inelastic scattering	49
		4.2.1 Intrinsic transverse momentum of partons	49
		4.2.2 Gaussian ansatz	52
5	Cor	rection for acceptance	55
	5.1	Monte Carlo simulation	55
		5.1.1 The LEPTO Generator	56
		5.1.2 Spectrometer simulation with COMGEANT	57
	5.2	Correction method	57
	5.3	Reproduction of the simulated distribution	61
	5.4	Direct and tabulated acceptance comparison	69
c	Det	commination of the inclusive differential energy section	75
6		termination of the inclusive differential cross section	75 75
	$6.1 \\ 6.2$	Luminosity	75 78
	0.2 6.3	Data sample	70 79
		Measured data and Monte Carlo comparison	79 86
	6.4	Cross section	80 89
	6.5 6.6	Structure function F_2	
	6.6		90
	6.7	F_2 comparison with SMC	93
7	Sen	ni-inclusive differential cross section hadron production	95
	7.1	The data samples	96
	7.2	Real data and Monte Carlo comparison	96
	7.3	Comparison with EMC	100
	7.4	Energy dependence of $\langle p_T^2 \rangle$	103
	7.5	Fit of the cross sections	105
		7.5.1 Dependence of $\langle p_T^2 \rangle$ on the hadron energy fraction z	121
		7.5.2 Dependence of $\langle k_{\perp}^2 \rangle$ on inclusive variables	121
8	Cor	nclusion and outlook	131
\mathbf{A}	F_2 c	comparison period by period	133
в	Info	prmation about the inclusive cross section	141

Table of Contents	ix
C Fit tables	145
D Acronyms and Abbreviations	157
Bibliography	159
Danksagung	164

List of Figures

2.1	Basic photon quark and gluon interactions	6
3.1	Concept of the trigger combining hodoscope and hadronic calorimeter	17
3.2	Position of the trigger components.	18
3.3	Schematic layout of the veto system	19
3.4	Overview of the DAQ system.	21
3.5	Schematic representation of the COMPASS reconstruction software	22
3.6	Charged particle crossing a straw and ionizing the gas along its path	24
3.7	Schematic view of a COMPASS straw drift chamber (type X)	25
3.8	Cross section of a double layer	26
3.9	Lateral cross section of the bottom of a straw drift chamber	27
3.10	Conceptual drawing of the straw cooling system	29
3.11	Detailed drawing of the straw cooling system.	30
3.12	Elements of a cooling unit of the straw cooling system	31
3.13	Picture of a cooling plate.	31
4.1	Feynman diagram of deep inelastic scattering	33
4.2	Feynman diagram of elastic muon-electron scattering	36
4.3	Point-like cross section compared to electron-proton scattering	38
4.4	Structure function $F_2(x_{Bj}, \hat{Q}^2)$.	42
4.5	R determined by NMC.	44
4.6	Lowest order QED radiative processes	45
4.7	Electron-proton scattering cross section.	47
4.8	DIS diagram with parton with intrinsic transverse momentum	50
4.9	DIS diagram with hadronization.	51
5.1	Acceptance tables.	58
5.2	Reproduction of MC inclusive distributions (ALL trigger).	63
5.3	Reproduction of MC inclusive distributions (inclMT).	64
5.4	Reproduction of MC inclusive distributions for x_{Bi} bins (ALL triggers)	65
5.5	Ratio of reproduced MC inclusive distributions for x_{Bi} bins (ALL triggers).	65
5.6	Reproduction of MC inclusive distributions for x_{Bi} bins (inclMT)	66
5.7	Ratio of reproduced MC inclusive distributions for x_{Bi} bins (inclMT)	66

5.8	Reproduction of MC hadron distributions within acceptance limits	67
5.9	Reproduction of MC hadron distributions	67
5.10	Hadron distributions and acceptance limits	68
5.11	Inclusive acceptance for ALL trigger	70
	Inclusive acceptance for inclusive middle trigger	71
5.13	MC generated and reconstructed inclusive distributions for ALL triggers .	72
5.14	Direct and tabulated inclusive acceptance comparison for ALL triggers	72
5.15	MC generated and reconstructed inclusive distributions for inclMT	73
5.16	Direct and tabulated inclusive acceptance comparison for inclMT	73
5.17	Direct and tabulated hadron acceptance comparison	74
6.1	Measured data distributions for ALL trigger	80
6.2	Measured data distributions for inclMT	81
6.3	Measured data vs MC for ALL triggers	82
6.4	Measured data vs MC for inclMT	83
6.5	Measured data vs MC for x_{Bj} bins (ALL triggers)	84
6.6	Real data and MC ratio for x_{Bj} bins (inclMT)	84
6.7	Measured data vs MC for x_{Bj} bins (inclMT)	85
6.8	Real data and MC ratio for x_{Bj} bins (inclMT)	85
6.9	COMPASS inclusive cross section (ALL triggers)	86
6.10		87
	COMPASS inclusive cross section for analysis bins (ALL triggers)	87
	COMPASS inclusive cross section for analysis bins (inclMT)	88
	η factor and COMPASS $\sigma_{1\gamma}$ (inclMT)	91
6.14	η factor for analysis bins (inclMT)	92
6.15	COMPASS $\sigma_{1\gamma}$ for analysis bins (inclMT)	92
	Structure function comparison for inclMT	93
6.17	$\frac{F_2^{\rm COMP}}{F_2^{\rm SMC}} \text{ for inclMT} \dots \dots$	94
	2	07
7.1	Event distributions and inclusive bins of the hadron analysis \ldots \ldots .	97 97
7.2	Hadron distribution as function of variables ${}^{lab}p_T$ and ${}^{lab}\eta$	
7.3	Measured data and MC comparison for hadrons (ALL triggers)	98
$7.4 \\ 7.5$	Measured data and MC comparison for hadrons (inclMT)	99 101
7.5 7.6	Charged hadron differential multiplicities comparison with EMC Charged hadron differential multiplicity ratio (COMPASS/EMC)	101
7.0 7.7	Charged hadron differential multiplicity ratio (COMPASS/EMC) Charged hadron differential multiplicity ratio	102 102
7.1 7.8		102
7.8 7.9	Mean p_T^2 vs <i>s</i> from Schweitzer et al	$104 \\ 104$
7.9 7.10	p_T distribution for $0.5 < z < 0.0$	$104 \\ 105$
	Mean p_T vs s with corrected COMPASS point	105
	Differential multiplicities and Gaussian fit $\dots \dots \dots$	100
	Differential multiplicities and Gaussian fit	108
	Differential multiplicities and Gaussian fit	109
1.1.7		TTO

7.15	Differential multiplicities and Gaussian fit	111
7.16	Differential multiplicities and Gaussian fit	112
7.17	Differential multiplicities and Gaussian fit	113
	$\langle P_T^2 \rangle$ vs Q^2	114
7.19	$\langle P_T^2 \rangle$ vs Q^2	115
7.20	$\langle P_T^2 \rangle$ vs x_{Bj}	116
7.21	$\langle P_T^2 \rangle$ vs x_{Bj}	117
7.22	$\langle P_T^2 \rangle$ vs Q^2 at fixed W^2	118
7.23	$\langle P_T^2 \rangle$ vs Q^2 at fixed W^2	119
	$\langle P_T^2 \rangle$ vs W^2	120
	$\langle p_T^2 \rangle$ as function of z^2	122
7.26	$\langle p_T^2 \rangle$ as function of z^2	123
	$\langle p_T^2 \rangle$ as function of z^2	124
	$\langle p_T^2 \rangle$ as function of z^2	125
	$\langle p_T^2 \rangle$ as function of z^2	126
	$\langle p_T^2 \rangle$ as function of z^2	127
	$\langle k_{\perp}^2 \rangle$ vs x_{Bj} , W^2 and Q^2	129
7.32	$\langle k_{\perp}^2 \rangle$ vs x_{Bj} charge comparison	130
A.1	F_2 comparison period W22 (inclMT)	133
A.2	F_2 comparison period W23 (inclMT)	134
	F_2 comparison period W26 (inclMT)	134
A.4	F_2 comparison period W27 (inclMT)	135
A.5	F_2 comparison period W30 (inclMT)	136
	F_2 comparison period W31 (inclMT)	136
A.7	F_2 comparison period W32 (inclMT)	137
A.8	F_2 comparison period W37 (inclMT)	137
	F_2 comparison period W38 (inclMT)	138
	F_2 comparison period W39 (inclMT)	138
	F_2 comparison period W40 (inclMT)	139
	Fraction of events triggered without requiring calorimeter signals.	143

List of Tables

4.1	Inclusive variable definitions	34
$ \begin{array}{l} 6.1 \\ 6.2 \\ 6.3 \end{array} $	Integrated luminosity period by period	77 79 79
7.1	Hadron selection statistics	96
B.1	SMC inclusive cross section and the parameters used for its determination	142
C.1 C.2 C.3 C.4	Fit results for $0.0045 < x_{Bj} < 0.006$ and $1 < Q^2 < 1.25$	145 146 146 147
C.5 C.6 C.7 C.8	Fit results for $0.008 < x_{Bj} < 0.012$ and $1.5 < Q^2 < 2.1$	147 148 148 149
C.9 C.10 C.11	Fit results for $0.018 < x_{Bj} < 0.025$ and $1 < Q^2 < 1.5$	149 150 150
C.13	Fit results for $0.018 < x_{Bj} < 0.025$ and $3.5 < Q^2 < 5$	151 151 152
C.15 C.16	Fit results for $0.025 < x_{Bj} < 0.04$ and $1.5 < Q^2 < 2.5$	$\begin{array}{c} 152 \\ 153 \end{array}$
C.18 C.19	Fit results for $0.025 < x_{Bj} < 0.04$ and $3.5 < Q^2 < 6$	153 154 154
C.21	Fit results for $0.04 < x_{Bj} < 0.07$ and $3.5 < Q^2 < 6$ Fit results for $0.04 < x_{Bj} < 0.07$ and $6 < Q^2 < 10$ Fit results for $0.07 < x_{Bj} < 0.12$ and $3.5 < Q^2 < 6$	155 155 156
	Fit results for $0.07 < x_{Bj} < 0.12$ and $6 < Q^2 < 10$	156

Summary

The COMPASS Collaboration has two main fields of interest: to improve our knowledge of the nucleon spin structure and to study hadrons through spectroscopy. These goals require a multipurpose universal spectrometer such as the COmmon Muon and Proton Apparatus for Structure and Spectroscopy, COMPASS. In its first years of data taking (2002-2007), the nucleon spin structure was studied with a polarized muon beam scattering off a polarized target. These studies resumed in 2010 and will continue until at least 2011. The years 2008 and 2009 were dedicated to hadron spectroscopy using hadron beams. In the case of the nucleon structure studies, it is crucial to detect with high precision the incoming beam muon (160 GeV), the scattered muon and the produced hadrons. The large amount of high quality data accumulated provides access to the unpolarized and polarized parton distributions of the nucleon and the hadronization process. Subtle differences (asymmetries) between polarized cross sections have been predicted for hadron production from polarized muon-nucleon interaction for COMPASS. It is based on these differences that the polarized parton distributions can be measured.

In this context, it is important to first compare predictions with the gross features of the measured unpolarized semi-inclusive differential cross sections or the closely related differential multiplicities. In order to determine cross sections, the data has to be corrected for the acceptance of the spectrometer. In this thesis, a multidimensional acceptance correction method, based on Monte Carlo simulation, is developed and applied to the data measured in 2004. The method is first used to determine the inclusive muon-nucleon cross section which is compared with a global fit to world data. This serves as a test of the acceptance correction method and to verify if the results from previous experiments can be reproduced. Then, unpolarized differential multiplicities as a function of transverse momentum are presented for different kinematical intervals. These multiplicities can be used as benchmarks to verify the reliability of theoretical models.

The subject of parton intrinsic transverse momentum is of growing interest to the spin structure community. The picture of partons moving collinear with the proton momentum is not sufficient to explain many spin features of the nucleons. Since a few years, transverse momentum dependent (TMD) distributions are integrated into theoretical models of nucleon interactions. Assumptions are made and it is to the experiment to test them. The Gaussian ansatz which assumes Gaussian behavior of the TMD distribution functions is applied and investigated. This model is very popular for its simplicity and ability to reproduce many experimental results. This analysis contributes to the verification of this model and suggests possible ameliorations. Based on this model, the intrinsic transverse momentum of the partons within the nucleon is extracted from the average transverse momenta of the measured hadrons. The extraction is carried out for different kinematical intervals to verify basic assumptions of the nucleon structure and fragmentation of partons into hadrons. Some insights are acquired about the flavor and kinematical dependence of the partons intrinsic transverse momenta. Finally, further studies and related analyses are proposed.

Zusammenfassung

Die COMPASS Kollaboration hat zwei wissenschaftliche Hauptziele: unser Wissen über die Spinstruktur des Nukleons zu erweitern und Hadronen mittels Spektroskopie zu untersuchen. Um diese Ziele zu erreichen, benötigt man ein universell einsetzbares Spektrometer. In den ersten Jahren der Datennahme (2002-2007) und den kommenden Jahre 2010 und 2011 wurde und wird die Spinstruktur des Nukleons mittels eines polarisierten Myon-Strahls und eines polarisierten Targets untersucht. Die Jahre 2008 und 2009 waren der Hadronspektroskopie gewidmet. Die große Zahl an gesammelten Myon-Daten von höchster Qualität ermöglicht einen Einblick in polarisierte und unpolarisierte Partonverteilungen des Nukleons und den Prozeß der Hadronisierung. Geringfügige Differenzen (Asymmetrien) zwischen polarisierten Wirkungsquerschnitten waren für die Hadronproduktion bei polarisierten Myon-Nukleon Wechselwirkungen vorhergesagt worden. Nur auf der Basis dieser Differenzen kann man die polarisierten Partonverteilungen messen.

In diesem Zusammenhang ist es wichtig, zuerst die Vorhersagen mit den allgemeinen Eigenschaften der gemessenen unpolarisierten semi-inklusiven differentiellen Wirkungsquerschnitte oder den eng damit zusammenhängenden Multiplizitäten zu vergleichen. Um Wirkungsquerschnitte zu bestimmen, müssen die Daten auf die Akzeptanz des Spektrometers korrigiert werden. In der vorliegenden Doktorarbeit wird eine multidimensionale Methode, basierend auf Monte-Carlo Simulationen, zur Akzeptanzkorrektur entwickelt und auf die Daten der Messung aus dem Jahr 2004 angewendet. Die Methode wird zuerst angewendet, um den inklusiven Myon-Nukleon-Wirkungsquerschnitt zu bestimmen und diesen dann mit einem allgemeinen Fit der weltweit dazu verfügbaren Daten zu vergleichen. Dies dient als Test der Methode der Akzeptanzkorrektur und um zu verifizieren, ob die Resultate vorhergehender Messungen reproduziert werden können. Im nächsten Schritt werden die unpolarisierten differenziellen Multiplizitäten als Funktion des transversalen Impulses für verschiedene kinematische Intervalle dargestellt. Diese Multiplizitäten können als Bezugspunkt dienen, um die Zuverlässigkeit theoretischer Modelle zu überprüfen.

Das Bild, dass Partonen sich kollinear zum Impuls der Protonen bewegen, reicht nicht aus, um viele Aspekte der internen Spinstruktur von Nukleonen zu erklären. Seit einigen Jahren werden transversalimpuls-abhängige Verteilungsfunktionen (TMDs) in die theoretischen Modelle der Nukleonen-Wechselwirkungen integriert. Der Gauß'sche Ansatz, der von einer Gaußform der TMDs ausgeht, wird angewandt. Dieses einfache Modell kann viele experimentelle Resultate reproduzieren. Basierend darauf kann der intrinsische Transversalimpuls der Partonen aus den mittleren Transversalimpulsen der gemessenen Hadronen extrahiert werden. Die Bestimmung erfolgt in verschiedenen kinematischen Intervallen, um grundlegende Annahmen zur Struktur des Nukleons zu bestätigen. Hiermit erhält man einige Einblicke in die Abhängigkeit der intrinsischen Transversalimpulse der Partonen von Flavour und Kinematik. Die vorliegende Analyse leistet einen Beitrag zur Verifizierung dieses Modells. Zum Schluss werden weitere Studienverbesserungen und Analysen vorgeschlagen.

Chapter 1 Introduction

Matter has been studied through particle scattering for more than a century. In its most simplified version, a structureless beam particle scatters off a target particle. The scattered particle angular distribution of many such scattering events depends on the structure of the target particle. Since the first scattering experiments, this picture has evolved tremendously. The interaction is now known to be mediated by an exchange particle and the final states usually "evolve" before detection. Models of the structure of matter are still interplays of theory and experiment. Experiments have evolved and became more complex, but the technique remains: a beam scatters off a target. In this thesis, it will be shown how muon-nucleon scattering at COMPASS contributes to this knowledge.

The first scattering experiment studying the nuclear structure can be traced back to the famous Geiger and Marsden scattering of α -particles on gold atom in Rutherford's laboratory. Their radiation source (decay of radium) not only provided α -particles but also electrons. These radiated electrons did not have enough energy to penetrate the electron cloud of the atom so they were considered as background. Their results could be described by elastic scattering off a point charge.

In 1932, James Chadwick performed a series of experiments that lead to the discovery of the neutron. The atom mass, charge and spin could finally be understood as composed of protons and neutrons, the *nucleons*. In 1951, Rosenbluth calculated the electron-proton scattering cross section for an extended proton with two form factors, G_E and G_M , related to the electric and magnetic charge distribution, respectively. In the 1950s, first electronnucleus/proton interactions were observed. The Mark III linear accelerator at Stanford with 225 MeV electrons scattered off a hydrogen gas target lead to the first estimation of the size of the proton. Then, scattering off deuterium target provided information about the neutron. By the end of the 1950s and the beginning of the 1960s, many electron scattering facilities around the world with energy up to 6 GeV (DESY) contributed to the study of the nucleons. In 1967 in Stanford, a major step forward was accomplished at SLAC with an electron beam energy of 20 GeV. This unprecedented energy enabled first probing of the internal structure of baryons, known as deep inelastic scattering (DIS). A very unexpected behavior of the DIS cross section, compatible with elastic scattering from point-like constituent, was observed. These results gave credibility to the constituent quark parton model (QPM) of the nucleon.

At first, only the scattered electron was observed in DIS experiments which is defined as inclusive analysis. In the case of elastic scattering, there is not much more to observe since the recoil of the target particle can be deduced from momentum conservation. In the case of DIS, only a part of the target particle interacts (the quark in the framework of the QPM) and the target particle can be modified. Hence, conservation of momentum is not enough to understand a whole DIS interaction. Since confinement precludes isolated quarks, a struck quark leaving the nucleon hadronizes (producing hadrons) before it can be observed. When the interaction is known¹, there are then two remaining unknowns to the final state observed by a DIS experiment. First, the interaction depends on the distribution of the partons (quarks in the QPM) inside the nucleon, the so-called parton distribution function (PDF). Second, the final states depend on the function describing the probability of a certain parton to *fragment* into different hadrons, the so-called fragmentation function (FF). The two function types, PDF and FF, are to be determined by experiments.

More information is gained in DIS when looking at more final particles than just the scattered particle (usually a lepton). The observation of DIS events and produced particles is referred to as semi-inclusive deep inelastic scattering (SIDIS). Already in the 1970s, experiments observed final state particles. At the same time, new experiments joined the effort with higher energy and different beam particles (e.g. muons and neutrinos). The theory also went along; Quantum chromodynamic (QCD) was developed and introduced the gluons and confinements explaining why isolated quarks were never observed. The idea of partons with intrinsic transverse momentum was already introduced in the early 1970s, but as stated by Cahn in 1978, have "...not only been overlooked recently, but were stated obscurely" (see [17] and reference therein). It this article, Cahn demonstrated how intrinsic transverse momenta of partons affect the azimuthal distributions of the muoproduced hadrons. His motivation was to correct a proposed test for quantum chromodynamics. Cahn concludes that "As a results, rather accurate, high statistics experiments with incident muons or neutrinos will be required to observe these effects.". More than 30 years later, COMPASS has the ability to verify this prediction as released in [48].

As an improvement of the first DIS experiments, polarized beams on polarized targets provided access to new structure functions, the polarized PDFs. In the 1980s, polarized DIS allowed to determine the quarks contribution to the spin of the nucleon. It came as a surprise, as will be explained later, that it is relatively small. The next logical candidates

¹ It is often assumed to be mediated by one photon. This is not true at high energy where the weak interaction also contributes. For SLAC and COMPASS, the latter can be safely neglected. One contribution that cannot be neglected is higher order quantum electrodynamics (QED) contribution, the so-called radiative effect, where more than one photon is involved. This will be discussed in the following sections.

were the gluons. COMPASS and other experiments now suggest that a significant contribution from the gluons is very unlikely. The remaining candidate to contribute to the spin of the nucleon is the orbital angular momentum of the constituents. This is much more complicated to measure. Nevertheless, an orbital angular momentum of the partons is related to their intrinsic transverse momenta. It is now an accepted feature of the nucleon to have partons with intrinsic transverse momentum. But many questions remain open: How is this angular momentum distributed among all the constituents of the nucleon? Is it flavor dependent? Is it different for valence and sea quarks? For now, only simple models can be treated analytically. The goal of this analysis is to test one such model using the unpolarized hadron production cross sections. These cross sections are also proposed as benchmark reference for numerical calculations.

This thesis consists of three main parts. First, an overview of the COMPASS experiment with its main physics goals and a description of the spectrometer is given. The second part describes the theoretical background needed for the analysis, starting from simple DIS to the semi-inclusive DIS with intrinsic momentum and fragmentation. Finally, differential hadron production cross section and multiplicity determination is explained and results are presented for different kinematic intervals. The multiplicities are fitted and compared with a simple model that includes assumptions about the intrinsic transverse momentum of the parton. These assumptions are investigated and limitations of the model and of the analysis are then discussed. _____

Chapter 2

The COMPASS experiment

2.1 Physics goals of COMPASS

COMPASS stands for COmmon Muon and Proton Apparatus for Structure and Spectroscopy. It originates from the association of two projects. The first one, HMC [36], was a proposal for polarized DIS to investigate the structure of the nucleons, in particular the contribution of the gluons to the spin of the nucleon. The second one, CHEOPS [38], was a proposal for the study of hadronic structure, semi-leptonic decay of charmed baryons and search for exotic baryon states. The goals of those two projects could be reached by one fixed target spectrometer in the North Area of the CERN SPS. There, many secondary $(\pi^{+,-}, K^{+,-}, p, \bar{p})$ and tertiary (polarized $\mu^{+,-}$) beams are available. The joint project COMPASS was proposed [25] to reach the goals of both HMC and CHEOPS.

An overview of the main physics goals at COMPASS is presented in the following sections. First, the muon beam program which has been going on from 2002 to 2007, then the hadron beam program for 2008 and 2009. In 2010, the beam is back to muon. The COMPASS spectrometer has still much to offer and the last section is a short survey of possible future physics.

2.1.1 Physics with the muon beam

Physics with muon beam at COMPASS follows a long tradition of DIS experiments where the muon is used to probe the structure of the nucleon. As explained below, the muons delivered to the COMPASS experiment have their spin longitudinally polarized along the muon direction. In order to study the polarized structure, the target has to be polarized. Depending on the analysis, the target can be either longitudinally or transversely polarized with respect to the muon polarization. COMPASS has accumulated data from both polarization configurations. This section describes physics analysis with these two configurations.

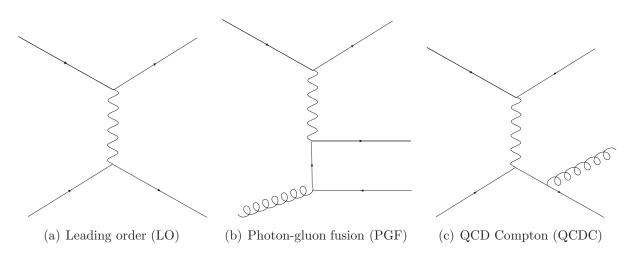


Figure 2.1: Basic photon quark and gluon interactions

Longitudinal target polarization

In the longitudinal configuration, the spin of the target is oriented either in the same direction as the beam polarization or opposite. This spin configuration gives access to the polarized structure function g_1 which, in the quark-parton model, is the polarized quark distribution. It also allows to evaluate the contribution of the gluons to the spin of the nucleon. In the latter study, it is necessary to select processes that involve gluons. Since the gluons do not carry electromagnetic charge, the photon-gluon interaction is not direct (i.e. not at the order 0 of QCD). The lowest order of photon-gluon interaction is called the photon-gluon-fusion (PGF). In a PGF process, a quark is exchanged between the photon and the gluon and a quark anti-quark pair is produced as shown in figure 2.1(b). This process is not dominant as its cross section is reduced by a factor α_s compared with the leading order (LO), photon-quark interaction shown in figure 2.1(a). Moreover, at the same order as PGF, there is another competing mechanism, the QCD Compton (QCDC) scattering shown in figure 2.1(c). In order to select the PGF process, COMPASS has two main methods:

Open charm

When a hadron comprising a charm quark is found in the final state, it is unlikely that the charm quark came from the nucleon. The mass of the charm quark being so large, chances are that it was indeed "created" by the interaction rather than struck by the virtual photon. Similarly, the charm quark large mass reduces its chances to be created by fragmentation. Assuming that the charm quark did not come from the nucleon nor by fragmentation, the detection of a charmed hadron is a very clean signal of PGF. The produced charmed hadron is a D^0 meson in about 60% of the cases. This meson then decays in a detectable pion-kaon pair ($D^0 \to K\pi$) with a branching ratio of about 4%. This reduces the statistic sample significantly, but it is very clean based on the simple assumption mentioned above.

The event sample can be even further purified by selecting the D^0 that were produced by the decay of an excited state $(D^* \to D^0 \pi_s)$, they represent about 30% of the produced D^0 . The D^* can be *tagged* by the soft pion, π_s , with momentum limited by the mass difference $\Delta M = \Delta M_{D^*} - \Delta M_{D^0} = 145$ MeV which is slightly above the pion mass.

High- p_T pair

PGF events are also more likely to create two hadrons with high transverse momenta with respect to the photon direction (p_T) . The leading order interactions favors forward hadrons. Contrary to the open charm method, the light flavored produced hadrons are also included in the analysis which increases the size of the statistics sample significantly. The price to pay for this statistical improvement is the reduction of the purity of the sample. Indeed, the high- p_T pair selection cannot distinguish between PGF and the background QCDC events shown in figure 2.1. The fraction of PGF from the sample is then determined by a theoretical model. In the case of COMPASS, the fraction of PGF of the high- p_T sample is estimated to be about 30% for both high ([7]) and low ([37]) virtuality¹ analysis. Most of the studies mentioned above are measured through cross section asymmetries. More and more analysis at COMPASS are considering absolute cross sections as in the present analysis.

Transverse target configuration

In the transverse configuration, the spin of the target is perpendicular to the spin of the beam. This gives access to the polarized structure function g_2 of the nucleon which vanishes in the simple quark-parton model. This configuration also gives access to the transverse PDFs, $\Delta_T q$, which have been studied by COMPASS through two different effects (cf. [11] and [13]):

- The Collins effect [31] which is the convolution of $\Delta_T q$ with a "chiraly-odd" fragmentation function, $\Delta_T^0 D_q^h$.
- The Sivers effect [61] which is based on a possible existence of a correlation between the intrinsic transverse momentum (k_{\perp}) of the parton and the transverse polarization vector of the nucleon. Transverse configuration gives access to the convolution between the Sivers PDF, $q_T(x_{Bj}, \vec{k_{\perp}})$, and the unpolarized fragmentation function.

Of course, the DIS data accumulated from 2002 to 2007 has produced and will produce more physics results than the short summary above. Most of them can be categorized in the structure of the nucleon, for example, the determination of the structure function g_1 [14], or polarized quark distributions [10] and [12].

¹ Virtuality refers to the exchanged photon. It will be explained below that the the exchanged photon has a mass $-Q^2$. The higher the photon mass, the higher its virtuality will be. In the case of COMPASS, high virtuality is defined as $Q^2 > 1$ (GeV/c)².

2.1.2 Physics with the hadron beam

The hadron physics program with hadron beam started with a two-week pilot run in 2004 and used the full beam time of 2008 and 2009. For 2008, the first hadron beam dedicated year, some changes were made to the spectrometer and new detectors were also implemented. Namely, a new target with recoil proton detector, a sandwich veto detector² and major improvement on the calorimetry system. The major physics interests are:

Pion polarizability

Compton scattering off extended charged particles reveals their response to the exposure of a strong electromagnetic field. The response function can be quantified by electric and magnetic polarizabilities which have a classical interpretation. The polarizabilities become visible by a deviation of the measured cross section from the one expected for point-like particle. The preliminary results of the pilot run agreed with low energy QCD calculations. These have been put into question by recent measurements made at Mainz University. Therefore, a more precise measurement will help clear the situation. For more details see [44].

Exotic states

QCD allows different hadronic states that include gluons and even pure gluonic states, glueballs. The quantum numbers of the (hadron) beam particle can be altered by the exchange with the target, through Regge or Pomeron exchange, leading to the creation of exotic states. This can happen in diffractive production, where the beam particle becomes the exotic or by central production, where the projectile and the target stay intact, but the exchange particles create the exotic. First results have already been published in [9].

2.1.3 Future physics

Further muon scattering in longitudinally polarized target

COMPASS intends further measurements of longitudinal target spin configuration. Results from COMPASS and other experiments strongly suggest that the gluons (with the quarks) are not the only contributors to the spin of the nucleon. It is important to improve the knowledge of the spin structure function, especially the function g_1 , which will help to better constraint the parton (including the gluon) PDFs.

Further muon scattering in transversely polarized proton target

The HERMES experiment at DESY has measured sizable transverse (Collins and Sivers) asymmetries on the proton [34]. A verification of this result is of utmost importance. COMPASS made its measurement on the deuteron and found asymmetries compatible

 $^{^2 \}rm Which$ was built by the LMU group.

with zero which is believed to be the result of cancellation of the proton and neutron asymmetries in the deuteron. During half of the 2007 data taking period, COMPASS performed an exploratory measurement with a proton target (cf. [43] and [13]). HERMES results were confirmed for the Collins asymmetries, but there is not a clear agreement for the Sivers case. However, given the present statistical error, the disagreement is marginal. Moreover, COMPASS measurement gives an indication for a possible dependence on the invariant mass³. Precise measurements of the transverse spin asymmetries for the proton are eagerly awaited by the spin physics community.

Parton distribution functions

Now that the gluons have been investigated, there is a growing interest into the angular momentum of the partons which could also contribute to the spin of the nucleon. Transverse spin effects are linked to the angular momentum in the nucleon. COMPASS intends to further their studies with lepton-nucleon scattering, but it will always be convoluted with fragmentation functions as was noted for the Collins and Sivers effect. A way to get rid of the fragmentation effect is to look at reactions where the final states are made of leptons because they do not hadronize. This happens in the Drell-Yan process where, in a hadron-hadron collision, a quark-antiquark annihilate creating a virtual photon (or Z boson), which then decays into a pair of leptons. However, the Drell-Yan cross section contains two PDFs, one for the quark and one for the antiquark, hence the need for a good PDF description. COMPASS intends to study the transverse momentum dependent distributions and transverse distributions by detecting the Drell-Yan process in the scattering of a pion beam off a transversely polarized target.

COMPASS will also contribute to the new theoretical concept of generalized parton distribution (GPDs) functions. The GPDs link form factors and PDFs and in addition describe parton correlations. GPDs attracted much attention after it was shown that the total angular momentum of a given parton species is related to the second moment of the sum of two GPDs. Constraining quark GPDs experimentally by measuring deeply virtual Compton scattering (DVCS) or meson production (DVMP) is the only known way to constrain the quark angular momentum contributions to the nucleon spin budget. COMPASS intends to study GPDs by measuring DVCS and DVMP on both unpolarized liquid hydrogen and polarized target.

 $^{^{3}}$ The invariant mass will be defined later.

Chapter 3

Experimental setup

3.1 Spectrometer overview

The COMPASS spectrometer has been designed to be versatile enough to pursue a wide range of physics studies. The versatility is not only expressed by its manifold particle identification, track resolution or high rate data taking, but also by its ability to be *modified* even during a period of data taking. For example, the setup was quickly modified at the end of the 2004 beam time for the two weeks hadron pilot run. Since then, each years had a few days dedicated for preliminary studies such as DVCS, Drell-Yan and others. The COMPASS setup has also been improved over the years, detectors have been added or replaced, a new electromagnetic calorimeter (ECAL1) has been included in the year of 2006. With such a constantly evolving spectrometer, a description of the COMPASS setup has to specify for what year it is intended. The data used for this analysis was collected during the longitudinally polarized target program of 2004. Therefore, the description of the experimental setup will focus on the spectrometer status of that year.

3.1.1 Beam

M2 beam line

The COMPASS experiment receives its beam from the M2 Beam line (see e.g. [35], [41]), which also provided beam for previous muon DIS experiments such as EMC, NMC, SMC. It provides a high intensity tertiary muon beam with a mean momentum of 160 GeV/c. Every 16.8 s, $2 * 10^8$ muons are delivered in a time interval of 4.8 seconds. To provide those muons, the CERN super proton synchrotron (SPS) delivers every 16.8 seconds cycle about 10^{13} primary protons with 400 GeV/c energy which are steered towards the North Experimental Area. A fraction of this beam is directed towards the primary target T6 (close to half a meter of Beryllium). This generates a secondary positively selected beam of (mainly) pions (~ 95%) and kaons (~ 5%) traveling a decay channel 600 meters in length where about 10% of the π^+ decay into $\mu^+ \bar{\nu}_{\mu}$. At the end of the decay channel, quadrupole magnets serve to focus the muons of 160 GeV/c on an absorber consisting of rods of about

few meters of Beryllium. In these rods, the hadrons are stopped and the muons loose only few GeV. Beryllium is used for its small ratio of nuclear interaction length over radiation length which provides minimum multiple Coulomb scattering for a given hadron stopping power. After the absorber, a system of focusing magnets is used to select (and focus) the muons of 160 GeV/c. The muons are naturally polarized due to the parity violation in the $\pi \to \mu \nu_{\mu}$ or $K \to \mu \nu_{\mu}$ decays. Indeed, the pions (kaon) have spin 0 which has to be conserved by the combined decay products. The neutrino being left handed, the muon has no choice but being also left handed. This is correct in the pion center of mass system (c.m.s.), but a change of the reference system in the opposite direction of the muon momentum can change the direction of the muon (but not its spin direction). Hence, in the laboratory system, the beam is not purely, but about 80%, polarized.

Beam Momentum Station

The beam momentum station (BMS) consists of four scintillator hodoscopes located symmetrically upstream and downstream of a bending magnet. The system has been designed to measure the momentum of more than 10^8 individual particles per burst with a relative precision of 1%. In order to eliminate ambiguities in the reconstruction of particle trajectories, their time of transit is measured with a resolution of 50 ps.

3.1.2 Target

The COMPASS muon program aims to measure cross section asymmetries $\Delta \sigma/2\bar{\sigma}$, where $\Delta \sigma$ is the difference between the cross sections of a given process for two different spin configurations and $\bar{\sigma}$ is the spin averaged cross section. What COMPASS actually measures is the counting rate asymmetry $A_{obs} = (P_{\mu}P_T f)(\Delta \sigma/2\bar{\sigma})$, where P_{μ} and P_T are, respectively, the beam and target polarization and f, the fraction of polarizable material in the target. The closer the factor P_{μ} , P_T and f are to one, the more statistically significant will be the measured asymmetry. The deuteron target must have a high degree of polarization. The chosen material was deuterated lithium (⁶LiD) which can be considered to a good approximation as a spin-0 ⁴He nucleus (i.e. an α particle) and two deuteron. This material can reach polarization over $P_T > 40\%$ and a polarized fraction $f \approx 0.35$. The asymmetry is measured using a target divided into two cells of opposite spin configurations. This setup was designed in order to have the same flux going into the two cells. In order to avoid acceptance differences of the two cells, the spin configuration was inverted every eight hours.

The two cylindrical target cells are 60 cm long and 3 cm in diameters. They are separated by a 10 cm gap in order to determine in which cell the interaction took place without ambiguity. For particles produced at the most upstream part of the upstream cell, the angular acceptance is 70 mrad, wider angles are blocked by the solenoid magnet used for polarization.

3.1.3 Magnets

The COMPASS spectrometer is divided in two parts, the large angle spectrometer (LAS) and the small angle spectrometer (SAS), each having its own dipole magnet SM1 and SM2, respectively. Together, these two "subspectrometers" fulfill the large momentum range and large angular acceptance requirements of the physics goals. The vertical fields of the SM1 and SM2 magnets deviate the charged particles with the Lorentz force $\vec{F} = q(\vec{v} \times \vec{B})$, which allows to determine their charge-momentum ratio. When the deviation is small, and the trajectory is perpendicular to the field \vec{B} , the charge q, momentum p and deflection angle θ are related as follow:

$$\frac{q}{p} = \frac{\theta}{0.3 \int Bdl}.$$
(3.1)

The bending power $\int Bdl$ for SM1 is 1.0 Tm and can deflect wide angle particles with small momenta as low as 0.5 GeV/c. SM2 has a bending power of 4 Tm which combined with the 10 meters of the downstream tracking detectors allows the detection of particle from 5 GeV/c to very high momenta.

3.1.4 Tracking detectors

The particle flux per unit transverse surface varies by more than five orders of magnitude in the different regions of the spectrometer. Close to the beam axis and close to the target, the rates can be very high (up to few MHz/cm²). On the other extreme, the required large acceptance calls for track detection up to more than a meter away from the beam axis. It is also important that the material budget, especially along the beam trajectory, should be kept minimal in order to avoid multiple scattering and secondary interactions. The tracking detectors are grouped in three categories:

- 1. -Very Small Area Trackers **VSAT** Trackers closest to the beam where the flux is of the order MHz/cm². Their lateral sizes vary from 4 cm to 12 cm, to take into account the beam divergence along the beam axis. They consist of
 - Scintillating fibre detectors (SciFi): Used to provide tracking for the incoming and scattered beam. Eight SciFi stations are installed from upstream of the target to the end of the spectrometer. Their transverse size vary from 4 cm^2 , closest to the target, to 12 cm² at the end of the spectrometer. Each station consists of at least two projections, one vertically and one horizontally sensitive. Some stations also comprise an additional inclined (~ 45°) projection. Their intrinsic efficiencies are about 99%, but in high intensity region it reduces to 96% due to occupancy in the readout. Their space resolutions vary from 130 μ m to 210 μ m. The time resolution at the central region, where the occupancy is highest, vary from 350 ps to 450 ps and gets slightly better in the outer region of lower occupancies.

- Silicon microstrip detectors: Used for the detection of the incoming muon beam. They consist of $300 \,\mu\text{m}$ thick silicon wafer with a $5 \times 7 \,\text{cm}^2$ active area. Each wafer has vertical and horizontal strip so that with one wafer, two dimensional position information can be obtained. The space resolutions varies from $8 \,\mu\text{m}$ to $11 \,\mu\text{m}$ and the average time resolution is 2.5 ns.
- 2. -Small Area Trackers **SAT** Trackers for distances from the beam larger than 2.5 cm and up to 20 cm where the flux is of the order of kHz/cm². It is the domain of micropattern gas detectors. They are medium size detectors with high space resolution and minimum material budget. They consist of
 - Micromesh Gaseous Structure (Micromegas): Detectors based on a parallel plate electrode structure and a set of parallel microstrips for readout. A metallic micromesh which separates a gaseous volume into two regions. First, a conversion gap where the ionization takes place and the resulting primary electrons drift in a moderate electric field. Second, an amplification gap where a higher field produces an avalanche which results in a large number of electron/ion pairs. The detectors have an active area of 40 × 40 cm² and a central dead zone of 5 cm in diameter. Micromegas are assembled in doublets of two identical detectors rotated 90° with respect to one another. There are 12 planes of Micromegas, grouped in three stations between the target and the first dipole magnet SM1. The efficiency reaches 97% at nominal beam intensity. Average space and time resolution are 90 μm and 9.3 ns, respectively.
 - Gas Electron Multiplier (GEM): The concept of these detectors is similar to the Micromegas, but with three amplification gaps. The active area is $31 \times 31 \text{ cm}^2$. The central region of 5 cm diameter is deactivated to avoid too high occupancies on the central strips. In 2004, there were 11 GEM detector stations, i.e. 22 detectors distributed along the spectrometer. The average efficiency was determined to be 97%. Average space and time resolution are 70 μ m and 12 ns, respectively.
- 3. -Large Area Trackers LAT- The reduced flux in the outermost regions allows the use of drift detectors. They consist of
 - Straw tube drift chambers: These drift detectors, under the responsibility of the LMU group, are described in a later chapter.
 - Drift chambers (DC): Each drift chamber consists of eight layers of wires with four different different inclinations: vertical, horizontal, and 20° (counter) clockwise tilted. They have an active area of $180 \times 127 \,\mathrm{cm}^2$ with a 30 cm diameter dead zone around the beam. The mean layer efficiency is 95% or higher for the more downstream layers where there are lower hit rates. The average space resolution for a wire layer is 270 μ m.

- Multiwire proportional chambers (MWPC): Used for the tracking of particles at large radial distances. Different types of MWPC cover areas of $178 \times 120 \text{ cm}^2$ or $178 \times 80 \text{ cm}^2$ with a central 16-22 mm diameter dead zone. The 34 wire layers have either vertical, horizontal or tilted orientation. They have an average efficiency of 98% and a spatial resolution of about 1.6 mm.
- Large area drift chambers: Large angle charged particles of the SAS can also be detected by the six large area drift chambers. They have an active area of $5 \times 2.5 \text{ m}^2$ and a dead zone diameter of 1 m (except one with 0.5 m). The layers are oriented either vertical, horizontal or tilted. The average efficiency is 93% and the average space resolution is 0.5 mm.

3.1.5 Calorimeters

In 2004, COMPASS was equipped with two hadronic calorimeters, HCAL1¹ in the LAS, and HCAL2 in the SAS. They are both made of stacks of iron and scintillator plates. When a hadron passes trough a hadronic calorimeter, it deposits its energy in a form of hadronic shower. In the case of muons, only a small fraction is deposited. Hence, the hadronic calorimeters are used to distinguish hadron from muon tracks. The signal measured is used to determine the energy by a proportionality relation. Hadronic calorimeters are also used by the trigger system as described in a later section.

There was also an electromagnetic calorimeter, ECAL2, situated in the SAS. A photon or electron passing through an electromagnetic calorimeter produces an electromagnetic shower which produces Cherenkov light. The light intensity is proportional to the deposited energy. ECAL2 is not used by the trigger system.

HCAL1

The LAS hadronic calorimeter, HCAL1, is situated after SM1 and before SM2. It consists of 480 calorimeter modules 28(horizontal)×20(vertical) with some modules removed in the corners and in the center $(1.2\times0.6 \text{ m}^2 \text{ to free area for the beam})$. The dimensions are $4.2\times3 \text{ m}^2$ for an active surface of 10.8 m^2 . The light from the scintillators is collected by light guides placed on the open side of the scintillators and sent to photomultipliers. The calorimeter is shielded by a lead wall to protect from electrons. The energy resolution is $\sigma(E)/E \approx 60\%/\sqrt{E} \oplus 8\%$ with the energy E in units of GeV. The space resolution is about $\sigma_{x,y} = 14 \text{ mm}$. The efficiency depends on the energy, but for hadrons with momenta above 5 GeV/c, it is almost constant and close to 100%.

¹ The last character of the calorimeter name, either 1 or 2, refers to the LAS and SAS, respectively. That is why the electromagnetic calorimeter, situated in the SAS, is named ECAL2 even though there was only one in 2004. In 2006, a new electromagnetic calorimeter was included in the LAS and was therefore named ECAL1. The same apply to the RICH detector in the LAS, which is named RICH1 and an eventual RICH detector in the SAS would then be named RICH2.

HCAL2

The SAS hadronic calorimeter, HCAL2, is situated downstream of SM2. It consists of 22×10 modules. The modules of the central region (8×6 around the emptied area for the beam) have more layers and are thicker. Although designed differently, the light collection is similar to HCAL1, using light guides and photomultipliers. Energy resolution is $\sigma(E)/E \approx 66\%/\sqrt{E} \oplus 5\%$. The efficiency for hadrons with energies above 10 GeV is close to 100%.

ECAL2

The only electromagnetic calorimeter of the spectrometer in 2004, ECAL2, is situated just before HCAL2. It consists of 2972 (64×48) lead glass modules connected to photomultipliers with light guides. There is a hole of 10×10 modules in the center to free area for the beam and the 800 modules closest to the center are radiation hardened (by adding 2% of Cerium). About 1000 photoelectrons per GeV energy deposited are obtained. The energy and space resolution are $\sigma(E)/E = 5.5/\sqrt{E} \bigoplus 1.5\%$ and $\sigma_{x,y} = 6/\sqrt{E} \bigoplus 0.5$ mm, respectively.

3.1.6 Muon walls

Muons are identified by means of muon filters MW1 and MW2 in the LAS and SAS, respectively. They consist of a 60 cm thick iron wall, MW1, and a 2.4 m thick concrete wall, MW2. They are preceded and followed by tracking stations. They represent several radiation lengths for hadrons such that particles passing through the muon filters are identified as muons.

3.1.7 RICH

Precise particle identification is possible with the large size Ring Imaging Cherenkov detector (RICH). It covers the whole acceptance of the LAS for particles with energy between 5 GeV and 43 GeV. Its 3 m long vessel is filled with C_4F_{10} as radiator gas. The Cherenkov photons are reflected by a mirror system in order to detect them outside of the LAS acceptance. The photons are then detected by a MWPCs. The RICH detector is not used in this analysis.

3.1.8 Trigger system

The main purpose of the COMPASS trigger system is to select relevant events at high rate and send decision signals to the readout of detectors and front-end electronics. Because of the high rate environment, the decision has to be made within less than 500 ns with a limited dead time. It also provides a reference time for the events. The trigger system comprises three elements: Trigger hodoscopes used to measure coincidence of the muon trajectory points, Veto hodoscopes to exclude halo muons and calorimeters to select events

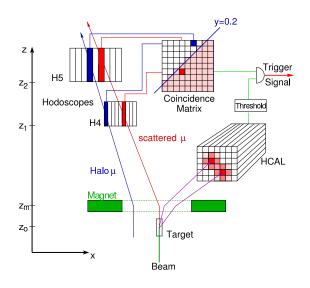


Figure 3.1: Concept of the trigger combining hodoscope and hadronic calorimeter.

that produced hadrons. The latter is especially important in the quasi-real photon regime (i.e. low Q^2), were the muon beam is deflected by an angle² so small that the event can be confused with elastic scattering off target electron, radiative scattering off target nucleus or beam halo seen as scattered muons. A conceptual representation of a hodoscope trigger combined with a calorimeter is shown in figure 3.1.

Hodoscope trigger

The hodoscopes of the trigger system can be either vertical or horizontal slabs, giving horizontal or vertical position of tracks, respectively. The hodoscope trigger is divided into four subsystems consisting of two hodoscope stations:

- Inner Vertical hodoscopes H4I and H5I cover the lowest Q^2 and are the closest to the beam axis.
- Ladder Vertical hodoscopes H4L and H5L, mostly $Q^2 < 1 \text{ (GeV/c)}^2$.
- Middle Horizontal and vertical hodoscopes H4M and H5M, cover $Q^2 \approx 1 \, (\text{GeV/c})^2$.
- Outer Horizontal hodoscopes H2O and H4O, cover the highest Q^2 up to ~ 20 $(\text{GeV/c})^2$.

Their relative positions are shown in figure 3.2.

² It will be later shown (cf. table 4.1) that the muon deflection angle Θ is related to Q^2 .

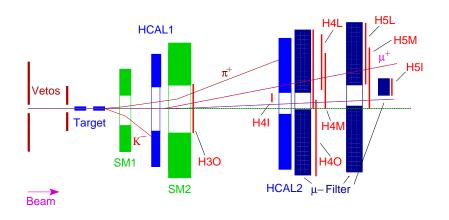


Figure 3.2: Position of the trigger components.

In the low Q^2 hodoscopes (Inner and Ladder), the muon deflection angle is so small that the trigger condition is based on the energy loss of the muon. The (horizontal) deflection of the muon in the magnetic field depends on its energy, hence the vertical hodoscope slabs give the bending information in the (horizontal) magnetic bending plane. The higher Q^2 trigger (Outer) on the other hand, detects muons with scattering angles large enough to be measured. Hence these triggers are made of horizontal hodoscope slabs measuring the vertical deflection which is not affected by the magnetic field. The middle trigger overlaps low and high Q^2 and uses both vertical and horizontal hodoscope slabs.

The hodoscope light signals are sent through light guides to photomultipliers. The resulting signals are then fed to a coincidence matrix, as shown in figure 3.1, which corresponds to muons that either lost a minimum of energy (vertical hodoscope) or to tracks that can be extrapolated back to the target (horizontal hodoscope).

Calorimeter trigger

As explained earlier, selection of the wanted events are improved by assessing that energy is deposited in the calorimeter. In order to avoid the $2 \cdot 10^7$ halo muons per second, an energy cluster is required to be above some threshold. The halo muons deposit energy of about 1.8 GeV, and the threshold for calorimeter in coincidence with hodoscope trigger is typically 5.4 GeV. The calorimeter can also be used as a standalone trigger (pure calorimetric trigger) where the threshold is increased to 8 GeV. The pure calorimetric trigger gives access to a large range of Q^2 up to values not covered by the hodoscopes.

Veto system

Even when the beam is focused on the target, there always is a halo of muons around it. To keep only events with a muon interacting in the target, hodoscopes are placed upstream and downstream of the target as represented in figure 3.3. When a track is "vetoed",

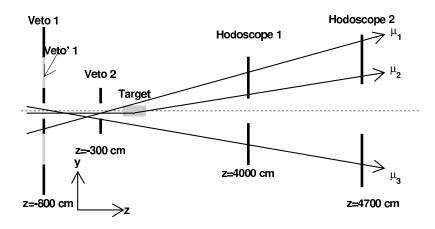


Figure 3.3: Schematic layout of the veto system

the trigger signal is prohibited. This creates a dead time of about 20% at nominal beam intensity. The veto signal affects only on the hodoscope triggers (middle and outer)³.

3.1.9 Data acquisition system

Data from the 250000 channels at a trigger rate of 10kHz during the 4.8 seconds spill time is managed by the COMPASS data acquisition system (DAQ) to be sent to permanent storage. The DAQ is represented schematically on figure 3.4.

Trigger Control System

At the beginning of each spill, the trigger control system (TCS) synchronizes the clocks of the TDC of every detector front-end. When an event fulfills the trigger conditions, TCS sends a signal and event label to the readout-driver modules named CATCH⁴. It also generates dead time in order to keep detectors to receive too high trigger rates. To satisfy different detector electronics and DAQ limitations, three types of dead time are applied:

- A minimum of $5 \,\mu s$ between two trigger signals.
- No more than three trigger signals within $75 \,\mu s$.
- No more than six trigger signals within $225 \,\mu s$.

This leads to a 5% dead time of the DAQ. Finally, it also sends signals for detector calibration. For example, TCS sends a signal to HCAL1 LED to flash light for on-line photo-multiplication calibration.

³A subsample of the veto was also used for the ladder trigger.

 $^{^4}$ In the case of GEM and Silicon, detectors with high rate, high occupancies and high channel density, different readout-driver modules named GeSiCA are used.

CATCH

The CATCH are the interface between TCS, the detectors and the event building computers. The readout of all detectors is unified to the CATCH⁴. Their functions are:

- Distribution of the trigger signals and timing signals to the front-ends.
- Initialization of the front-ends.
- Merge the data received from the digitizing units of the front-ends from the same event (sub-event concentration) and add event information from TCS.
- Send merged data to the counting room (ROB and EB).

Front-end electronics

The detector signals has to be separated from the noise as early as possible. This is done by applying thresholds (analog or digital) to discriminate signals. Most of the tracking detectors use F1 cards with TDC digitizing the signal. The F1-TDC were designed with the flexibility to fulfill all requirements for the different detectors. In the case of the straw drift chambers, four bits of the time signal are reserved to indicate the channels which fired. As configuration parameters (time gates, thresholds, noise parameters) change frequently, they are stored in a volatile memory which needs to be programmed each time the electronics are powered up.

Event building and storage

The high data rate during the spill is absorbed in readout buffers (ROB), which can contain more data than a spill provides. The data are then merged into events by the event builders (EB) in a format called *raw data*. At this point, a second level of selection named online filter discards uninteresting events. The selected events are then sent to the central recording facilities of CERN.

The basics steps of the DAQ can be summarized as follow:

- 1. Clocks are synchronized at beginning of spills.
- 2. TCS sends a trigger signal to the CATCHs.
- 3. The CATCHs send trigger signals to the detectors.
- 4. The detectors send data (time, channel...) to the CATCHs.
- 5. The CATCHs send detector data to readout buffer (ROB) for the 4.8s spill time.
- 6. The ROBs send data to event builders (EB), where data of the same trigger signal are grouped as one event.

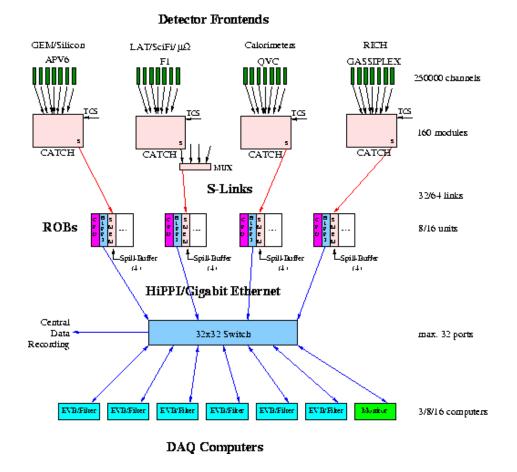


Figure 3.4: Overview of the DAQ system.

- 7. Useless events are removed by Online Filter (a second level of trigger system).
- 8. Events are sent to permanent storage.

3.1.10 Data reconstruction

The data stored at the central recording facilities of CERN contains detector information from every stored event. The reconstruction of physics elements (4-vectors, tracks, vertex...) from the raw data is carried out by the C++ program named CORAL (COmpass Reconstruction Algorithm Library) [2]. A schematic representation of the reconstruction software is shown in figure 3.5. First, the program *decodes* the detector information from the raw data and then groups together channel signals that are associated to the same particle. During the *clustering* phase, detector signals associated to the same particle are grouped together. After clustering, tracks are reconstructed as explained below. The information of the tracking detectors is used to reconstruct trajectories of charged particles

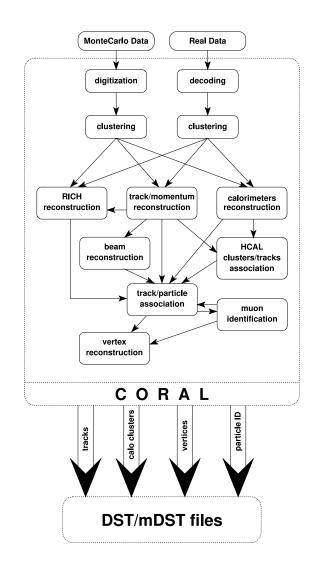


Figure 3.5: Schematic representation of the COMPASS reconstruction software which can have either raw data or Monte Carlo simulated data as input.

and to determine their momenta. Hadron clusters are used to separate muons and hadrons as explained in section 3.1.8. With tracks and particle identification, the vertex (primary and secondary) can be reconstructed. Finally, the reconstruction output, named mini Data Summary Tapes (mDST), is saved in a format of a ROOT [4] tree. The output size is a factor 100 smaller than the raw data input.

Tracking

To reconstruct the tracks, CORAL divides the clusters into different regions of the spectrometer. The section limits are defined by the magnetic field and high density material. In those regions, the trajectories segments are almost straight lines. The segments are then connected by a procedure called bridging using a 3D mapping of the magnetic field between segments. The tracks are then tuned according to the material that they have crossed.

Vertexing

After tracking, CORAL scans over the reconstructed tracks and identifies as the scattered muon a positive track compatible with the hodoscope hits as given in the trigger matrix⁵. The primary vertex is found by extrapolating the tracks inside the target. The primary vertex position is at the crossing of the incident muon with the meeting points of the other tracks in the target.

Finally, the output mDST files are used for analysis with the help of the program PHAST [42]. It contains libraries that allow to easily calculate physics quantities and to create selected subsamples, called microDST (μ DST), adapted to different analysis.

3.2 The straw drift chambers

At large angles, the tracking environment requires different detector characteristics than for the small angles. The rate is lower by few orders of magnitude, but the area to cover is much larger. Hence, the number of channels can be reduced while still keeping a reasonable level of occupancy. Gaseous detectors have the advantages of having a low material budget but care has to be taken for stability over large area coverage. The straw drift chambers fit very well these criteria. At COMPASS, each straw drift chamber covers about 9 m^2 with straws as long as 3.6 m with a space resolution of about $190 \,\mu\text{m}$ keeping a low 0.2%radiation length for a detector⁶ (excluding the detector gas).

 $^{^5}$ For a standalone calorimeter trigger, a minimum of hits is required downstream of the first or second absorber.

 $^{^{6}}$ This value corresponds to a double layer, i.e. two planes of straws. The detector components will be explained below.

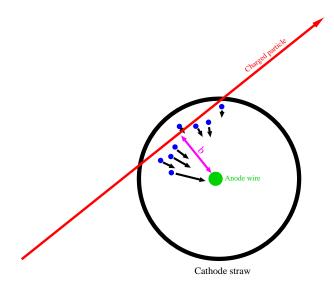


Figure 3.6: Charged particle crossing a straw and ionizing the gas along its path. The primary electrons are attracted towards the positively charged wire (anode). The pink parameter b represents the closest distance to the wire along the trajectory of the particle.

3.2.1 General concept

The straw drift chambers are ionization detectors. They are based on the collection of electrons and ions created by charged particles passing through a gas. A straw is made of three basic components: an anode wire, a cathode cylinder and ionizable gas. The cylindrical shape creates a simple radial electric field:

$$E(r) = \frac{CV_0}{2\pi\epsilon} \frac{1}{r} \tag{3.2}$$

where C is the capacitance per unit length, V_0 the applied voltage, ϵ the electric permittivity of the gas and r the distance to the wire. When a charged particle passes through the straw volume, the gas gets ionized and the liberated electrons are attracted towards the anode wire as represented in figure 3.6. On their way to the anode, the electrons ionize further the gas so the ionization accelerates resulting in an avalanche of electrons. The COMPASS straw drift chambers work in the proportional regime, which means that the number of gathered electrons at the anode is proportional to the number of primary electron-ion pairs. The proportionality factor is called gain.

The measured signal is actually created by the displacement of the charges which changes the voltage. It turns out that the positive ions are the main contributors to the voltage change. The time for the pulse to arrive to the anode wire depends on the distance from the closest primary electrons to the wire (which can be approximated by the shortest distance between the track and the wire i.e. distance **b** in figure 3.6).

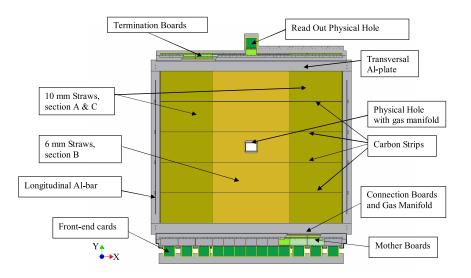


Figure 3.7: Schematic view of a COMPASS straw drift chamber (type X)[28].

3.2.2 Components

Straw tubes

There are two types of straws with different diameters: 6 mm (actually 6.15 mm outer diameters) and 9 mm (actually 9.65 mm). The 9 mm straws are situated in the outer sections where the rates are lower and a straw can cover a larger area without occupancy problems. Both have been shown to have the same space resolution [28]. The anode wires have 30 μ m diameters and are centered in the straw tubes by two end-plugs and four small plastic spacers positioned at intervals of about 60 cm along the tubes. The spacers cause a strong drop of efficiency for about one centimeter along the straw. Near the straw wall, a charged particle creates less electron-ion pairs, this causes a sudden drop of efficiency in the last 500 μ m [58]. The straws are filled with a fast counting gas mixture of Ar/CO₂/CF₄ (74/6/20) which at nominal voltage (1950 V) corresponds to a gain of 6·10⁴. There are in total 12440 straw tubes.

Straw planes

There are two types of straw planes: vertical (X-type) and horizontal (Y-type), a X-type plane schematic representation is shown in figure 3.7. Both types have outer sections (section A and C in figure 3.7) with 9 mm straws and a central section (section B in figure 3.7) with 6 mm straws. The straw tubes are glued together which gives more stability compared to individual straw tubes. To avoid the beam region, the central section of each plane has a dead zone, named physical hole, of about $20 \times 20 \text{ cm}^2$ with shorter straws above and below. This keeps the beam from overwhelming the straws and doubles the number of channels in the most occupied area. The X and Y-types have a different amount of straws

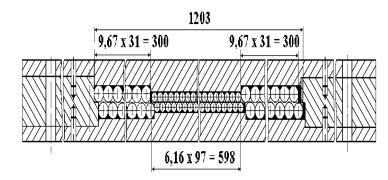


Figure 3.8: Cross section of a double layer, looking into the straws.

and different straw lengths.

Double layer

A complete straw detector is actually a double layer: two planes, one in front of the other shifted by a straw radius. The shift helps to avoid left/right ambiguity. Indeed, the information that is given by a single straw is the drift time, which can be converted in distance from the wire. This distance can either be left or right from the wire⁷. This ambiguity can be resolved by straws (in front or behind) shifted by half a diameter. A transverse cross section of a double layer is shown in figure 3.8. There are in total 15 double layers.

Chamber frame

The straw drift chambers were designed to fit many chambers in the limited space between SM1 and the RICH. The material budget had to be minimal to avoid secondary interactions, so the frame material was chosen to be aluminum. The chambers had to fulfill the challenging requirements of covering an area of about 9 m^2 within a 40 mm thickness. The end of the straws of a double layer are glued gas tight between each side of the aluminum frame. The frame also serves as gas manifold where the gas streams from the bottom through the manifold and through the end-plugs into the straws and exits through the manifold at the top. A transverse view of the straw ends in the frame is shown in figure 3.9. The straw layers are supported by carbon fiber strips attached to the frame. As carbon is practically not influenced by temperature, it keeps the straws stable. The chamber frame also supports the electronics and the cooling water distributor⁸.

⁷This is under the safe assumption that the track hits the plane perpendicularly.

 $^{^{8}}$ It is to be noted that the water cooling system was not installed until 2006, so it was not part of the setup for the physics analysis in the later chapters.

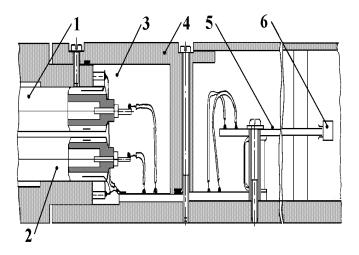


Figure 3.9: Lateral cross section of the bottom of a straw drift chamber.

Gas volume

The straws are very sensible to humidity. In order to keep the straw tubes straight, they have to be kept under small tension. A change in humidity can either increase or decrease the length of the tubes, which will stress the frame or bend the straws. The latter can affect significantly the performance of the detector. In order to minimize the effect of the humidity, the double layers are surrounded by a dry gas contained in a protective volume. The protective volume is made of two foils glued onto the frame and keeps the humidity constant and below 10%. These $12 \,\mu$ m thick aluminized Mylar foils have a very low water vapor transmission coefficient (smaller that $0.05 \,\text{g/(m^2 day)}$) at 25° C and 70% relative humidity). A gas flow of about 30 l/hour is running through the protective volume. Humidity sensors are placed within every double layers to make sure that the humidity levels are always within the working conditions.

Readout electronics

Straws are connected to mother boards (MB) in group of 64. The MB distributes the high voltage and acts as an interface to the front-end card. The front-end F1 card gets the signal from the mother board and amplifies the signal. As written in section 3.1.9, the F1 cards have a TDC incorporated to reduce cabling and signal degradation. The MB can also test the readout system by injecting a charge directly to the amplifier inputs. A front-end F1-TDC card consists of eight preamplifiers and eight F1-TDC chips with, in the straw case, a 130 ps digitization. Each F1-TDC chip digitizes eight channels. The threshold of the preamplifier can be set individually for each channel (straw).

Submodules and modules

A straw plane used alone can measure precisely only one dimension in the detector plane. Therefore, each vertical double layer is grouped with a horizontal double layer. This would be enough to get the position of one track, but for more tracks, ambiguity is possible. When two tracks pass the detector simultaneously, four straws send a signal, two horizontal and two vertical crossing at four point like a hash sign (#). To know on which of those four crossing points actually lie the trajectories, an inclined X-type double layer, $\pm 10^{\circ}$ w.r.t. the vertical direction, is included. The (counter)clockwise inclined double layer is referred to as U (V) chamber. A group of three double layer (vertical X-type, Y-type and an inclined double layer) is called sub-module. Two sub-modules joined together (with different inclined double layers tilted in opposite direction) form a module. In 2004, there were one module (ST03) and three submodules (ST04, ST05, ST06).

3.2.3 The front-end cooling system

When double layers are grouped into a module, the order of the double layers is (from upstream to downstream of the beam direction): X, Y, U, V, Y, X planes. The inclined layer U,V are "sandwiched" in the middle of the module. In this confined space, the electronic readout of the inclined detector are into a (partially isolated) volume heated by the electronic chips. Before the year 2006, a standard air blowing cooling system was in function, but the electronic chips reached temperature above 50°C. The design of an improved cooling of the front-end cards had challenging limitations:

- Available space below 2 mm.
- Non-conducting material is mandatory to avoid capacity coupling to the front-end.
- Low cost since there are about 200 cards.
- 20 Watt \rightarrow 5 liters/h ($\Delta T_{water} = 2 \text{ K}$) to get rid of.

The final design

The cooling system, designed and constructed by Dr. Reiner Geyer⁹, consists of a closed (distilled) water circuit passing by the front-end card surfaces to transport their heat to a heat exchanger. A simplified circuit is shown in figure 3.10, and a detailed version in figure 3.11. To respect the geometrical constraints, the cooling on the front-end cards is realized with thin cooling plates as shown in figures 3.12 and 3.13. The cooling unit consists of two cooling plates linked with a brass connector as shown in figure 3.12. The cooling plates are made of fiber glass, the same type as used for printed circuit. The front-end card sits between the two plates such that the chips on both sides are cooled. Glass slides (the kind used to hold liquids for microscope) are glued to fill the gap between the cooling plates and

 $^{^{9}}$ Manuel Hubner contributed to the design and the author of this document to the construction.

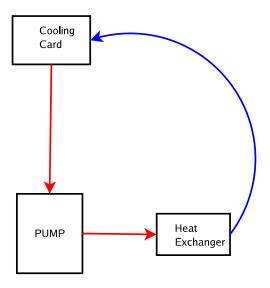


Figure 3.10: Conceptual drawing of the straw cooling system. The blue arrow represent the path of cooled water on its way to the cooling card where it absorbs heat from the electronic chips. The red arrows represent the path of heated water on its way to the heat exchanger.

the chips of different heights. The cooling plates are three 500 μ m layers glued together as shown in figure 3.12 for the two cooling plates of a unit. The middle layer is cut in such a way to make a path for the cool water through the plates. Figure 3.13 shows the assembled card with the flow direction. The glass slides are glued with silicon glue to the plates and to the Kapton tape applied on four chips. The Kapton tape is applied to help an eventual removal of the plates from the card and to protect the chips. The space available (about 1.5 mm) limits the thickness of the plates which are also limited by their elastic property; If they are too thin and/or the cut path too wide, the two outer layers collapse and can reduce the space enough to affect significantly the water flow. The plates are glued to the brass connector with Araldite.

3.2.4 Drift time calibration

It has been previously noted [54] that the drift reference start time T_0 of the straw signal is not constant. This leads to a wrong drift time estimation which ultimately leads to a wrong track position. It was shown that the T_0 could be wrong by as much as 14 ns for particular cases. This error makes the data unreliable. A major effort of Sasha Zvyagin and the author of this document has been dedicated to the investigation and individual calibration of the 400 cards [57]. The procedures has to be repeated every year and has proven successful to improve the quality of the tracking.

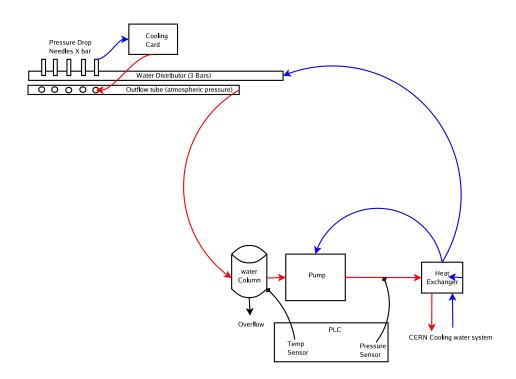


Figure 3.11: Detailed drawing of the straw cooling system. The blue arrow represents the path of cooled water on its way to the cooling card where it absorbs heat from the electronic chips. The red arrows represent the path of heated water on its way to the heat exchanger.

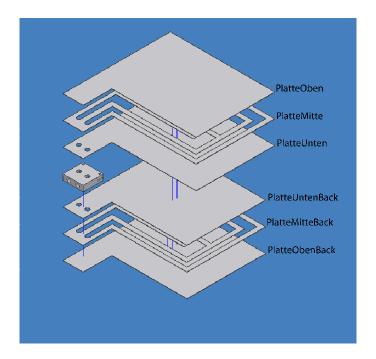


Figure 3.12: Elements of a cooling unit. Each cooling plate has a thickness of $500 \,\mu\text{m}$. The water manifold in the middle is made out of brass for its low interaction with water. The electronic card will be inserted between the third and the fourth layer (PlatteUntenBack and PlatteUnten) and glass slides will fill the gap between the cooling plates and the two chips (ASD8 preamplifier and F1-TDC). The cross section of the water channel is about $15 \times 0.5 \,\mathrm{mm}^2$

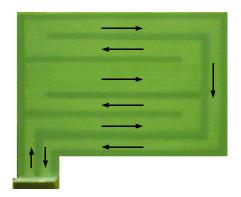


Figure 3.13: Picture of a cooling plate. The arrows show the direction of the water flow.

Chapter 4

Theoretical framework

4.1 Deep inelastic scattering

Deep inelastic scattering (DIS) processes reveal the internal structure of hadrons. In the following sections, different models of the nucleon structure will be presented. Starting from the point-like nucleon, more complex models will be introduced with distribution functions of the constituents, the so-called partons. Figure 4.1 shows the Feynman diagram of one-photon exchange lepton (e, μ) scattering off the nucleon (N).

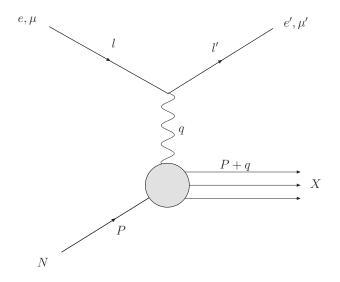


Figure 4.1: Deep inelastic scattering diagram. The l and l' are the 4-vectors of the incoming and scattered lepton, respectively. P is the 4-vector of the nucleon and X represents the remaining final state excluding the scattered lepton. The final state X usually includes additional hadrons.

4.1.1 Basic variables

All the following definitions are based on the single photon exchange shown in figure 4.1. In the variable definitions, the exchange photon 4-momentum is defined from the incoming and scattered lepton. It will be shown later that radiative processes such as those shown in figure 4.6 make this interpretation dubious. But for simplicity, the 4-momentum transfer of the lepton is named the 4-momentum of the exchange photon.

Muon variables

- l^{μ} : 4-momentum of the incoming lepton.
- l'^{μ} : 4-momentum of the scattered lepton.
- P^{μ} : 4-momentum of the target nucleon.
- q^{μ} : 4-momentum transfer of the muon (equals the 4-momentum of the exchanged virtual photon in case of single photon exchange).
- Θ : Angle between incoming and scattered muon, in the laboratory system.
- $Q^2 = -q^2$: (Negative invariant mass squared of the exchange photon in case of single photon exchange).
- E_{γ} or $\nu = E E'$: (Energy of the exchange photon in the laboratory system in case of single photon exchange).
- $W^2 = (P + q)^2$: (Invariant mass squared of the (virtual) photon-nucleon system X in case of single photon exchange).

Definition	General	Lab
E_{γ}, ν	$\frac{P \cdot q}{M}$	E-E'
q	l - l'	
Q^2	$-q^{2}$	$\approx 4EE'sin^2\frac{\Theta}{2}$
W^2	$(P+q)^2$	$M^2 + 2M\nu - \overset{\scriptscriptstyle 2}{Q}{}^2$
x_{Bj}	$\frac{Q^2}{2P \cdot q}$	$\frac{Q2}{2M\nu}$
y	$\frac{P \cdot q}{P \cdot k}$	$\frac{\nu}{E}$

Table 4.1: Inclusive variable definitions.

Hadron variables

In the events where there is an observed hadron h (in addition to the -normally observedhadron) in the final state X of figure 4.1, the process is semi-inclusive deep inelastic scattering (SIDIS). Then, the kinematic variables of the observed hadron have to be defined.

- h^{μ} : Hadron 4-momentum, in the laboratory system.
- E_h : Energy of the hadron, in the laboratory system.
- p: Magnitude of the hadron momentum, in the laboratory system.
- p_T : Transverse momentum of the hadron w.r.t. virtual photon direction.
- ${}^{lab}p_T$: Transverse momentum, in the laboratory system, of the hadron w.r.t. the beam direction.
- p_L : Longitudinal momentum, in the laboratory system, of the hadron w.r.t. virtual photon momentum.
- ϕ : Azimuthal angle of the hadron w.r.t. the muon scattering plane.
- θ : Polar angle of the hadron w.r.t. the virtual photon direction.
- ${}^{lab}\theta$: Polar angle of the hadron w.r.t. the laboratory z-coordinate (beam direction).
- $z = \frac{P \cdot h}{P \cdot q}$: Fraction of the virtual photon energy carried by the hadron. With the laboratory variables, $z = \frac{E_h}{\nu}$.
- $y = \frac{1}{2} ln \frac{E_h + p_L}{E_h p_L}$: Rapidity calculated in the laboratory system.
- $\eta = -ln(tan\frac{\theta}{2})$: Pseudorapidity of the hadron calculated in the laboratory system and w.r.t. the direction of the virtual photon. $\approx y$
- ${}^{lab}\eta = -ln(tan {}^{lab}\theta {}^2)$: Pseudorapidity of the hadron calculated in the laboratory system and w.r.t. to the beam muon direction.

4.1.2 Elastic scattering

Although deep inelastic scattering reveals the internal structure of hadrons, the description of structureless particles will still be of use. For one, the nucleon is usually probed with a lepton (a muon in the case of COMPASS) which is structureless. Moreover, a particle with structure can be approximated by a composition of structureless elements as in the quark parton model as described below.

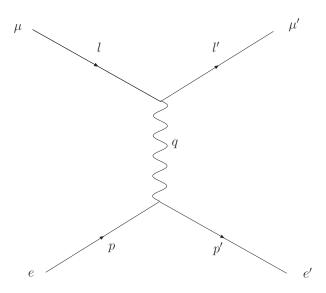


Figure 4.2: Feynman diagram of elastic muon-electron scattering. The diagram is the same for muon-quark elastic scattering.

An example of elastic scattering is the electromagnetic interaction between two point-like particles, like an electron and a muon. Figure 4.2 shows the Feynman diagram for elastic scattering. In this process, the initial and final particles are the same, that is $p^2 = p'^2$ such that energy-momentum conservation at the lower vertex in figure 4.2 gives

$$(p+q)^2 = p^2 \Rightarrow q^2 = -2p \cdot q. \tag{4.1}$$

From this, the Bjorken variable reduces to

$$x_{Bj} = \frac{Q^2}{2p \cdot q} \stackrel{elastic}{=} 1. \tag{4.2}$$

The invariant amplitude from the Feynman rules for an elastic process is:

$$\mathcal{M} = -ee'\overline{u}(l')\gamma^{\mu}u(l)\frac{1}{q^2}\overline{u}(p')\gamma_{\mu}u(p), \qquad (4.3)$$

where u, v are Dirac spinors and γ^{μ} the four Dirac γ -matrices¹. Two different charges, e and e' are assigned in order to have a more general formula also applicable to muon scattering off particles with different charges. According to Fermi's Golden rule number 2, the cross section is obtained from $|\mathcal{M}|^2$. For the unpolarized case, the spin states must be averaged with the factor $\frac{1}{(2s_e+1)(2s_{\mu}+1)} \sum_{spins}$, where $s_{\mu}(s_e)$ is the spin of the muon (electron).

In the case of spin $\frac{1}{2}$ particles, the cross section is proportional to

¹For more details see, for example, [45].

$$\langle |\mathcal{M}|^2 \rangle \equiv \frac{1}{4} \sum_{spins} |\mathcal{M}|^2$$
 (4.4)

It is common practice to separate $\langle |\mathcal{M}|^2 \rangle$ into its muon (l,l') and electron (p, p') part defined as tensors. The muon tensor is then

$$L_{muon}^{\mu\nu} = \frac{1}{2} \sum_{muon-spins} [\overline{u}(l')\gamma^{\mu}u(l)][\overline{u}(l')\gamma^{\nu}u(l)].$$
(4.5)

Using trace algebra properties, the muon tensor can be rewritten the following way:

$$L_{muon}^{\mu\nu} = 2(l'^{\mu}l^{\nu} + l'^{\nu}l^{\mu} - (l' \cdot l - m^2)g^{\mu\nu}), \qquad (4.6)$$

where m is the muon mass. The electron tensor is defined similarly. The contraction of the muon and electron tensors gives

$$L^{\mu\nu}_{muon}L^{e}_{\mu\nu} = 8((l' \cdot p')(l \cdot p) + (l' \cdot p)(l \cdot p') - m^{2}(p' \cdot p) - m^{2}_{e}(l' \cdot l) + 2m^{2}m^{2}_{e}).$$
(4.7)

Neglecting the muon (m) and electron (m_e) masses it becomes

$$L^{\mu\nu}_{muon}L^{e}_{\mu\nu} = 8((l' \cdot p')(l \cdot p) + (l' \cdot p)(l \cdot p'))$$
(4.8)

which can be rewritten as function of the Mandelstam variables 2 as

$$L^{\mu\nu}_{muon}L^{e}_{\mu\nu} = 2(s^2 + u^2).$$
(4.9)

Thus, combining 4.4 and 4.9, the unpolarized invariant amplitude is

$$\langle |\mathcal{M}|^2 \rangle = \frac{e^2 e'^2}{Q^4} 2(s^2 + u^2)$$
 (4.10)

which, noting that u/s = y - 1, can be rewritten as

$$\langle |\mathcal{M}|^2 \rangle = \frac{e^2 e'^2}{Q^4} 2s^2 (1 + (1 - y)^2).$$
 (4.11)

The nucleon is also a spin- $\frac{1}{2}$ particle and if it were a structureless particle, it would have a cross section proportional to equation (4.10). This is the case for small Q^2 , where the virtual photon wavelength is so long that it cannot *resolve* the constituents of the nucleon.

Figure 4.3 shows that the nucleon is a particle with structure by comparing lepton-nucleon scattering with the point like ansatz. Indeed, as Q^2 increases, the cross section is no longer proportional to equation (4.10).

$${}^{2}s = (p+l)^{2}, t = (l-l') \text{ and } u = (l'-p)^{2}$$

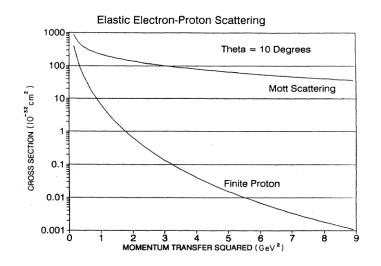


Figure 4.3: Point-like cross section compared to electron-proton scattering of single photon exchange taken from [49]. The Mott cross section has the $1/Q^4$ dependence as in (4.11), obviously the dependence is stronger than $1/Q^4$. Indeed, the Rosenbluth formula adds two structure function that represents the charge and magnetic moment distributions inside the proton. These functions are dependent of Q^2 and explain the stronger decrease of the cross section.

4.1.3 Muon-hadron scattering

At COMPASS, muons scatter off nucleons. Just as a lepton tensor was introduced, the hadron tensor is defined. The complex final state of DIS cannot be described by a simple tensor made out of a Dirac spinor. Ignorance of the hadronic structure imposes the use of a general form using $g^{\mu\nu}$ and independent momenta with parameters, $W_{1,2}$, that have to be determined experimentally³:

$$W_{\mu\nu} = -W_1(-g_{\mu\nu} + \frac{q_\mu q_\nu}{q^2}) + \frac{W_2}{M^2}(P_\mu - \frac{P \cdot q}{q^2}q_\mu)(P_\nu - \frac{P \cdot q}{q^2}q_\nu), \qquad (4.12)$$

where M is the mass of the nucleon and $W_{1,2}$ are two functions depending on inclusive variables that parametrize the structure of the hadron. Contracting with the lepton tensor gives (see e.g. equation (8.31) in [45])

$$L^{\mu\nu}W_{\mu\nu} = 4(l \cdot l')W_1 + 2\left(2(P \cdot l)(P \cdot l') - (l \cdot l')M^2\right)\frac{W_2}{M^2}.$$
(4.13)

In the laboratory frame it becomes

$$L^{\mu\nu}W_{\mu\nu} = 4EE' \left(\cos^2 \frac{\Theta}{2} W_2(\nu, Q^2) + \sin^2 \frac{\Theta}{2} 2W_1(\nu, Q^2) \right).$$
(4.14)

4.1.4 Cross sections

The cross section, σ , is related with the likelihood of interaction between particles. This section shows how to determine $\sigma^{\mu X \to \mu' Y}$ from Fermi's Golden rule number 2⁴:

$$\Phi \times \sigma(i \to f) = \int w_{fi} \times \text{[final state phase space]}$$
 (4.15)

where Φ is the *initial flux* and w_{fi} the transition rate per unit of volume V and time T of the interaction:

$$w_{fi} = \frac{|S_{fi}|^2}{VT},\tag{4.16}$$

where S_{fi} , the transition amplitude, is related to the matrix element in the following way:

$$S_{fi} = i(2\pi)^4 \delta^4(p_i - p_f) \mathcal{M}_{if}$$
(4.17)

where p_i and p_f are the four 4-momenta of the initial and final state, respectively. Combining (4.17) and (4.16) leads to

$$w_{fi} = (2\pi)^4 \frac{\delta^4 (p_i - p_f) |\mathcal{M}_{if}|^2}{V^4}, \qquad (4.18)$$

where the time T canceled out with the one resulting from squaring $\delta^4(p_i - p_f)$ from (4.17).

³ This tensor form was obtained by using some conservation quantity such as parity which is appropriate for muon-nucleon scattering.

⁴ This demonstration follows the steps of [45].

Number of available final states

A single particle in a volume V within the momentum interval p and $p + d^3p$ has $\frac{Vd^3p}{(2\pi)^3}$ possible states. The volume is normalized to contain 2E particles which have to share the number of available states, then the following number of states per particle is

Number of states per particles
$$= \frac{V d^3 p}{(2\pi)^3 2E}$$
. (4.19)

Thus, the number of available states into the momentum elements for the two particles X, l' is

Number of available final states =
$$\frac{Vd^3p_X}{(2\pi)^3 2E_X} \frac{Vd^3k'}{(2\pi)^3 2E'}$$
. (4.20)

The initial flux Φ

It is easier to calculate first in the laboratory reference system and then write it in an invariant form to have the general definition. The number of particles passing through unit area per unit time is $|\mathbf{v}_k| 2E/V$ and the number of target particles per unit volume is $2E_t/V$. Then, the initial flux is

$$\Phi = |\mathbf{v}_k| \frac{2E}{V} \frac{2E_t}{V},\tag{4.21}$$

where subscript t stands for target. The volume cancels out when equations (4.21), (4.20) and (4.18) enter (4.15) so it will be omitted from now on. In general, when both beam and target particles are moving:

$$\Phi = |\mathbf{v}_l - \mathbf{v}_t| 2E2E_t \tag{4.22}$$

which can be rewritten in invariant form

$$\Phi = 4((l \cdot P)^2 - m_{\mu}^2 m_t^2)^{\frac{1}{2}}.$$
(4.23)

In the case of fixed target $(P = (m_t, 0, 0, 0))$ and neglecting the incoming particles mass, the flux reduces to

$$\Phi = 4m_t E. \tag{4.24}$$

Muon-Quark

For a target experiment, the quark (eventually in a nucleon) is at rest. Using equation (4.15) without the integration, (4.18), (4.20) and (4.24) the differential cross section relation is

$$d\sigma = \frac{1}{(2E)(2m_q)} \frac{\langle |\mathcal{M}_{if}|^2 \rangle}{4\pi^2} \frac{d^3k'}{2E'} \frac{d^3p'}{2E_0'} \delta(p+k-p'-k')$$
(4.25)

$$= \frac{1}{4m_q E} \frac{\langle |\mathcal{M}_{if}|^2 \rangle}{4\pi^2} \frac{1}{2} E' dE' d\Omega \frac{d^3 p'}{2E'_0} \delta(p+q-p'), \qquad (4.26)$$

where the initial energy of the quark at rest is its mass, m_q . Since the quarks are structureless, the cross section of the muon on quarks is exactly the same as for the muon electron scattering except for the fact that the charge is different. In section 4.1.2, the charge of the electron was carefully kept unspecified, e', so formula (4.10) can be recycled for the muon-quark scattering in (4.26). Integrating over the final quark phase-space, d^3p' , and the energy, dE', and changing the variable Ω to Q^2 it becomes

$$\frac{d\hat{\sigma}}{dQ^2} = \frac{2\pi\alpha^2}{\hat{s}^2} \frac{\hat{s}^2 + \hat{u}^2}{Q^4} e_i^2, \qquad (4.27)$$

where e_i is the quark charge in electron charge units (i.e. $e' = e_i e$) and the *hatted* mandelstam variables are for the muon quark system:

$$\hat{s} = (l+k)^2,$$
(4.28)

$$\hat{t} = (l - l')^2, \tag{4.29}$$

$$\hat{u} = (k - l')^2. \tag{4.30}$$

(4.31)

In terms of the y variable, the differential cross section becomes

$$\frac{d\sigma}{dy} = \frac{2\pi\alpha^2}{Q^2} \left(1 + (1-y)^2\right) \hat{s}e_i.$$
(4.32)

Muon-hadron

Hadrons are not fermions that can simply be described by Dirac spinors as the muons in (4.3). Using the tensor product (4.14) and the relation $d\sigma \sim L_{\mu\nu}W^{\mu\nu}$ inspired by (4.15), (4.18) and tensor separation (4.4) of the invariant amplitude of the elastic case gives the following differential cross section:

$$\frac{d\sigma}{dE'd\Omega} = \left(\frac{4\alpha^2 E'^2}{Q^4}\right) \left(W_2(\nu, Q^2)\cos^2\frac{\Theta}{2} + 2W_1(\nu, Q^2)\sin^2\frac{\Theta}{2}\right).$$
(4.33)

It is common practice to rewrite the cross section as function of (x_{Bj}, y, Q^2) and the structure functions $F_1 = W_1$ and $F_2 = \nu W_2/M^2$:

$$\frac{d\sigma}{dx_{Bj}dQ^2} = \left(\frac{4\pi\alpha^2}{x_{Bj}Q^4}\right) \left(F_2(x_{Bj},Q^2)(1-y) - F_1(x_{Bj},Q^2)x_{Bj}y^2\right).$$
 (4.34)

These functions have been determined by several experiments as can be seen for F_2 in figure 4.4.

In the single photon exchange approximation, the cross section $\sigma_{1\gamma}$ can be described as the sum of the total cross section for absorption of transverse, σ_T , and longitudinal, σ_L ,

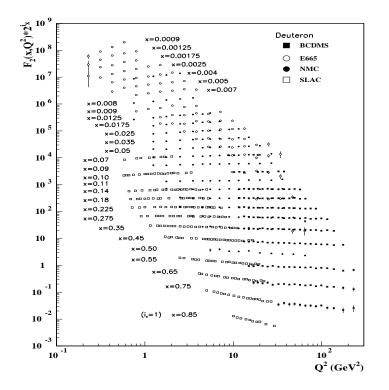


Figure 4.4: Structure function $F_2(x_{Bj}, Q^2) * 2^{i_x}$ where $i_x = 1, 2, 3...$ for x = 0.85, 0.75, 0.65...

virtual photons⁵:

$$\frac{d^2\sigma_{1\gamma}}{dx_{Bj}dQ^2} = \Gamma(\sigma_T(x_{Bj}, Q^2) + \epsilon\sigma_L(x_{Bj}, Q^2)), \qquad (4.35)$$

where Γ is the flux of transverse virtual photons,

$$\Gamma = \frac{\alpha}{4\pi^2} \frac{KE'}{q^2 E} \left(\frac{2}{1-\epsilon}\right),\tag{4.36}$$

where ϵ is the degree of longitudinal polarization,

$$\epsilon = \left(1 + 2(1 + \nu^2/q^2)tan^2(\Theta/2)\right)^{-1}$$
(4.37)

and

$$K = \frac{W^2 - M^2}{2M}.$$
(4.38)

It is useful to define the ratio of those two cross sections:

$$R \equiv \frac{\sigma_L}{\sigma_T}.\tag{4.39}$$

This value has been determined in the kinematics of COMPASS by the previous experiment NMC [19] and can be seen in figure 4.5. When needed, a fit on world data from [5], including NMC, will be used. The cross sections σ_T and σ_L are related to the structure functions F_1 and F_2 by

$$\sigma_T(x_{Bj}, Q^2) = \frac{4\pi^2 \alpha}{Q^2} 2x_{Bj} F_1(x_{Bj}, Q^2), \qquad (4.40)$$

$$\sigma_L(x_{Bj}, Q^2) = \frac{4\pi^2 \alpha}{Q^2} F_L(x_{Bj}, Q^2), \qquad (4.41)$$

where

$$F_L = F_2 - 2x_{Bj}F_1. (4.42)$$

4.1.5 QED radiative effects

The previously defined single photon exchange cross section $\sigma_{1\gamma}$, (4.35), is only the lowest order of many interactions that compose the observed cross section. The other contributions to the observed cross section are named radiative corrections (to the cross section). The lowest order corrections are shown in figure 4.6. The observed cross section can then be written as

$$\sigma_{meas}(x_{Bj}, y) = \sigma_{1\gamma}(x_{Bj}, y) + \sigma_{\text{QED}}(\alpha) + \sigma_{\text{VAC}} + \dots, \qquad (4.43)$$

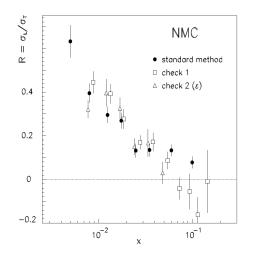


Figure 4.5: R determined by NMC [19] from proton and deuterium target with muon beam energies: 90, 120, 200, 280 GeV. The Q^2 interval was [0.5,75] (GeV/c)² with an average Q^2 ranging from $\langle Q^2 \rangle = 1.4$ to 20.6 (GeV/c)² for the different x-bins.

where σ_{QED} arise from the photon radiation shown in figure 4.6 and σ_{VAC} arise from the vaccum polarization. These corrections are summarized into one factor that links the observed cross section to the single photon exchange cross section:

$$\sigma_{meas}(x_{Bj}, y) = \frac{\sigma_{1\gamma}(x_{Bj}, y)}{\eta(x_{Bj}, y)},\tag{4.44}$$

where the contributions from all radiative effects are included in $\eta(x_{Bj}, y)$.

4.1.6 The Quark Parton Model

Knowing that the nucleon is an extended object with a DIS cross section depending only logarithmically on Q^2 , a first approximation of its structure can be realized by a number of free point-like constituents, the *partons*. In the quark parton model, the constituents are the quarks. Distribution functions $q_i(x)$ give the probability that the struck quark *i* carries a fraction *x* of the hadron momentum. The nucleon tensor can be written as a sum of point-like tensors, $w_{\mu\nu}$, with the structure of (4.6):

$$W_{\mu\nu} = \sum_{i} e_i^2 x q_i(x) w_{\mu\nu}.$$
 (4.45)

⁵Since the virtual photon has a mass q^2 , it is no longer forbidden to have a longitudinal polarization. But as $q^2 \to 0$, $\sigma_L \to 0$.

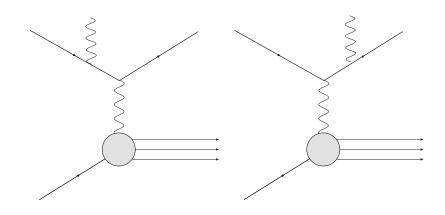


Figure 4.6: Lowest order QED radiative processes to be corrected to obtain the one-photon exchange of figure 4.1.

The contraction with the muon tensor is similar as in the elastic case, but with the distribution function factor so (4.9) would look like

$$L_{muon}^{\mu\nu}W_{\mu\nu} = \sum_{i} e_{i}^{2} x q_{i}(x) \delta(2q \cdot k - Q^{2}) 2(\hat{s}^{2} + \hat{u}^{2})$$
(4.46)

with the muon-quark Mandelstam variables defined in (4.31) and the parton 4-vector k^6 . The term $\delta(2q \cdot k - Q^2)$ reflects the fact that the partons are on-shell. A similar derivation as the one leading to (4.11) and (4.32) leads to:

$$\frac{d\sigma}{dxdQ^2} = \left(\frac{2\pi\alpha^2}{xQ^4}\right) \left(1 + (1-y)^2\right) \sum_i e_i^2 x q_i(x) \tag{4.47}$$

Rewriting the muon-hadron cross section (4.34) in a way that resembles equation (4.47), using the other structure function F_L defined in (4.42) gives

$$\frac{d\sigma}{dx_{Bj}dQ^2} = \left(\frac{2\pi\alpha^2}{x_{Bj}Q^4}\right) \left(F_2(x_{Bj},Q^2)(1+(1-y)^2) - F_L(x_{Bj},Q^2)y^2\right)$$
(4.48)

and comparing (4.48) and (4.47), the following relation emerges:

$$F_2(x_{Bj}, Q^2) = \sum_i e_i^2 x q_i(x).$$
(4.49)

Hence, in the quark parton model, the structure function F_2 is a function of one variable only, x. Since in this model a lepton scatters elastically off a quark carrying a momentum k = xP the relation (4.2) becomes here

$$1 = \frac{Q^2}{2k \cdot q} = \frac{Q^2}{2xP \cdot q} \tag{4.50}$$

⁶In this simple collinear parton model, the parton tensor is simply $k = (xP_0, 0, 0, 0, xP_z)$, but when the intrinsic momentum will be considered, the definition will not be so trivial.

which leads to

$$x = \frac{Q^2}{2P \cdot q} = x_{Bj}.\tag{4.51}$$

Thus in the QPM, the hadron momentum fraction carried by the struck quark x is associated with the kinetic variable x_{Bj} in the QPM. Replacing x by x_{Bj} in the distribution functions of equation (4.49) leads to the following relations:

$$F_2(x_{Bj}, Q^2) \Rightarrow F_2(x_{Bj}) = \sum_i e_i^2 x_{Bj} q_i(x_{Bj}),$$
 (4.52)

$$F_L(x_{Bj}, Q^2) = F_2(x_{Bj}) - 2x_{Bj}F_1(x_{Bj}) = 0.$$
(4.53)

Here, the structure of the hadron depends only on the fraction of momentum carried by the quarks and *not* on the mass of the probe, Q^2 . This is the famous Bjorken scaling predicted in [27] and confirmed by many experiments as shown in figure 4.4 and 4.7. The cross section behavior is in much better agreement with the elastic scattering on point-like constituents, contrary to the finite proton model shown in figure 4.3. These results from SLAC in the 1960s supported the idea of the point-like constituents of the nucleon which were ultimately identified as quarks, previously devised by Gell-Mann.

Of course, the agreement between the QPM and the experimental data is not perfect since the proton is not only made of three (valence) quarks, and the strong interaction has not yet been considered. Indeed, gluon interactions such as PGF and QCDC shown in figure 2.1 are not included in the the quark parton model described above. Bjorken scaling is no longer satisfied when considering gluon interactions and the parton densities thus become Q^2 dependent. However, the Q^2 dependence can be calculated perturbatively using socalled splitting functions. The resulting formalism is known as the DGLAP⁷ evolution equations, and leads to more general PDFs $q_i(x_{Bj}) \rightarrow q_i(x_{Bj}, Q^2)$. The following analysis do not consider the Q^2 dependence of the distribution functions.

4.1.7 Polarized deep inelastic scattering

Fermions are described by the Dirac equation:

$$H\psi = (\alpha \cdot P + \beta m)\psi, \tag{4.54}$$

where α and β are 4×4 matrices. The Hamiltonian *H* does not commute with the orbital angular momentum **L**, but rather with the *total* angular momentum:

$$\mathbf{J} = \mathbf{L} + \frac{1}{2}\Sigma,\tag{4.55}$$

where $\frac{1}{2}\Sigma \equiv \mathbf{S}$, is an intrinsic property of the same nature as the angular momentum. Quantum mechanics restricts \mathbf{L} magnitude squared to be of the form

⁷For Dokshitzer, Gribov, Libatov, Altarelli and Parisi.

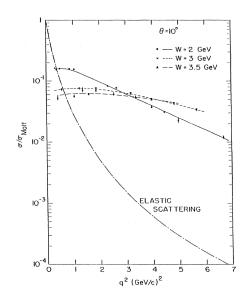


Figure 4.7: Electron-proton scattering cross section normalized by the Mott (point-like elastic) cross section in the DIS domain at SLAC [40]. This is completely different to the elastic electron-proton, where the cross section falls steeper than σ_{Mott} as shown in figure 4.3 revealing that the proton structure is not point-like. Here, in the DIS domain, the behavior is similar to point-like cross section. This suggests that the proton (or nucleon) is constituted of point-like particles.

$$L^2 = l(l+1)\hbar^2, (4.56)$$

where l = 0, 1, 2, ... are positive integers. For a given quantum number l, a measurement of the angular momentum in one direction L_z^8 has the following 2(l+1) valid eigenvalues in units of \hbar :

$$m_l = -l, -l+1, \dots, -1, 0, +1, \dots, l-1, l.$$

$$(4.57)$$

Similarly for the spin operator S^2 , the valid values are

$$S^2 = s(s+1)\hbar^2 \tag{4.58}$$

but here, the valid s are positive half integer $(0, \frac{1}{2}, 1, \frac{3}{2}, ...)$. Again, for a given quantum number s, a measurement of the spin angular momentum in one direction S_z has the following s(s+1) valid eigenvalues in units of \hbar :

$$m_s = -s, -s + 1, \dots, -1, 0, +1, \dots, s - 1, s.$$

$$(4.59)$$

The s are fixed for each type of particles. When the s are integers, as for the angular momentum, the particles are bosons. In the case of half integers, the particles are fermions. Since s is an intrinsic property, a particle is said to have spin s.

The spin quantum number s of the nucleon has been determined to be 1/2 [33] which leads to the eigenvalues of the one-directional projection m_s to $\pm \frac{1}{2}$. The nucleon one-directional spin projection (in units of \hbar) can be written as the sum of the contribution from its constituents⁹:

$$\frac{1}{2} = \frac{1}{2}\Delta\Sigma + \Delta G + L_q + L_g \tag{4.60}$$

where $\Delta\Sigma$ is the contribution from the quarks, ΔG from the gluons, L_q and L_g are the contributions from the angular momentum from the quarks and the gluons, respectively. Here is a list of different calculations of $\Delta\Sigma$:

- Simple non relativistic constituent quark model: $\Delta \Sigma = 1$
- Relativistic: $\Delta \Sigma \approx 0.75$
- Ellis-Jaffe (OPE and $\Delta s = 0$): $\Delta \Sigma \approx 0.6$

In 1988, the EMC experiment [20] determined the quarks contribution to be: $\frac{1}{2}\Delta\Sigma = 0.068 \pm 0.047 \pm 0.103$ in the quark parton model. The measurements and analysis has since then improved, but the fact remains: the quarks contribute only to a fraction of the nucleon spin. This was not the first time that the quarks were not the only *carrier*

⁸Only two orbital momentum components can be determined simultaneously, it is usually the magnitude square L^2 (S^2) and the z-component L_z (S_z)

 $^{^9\}mathrm{Most}$ of the literature drops the obvious \hbar and this will also be done here from now on.

of a nucleon's characteristic; the quarks, for example, carry only about 50% of the linear momentum, the rest being carried by the gluons. It then seems logical to measure the gluon contribution to the spin to look for the rest of the nucleon spin budget. This has been one of COMPASS main goals. Combined with results from other experiments, it is now unlikely that the gluons alone can explain the missing contribution. The only elements left from (4.60) are the angular momentum L_q and L_g which can be revealed by intrinsic motion of the partons.

4.2 Semi-inclusive deep inelastic scattering

4.2.1 Intrinsic transverse momentum of partons

In the previous sections, parton distribution functions (PDFs, e.g. $q_i(x_{B_i})$ in (4.45)) were defined to be function of x_{B_i} (and Q^2) only. Most of our knowledge of the inner structure of the nucleons is encoded into the PDFs. In the quark parton model, where the quarks are assumed collinear to the direction of the nucleon, this means that the quark distributions depend only on the nucleon momentum fraction carried by the quarks. It was noted earlier that intrinsic transverse momentum of the quark would lead to an azimuthal asymmetry of the cross section (Cahn effect [29]). Unintegrated parton distributions (transverse momentum dependent) are a natural extension of the usual integrated distributions and play a significant role in many physical processes. They can be extracted from experimental data and can be used to make predictions. One main difference between standard PDFs and unintegrated PDFs is that the latter does not appear in the definition of fully inclusive processes (when produced hadrons are not observed). When transverse momentum of a DIS produced hadron is observed, the unintegrated PDFs play a role, especially in the case of polarized SIDIS. The following analysis uses a simple implementation of intrinsic transverse momentum, k_{\perp} , fully taken into account by the quark distributions in the quark parton model. The framework of this analysis is based on the articles [17] and [16] which make predictions for COMPASS.

Kinematics of unintegrated semi-inclusive deep inelastic scattering

At leading order, the muon scatters off a quark with intrinsic motion as shown in figure 4.8, the initial k and final k' momenta are:

$$k = \left(xP_0 + \frac{k_{\perp}^2}{4xP_0}, \mathbf{k}_{\perp}, -xP_0 + \frac{k_{\perp}^2}{4xP_0}\right),$$
(4.61)

$$k' = k + q, \tag{4.62}$$

where x is the light-cone fraction, $(k_0^- - k_3)/(P_0^- - P_3)$, of the proton momentum carried by the parton and $\mathbf{k}_{\perp} = k_{\perp}(\cos\phi, \sin\phi, 0)$ is the parton transverse momentum, with $k_{\perp} \equiv |\mathbf{k}_{\perp}|$. The initial quark momentum fulfills the on-shell condition $k^2 = 0$ and for the struck quark:

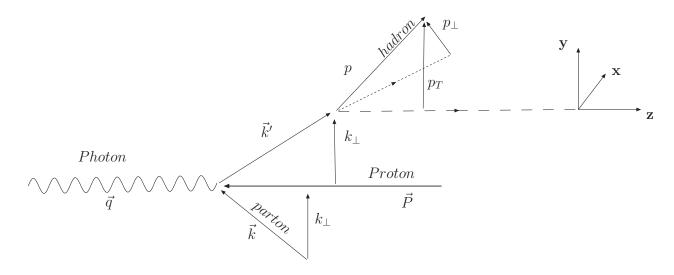


Figure 4.8: DIS diagram with parton k with intrinsic transverse momentum k_{\perp} . The final hadron is represented by p and gains transverse momentum p_{\perp} through the hadronization process.

$$k^{\prime 2} = 2k \cdot q - Q^2 = \hat{s} + \hat{u} + \hat{t} = 0.$$
(4.63)

This implies that

$$x = \frac{1}{2} x_{Bj} \left(1 + \sqrt{1 + \frac{4k_{\perp}^2}{Q^2}} \right).$$
(4.64)

Assuming small intrinsic transverse momentum such that $(k_{\perp} \ll xP_0)$, the quark 4-vector can be rewritten as

$$k = (xP_0, \mathbf{k}_\perp, -xP_0).$$
(4.65)

Neglecting the terms $\mathcal{O}(k_{\perp}^2/Q^2)$, the usual relations $x = x_{Bj}$ and $\mathbf{k} = x_{Bj}\mathbf{P} + \mathbf{k}_{\perp}$ are recovered.

A simple way to include transverse momentum to the hadron tensor is to insert a transverse momentum dependence into the parton distribution functions $q_i(x) \to f_i(x, k_{\perp})$ such that the collinear tensor from equation (4.45) becomes

$$W_{\mu\nu} = \sum_{i} e_i^2 \int dx dk_\perp^2 \left(\frac{1}{x}\right) f_i(x,k_\perp) w_{\mu\nu}, \qquad (4.66)$$

where the factor 1/x comes from the relativistic normalization of the states. The muonhadron scattering in the parton model, equation (4.46), then becomes

$$L_{muon}^{\mu\nu}W_{\mu\nu} = \sum_{i} e_i^2 x f_i(x, k_\perp) \delta(2q \cdot k - Q^2) 2(\hat{s}^2 + \hat{u}^2)$$
(4.67)

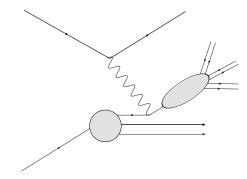


Figure 4.9: DIS diagram with hadronization.

and the cross section

$$\frac{d^2\sigma}{dx_{Bj}dQ^2} = \sum_i \int d^2 \mathbf{k}_\perp f_i(x,k_\perp) \frac{d\hat{\sigma}}{dQ^2} J(x_{Bj},Q^2,k_\perp)$$
(4.68)

again, $d\hat{\sigma}/dQ^2$ is the lepton-quark cross section given by equation (4.27) and where

$$J = \frac{x_{Bj}}{x} \left(1 + \frac{x_{Bj}^2 k_{\perp}^2}{x^2 Q^2} \right)^{-1}.$$
 (4.69)

If the parton could be measured directly after the interaction, the cross section would look like

$$\frac{d^4 \sigma^{lP \to l+p+X}}{dx_{Bj} dQ^2 d^2 \mathbf{k}_\perp} = \sum_i f_i(x, k_\perp) \frac{d\hat{\sigma}}{dQ^2} J(x_{Bj}, Q^2, k_\perp).$$
(4.70)

Fragmentation

The scattering processes discussed above have been considered until the first interaction with the parton. Confinement does not allow free quarks, consequently an experiment can only observe results of *hadronization* of the quark as shown in figure 4.9. The hadronization process is taken into account by the fragmentation functions¹⁰ (FFs) $D_q^h(\hat{z}, \mathbf{p}_\perp)$, the probability density for hadrons h to result from the fragmentation of the struck parton q. FFs are normalized such that

$$\int d\hat{z} d^2 \mathbf{p}_{\perp} D_q^h(\hat{z}, \mathbf{p}_{\perp}) = \langle n_h \rangle, \qquad (4.71)$$

where $\langle n_h \rangle$ is the average multiplicity of hadron h in the current fragmentation region of quark q. The variable \hat{z} is the light-cone fraction of the parton momentum carried by the resulting hadron. It is related to the usual hadronic z variable in the following way:

 $^{^{10}}$ Here, the dependence on fragmentation function on inclusive variable is not included although it depends on them [32], [50].

$$\hat{z} = z + \mathcal{O}\left(\frac{k_{\perp}^2}{Q^2}\right). \tag{4.72}$$

Similarly, p_{\perp} is the transverse momentum of the hadron h with respect to the parton direction \vec{k}' as can be seen in figure 4.8 and is related to the hadron transverse momentum with respect to the virtual photon direction as follow:

$$\mathbf{p}_{\perp} = \mathbf{p}_T - z\mathbf{k}_{\perp} + \mathcal{O}\left(\frac{k_{\perp}^2}{Q^2}\right).$$
(4.73)

The complete cross section of hadrons produced by DIS is then, as function of the muonquark cross section 4.27,

$$\frac{d^7 \sigma^{lP \to l+h+X}}{dx_{Bj} dQ^2 d^2 \mathbf{k}_\perp dz d^2 \mathbf{p}_\perp} = \sum_i f_i(x, k_\perp) \frac{d\hat{\sigma}}{dQ^2} J(x_{Bj}, Q^2, k_\perp) D_q^h(\hat{z}, \mathbf{p}_\perp)$$
(4.74)

or, as function of the observable variables,

$$\frac{d^5 \sigma^{lP \to l+h+X}}{dx_{Bj} dQ^2 dz d^2 \vec{p}_T} = \sum_i e_i^2 \int d^2 \mathbf{k}_\perp f_i(x, k_\perp) \frac{2\pi\alpha^2}{x_{Bj}^2 s^2} \frac{\hat{s}^2 + \hat{u}^2}{Q^4} D_q^h(\hat{z}, \mathbf{p}_\perp) \frac{z}{\hat{z}} \frac{x_{Bj}}{x} \left(1 + \frac{x_{Bj}^2 k_\perp^2}{x^2 Q^2}\right)^{-1}.$$
(4.75)

At
$$\mathcal{O}\left(\frac{k_{\perp}}{Q}\right)$$

Considering only the terms up to $\mathcal{O}\left(\frac{k_{\perp}}{Q}\right)$ such that from (4.64), (4.72), (4.73) and (4.69), the variables simplify to $x \approx x_{Bj}$, $\hat{z} \approx z$, $\mathbf{p}_{\perp} \approx \mathbf{p}_T - z\mathbf{k}_{\perp}$ and $J \approx 1$. The cross sections (4.74) or (4.75) then become

$$\frac{d^5 \sigma^{lP \to l+h+X}}{dx_{Bj} dQ^2 dz d^2 \mathbf{p}_T} = \sum_i e_i^2 \int d^2 \mathbf{k}_\perp f_i(x, k_\perp) \frac{2\pi\alpha^2}{x_{Bj}^2 s^2} \frac{\hat{s}^2 + \hat{u}^2}{Q^4} D_q^h(\hat{z}, \mathbf{p}_\perp).$$
(4.76)

4.2.2 Gaussian ansatz

A simple way to take into account the k_{\perp} dependencies for the parton density $f_i(x, k_{\perp})$ and the fragmentation $D_q^h(\hat{z}, \mathbf{p}_{\perp})$ functions is with a Gaussian:

$$f_i(x,k_\perp) = f_i(x) \frac{1}{\pi \langle k_\perp^2 \rangle} e^{-k_\perp^2 / \langle k_\perp^2 \rangle}$$
(4.77)

and

$$D_q^h(\hat{z}, \mathbf{p}_\perp) = D_q^h(\hat{z}) \frac{1}{\pi \langle p_\perp^2 \rangle} e^{-p_\perp^2 / \langle p_\perp^2 \rangle}.$$
(4.78)

From these definitions, the usual integrated PDFs and FFs are recovered by integrating over k_{\perp} and p_{\perp} :

$$\int d^2 \mathbf{k}_{\perp} f_i(x, k_{\perp}) = f_i(x) \tag{4.79}$$

and

$$\int d^2 \mathbf{p}_{\perp} D_q^h(\hat{z}, \mathbf{p}_{\perp}) = D_q^h(\hat{z})$$
(4.80)

At $\mathcal{O}\left(\frac{k_{\perp}}{Q}\right)$

In the case of the Gaussian ansatz, where only the terms up to $\mathcal{O}\left(\frac{k_{\perp}}{Q}\right)$ are kept, the differential cross section (4.76) can be integrated over $d^2\hat{k}_{\perp}$ analytically, resulting to

$$\frac{d^{5}\sigma^{lP \to l+h+X}}{dx_{Bj}dQ^{2}dzd^{2}\mathbf{p}_{T}} \approx \sum_{i} \frac{2\pi\alpha^{2}e_{i}^{2}}{Q^{4}}f_{i}(x_{Bj})D_{q}^{h}(z)$$

$$\left[1 + (1-y)^{2} - 4\frac{(2-y)\sqrt{1-y}\langle k_{\perp}^{2}\rangle zp_{T}}{\langle p_{T}^{2}\rangle Q}cos(\phi_{h})\right]\frac{1}{\pi\langle p_{T}^{2}\rangle}e^{-p_{T}^{2}/\langle p_{T}^{2}\rangle},$$

$$(4.81)$$

$$(4.81)$$

$$(4.82)$$

where

$$\langle p_T^2 \rangle = \langle p_\perp^2 \rangle + z^2 \langle k_\perp^2 \rangle. \tag{4.83}$$

Chapter 5

Correction for acceptance

A measurement is never perfect. The imperfections depend on many factors that affect the measurement differently for different kinematics. These imperfections will be referred to as acceptance effects. This section is dedicated to the method used to correct for those acceptance effects. The first part describes how the data is simulated in order to have information both before and after the reconstruction. The second part describes the method of correction for the acceptance effect with an acceptance table and how this table is produced with simulated data. The following part shows how the acceptance correction method can reproduce the true (simulated) data from the reconstructed (simulated) data. The last part compares the acceptance table method with another, less reliable, correction method.

5.1 Monte Carlo simulation

In order to correct for the acceptance, is it important to know the effect of the spectrometer on the data. The main points are

- the trigger response to the data,
- the efficiency of the detectors,
- the kinematic smearing (bin migration),
- the event reconstruction algorithm.

These acceptance effects can be analyzed and corrected for by the means of Monte Carlo (MC) simulation. The principle is simple and can be summarized in one question: If some event happens with given (true) kinematics, will it be detected and with what kinematics will it be determined by the spectrometer and the reconstruction procedure? The way to know these effects is by generating simulated events and have them pass through a simulation of the spectrometer and process this simulated spectrometer response the same way as real data. The generated events must be as similar as possible to the real data and the appropriate *event generator* must be chosen according to the needs of the analysis.

5.1.1 The LEPTO Generator

The events to be generated are muon-nucleon SIDIS with all the produced charged particles from hadronization. The generator used for this analysis is LEPTO [46], a FORTRAN 77 Monte Carlo program to simulate complete lepton-nucleon scattering events. It is based on leading order (LO) electro-weak cross section. The program can be separated into the following steps:

- Random choice of the inclusive variable, e.g. (x_{Bj}, Q^2) , based on the electro-weak cross section.
- Parton interaction
- Hadronization

Choice of the inclusive variables

LEPTO randomly chooses two inclusive variables based on the inclusive cross section. The cross section is by default taken from the single boson (the photon in our case) quark parton model results (4.48) with the Callan-Gross relation (4.53). A more precise formula, though not used in this work, can be optionally used which includes the mass terms and QCD processes to order α_s . The structure functions are defined with the parton distribution functions (PDFs). There are many choices available. This analysis uses the MRST [52].

Choice of parton interaction

Leading order (LO) and first order (QCDC and PGF) parton interactions shown in figure 2.1 are imposed through the exact matrix elements (ME). Divergence are avoided by cut-off on the ME. Higher orders are treated by parton shower [26].

Hadronization

Once the photon-parton process is chosen, the parton type is determined with the PDFs. The parton then fragments according to the Lund string hadronization model [15] where a color string stretches between the struck quark and the remaining quark system or a part of it. As the string stretches, hadrons are created by the production of quark-antiquark and diquark-antidiquark pairs from the energy in the color field. In the case of interaction with a valence quark, the Lund string is stretched between the struck quark and the remaining diquark. For a sea quark interaction, there are three possibilities LO, PGF and QCDC. In the case of LO, the string is stretched between the struck (sea) quark and the remaining sea antiquark (or vice versa). For PGF, two strings stretches from the created quark and antiquark. Both strings are connected to parts of the remaining (spectator) system. Finally, for QCDC, the string stretches from the struck quark to the remnant via the radiated gluon.

5.1.2 Spectrometer simulation with COMGEANT

Once the hadronized final state particles are produced, they are fed to a simulation of the COMPASS spectrometer. The spectrometer simulation software is named COMGEANT [1] and is based on GEANT3 [3].

5.2 Correction method

To correct for the acceptance of the spectrometer, three acceptance tables are produced: an inclusive acceptance, $A_{incl}(Q_i^2, y_j)$, for the scattered muon and two hadron acceptances, $A_{h^{(+,-)}}(p_{Tk}, \eta_0)$, for the produced positive and negative hadrons. The two-dimensional inclusive $(\mu \to \mu'...)$ table contains finite bins in Q^2 and y. In the intervals $\delta Q_i^2 \equiv [Q_i^2 - \frac{\delta Q_i^2}{2}, Q_i^2 + \frac{\delta Q_i^2}{2}]$ and $\delta y_j \equiv [y_j - \frac{\delta y_j}{2}, y_j + \frac{\delta y_j}{2}]$ it is determined in the following way:

$$A_{incl}(Q_i^2, y_j) = \frac{\int_{\delta Q_i^2} \int_{\delta y_j} \frac{d^2 N_{rec}(Q_{rec}^2, y_{rec})}{dQ^2 dy} dQ^2 dy}{\int_{\delta Q_i^2} \int_{\delta y_j} \frac{d^2 N_{gen}(Q_{gen}^2, y_{gen})}{dQ^2 dy} dQ^2 dy} \equiv \frac{\delta N_{rec}^{ij}}{\delta N_{gen}^{ij}},$$
(5.1)

where $\frac{d^2 N_{rec(gen)}(Q^2, y)}{dQ^2 dy} dQ^2 dy$ is the number of reconstructed (generated) events in the intervals $[Q^2, Q^2 + dQ^2]$ and [y, y + dy].

The hadron acceptance is computed separately for positive and negative hadrons in a similar way, but as function of the transverse momentum and pseudorapidity in the laboratory system, $^{lab}p_T$ and $^{lab}\eta$. For simplicity, the *lab* label will be omitted in the following definitions.

The hadron acceptance is conditional, calculated on top of the inclusive (muon) acceptance: only events passing the inclusive selection are used to determine the hadron acceptance tables. This assumes that the acceptance effect for muon detection and hadron detection are largely independent. The hadron acceptance in a bin at $\delta p_{Tk} \equiv [p_{Tk} - \frac{\delta p_{Tk}}{2}, p_{Tk} + \frac{\delta p_{Tk}}{2}]$ and $[\delta \eta_l \equiv \eta_l - \frac{\delta \eta_l}{2}, \eta_l + \frac{\delta \eta_l}{2}]$ is determined in the following way:

$$A_h(p_{Tk},\eta_l) = \frac{\int_{\delta p_{Tk}} \int_{\delta \eta_l} \frac{d^2 n_{rec}(p_T,\eta)}{dp_T d\eta} dp_T d\eta}{\int_{\delta p_{Tk}} \int_{\delta \eta_l} \frac{d^2 n_{gen}(p_T,\eta)}{dp_T d\eta} dp_T d\eta} \equiv \frac{\delta n_{rec}^{kl}}{\delta n_{gen}^{kl}}$$
(5.2)

where the rec and gen label on kinematic variables have been omitted in the middle term for clarity, but are similar to those in the definition (5.1).

To correct for the acceptance, two correction factors are applied, one inclusive, $A_{incl}(Q^2, y)$, and one hadronic, $A_h(p_T, \eta)$. The value of each factor is taken from the acceptance tables. The total acceptance factor is then,

$$A(Q^{2}, y, p_{T}, \eta) = A_{incl}(Q^{2}, y) \cdot A_{h}(p_{T}, \eta).$$
(5.3)

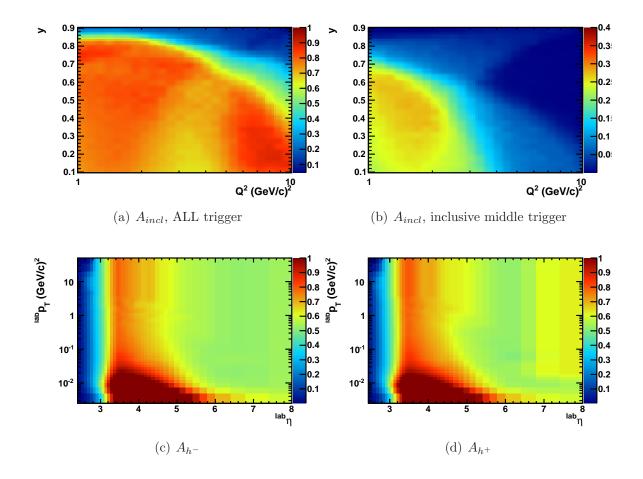


Figure 5.1: Acceptance tables determined with the Monte Carlo samples using formulae (5.1) and (5.2). The tables have been smoothed in order to reduce the granularity from the binning.

Application of this factor, together with the integrated luminosity, to an event with any number of observed hadrons allows to extract the "semi-inclusive" differential cross section of hadron production for DIS muon scattering, as a function of the variables Q^2 , y, p_T , η , (or any other variables) is:

$$\frac{d^4\sigma(\mu N \to \mu' h...)}{dQ^2 dy dp_T d\eta}.$$
(5.4)

For example, in the kinematic display interval¹ $\Delta_{ijkl} \equiv (\Delta Q_i^2, \Delta W_j^2, \Delta p_{Tk}, \Delta \eta_l)$, the num-

¹ This interval should not be confused with a bin δ_{ijkl} of the acceptance tables. It is rather an interval that will later be determined for physics analysis, for example $1 < Q^2 < 1.5$ (GeV/c)², $90 < W^2 < 150$ GeV², $3.5 < \eta < 3.75$ and $0.3 < p_T < 0.4$ GeV/c. The bins for the tables are rather smaller as can be seen in figure 5.1. Also, the variables do not have to be the same as the ones from the table, as shown by the choice W^2 instead of y for this example.

ber of hadrons detected (i.e. not corrected for acceptance) is:

$$\Delta n_{meas}^{ijkl} \equiv \int_{\Delta_{ijkl}} \frac{d^4 n_{meas}(Q^2, W^2, \dots)}{dQ^2 dW^2 dp_T d\eta} dQ^2 dW^2 dp_T d\eta.$$
(5.5)

When corrected for the acceptance, it will be (again omitting the *lab* label):

$$\Delta n_{cor}^{ijkl} \equiv \int_{\Delta_{ijkl}} \frac{\frac{d^4 n_{meas}(Q^2, W^2, \dots)}{dQ^2 dW^2 dp_T d\eta}}{A(Q^2, y, p_T, \eta)} dQ^2 dW^2 dp_T d\eta, = \sum_{\delta} \frac{\delta n_{meas}(Q_i^2, W_j^2, \dots)}{A(Q_i^2, y_{ij}, p_{Tk}, \eta_l)},$$
(5.6)

where the sum in the last term is over all *delta* within Δ_{ijkl} and y_{ij} is a short notation for $y(Q_i^2, W_j^2, E_{ij})$ i.e. the acceptance table variable y as function of the display variables as can be deduced from the relations given in table 4.1. The same would apply to the other variables if they were not the same as the ones used for the acceptance table.

It is instructive to compare the effect of the acceptance correction (5.6) using the acceptance tables (5.1) and (5.2) with the effect of an average, integral acceptance *directly* calculated for the display interval. The direct acceptance is defined similarly as the table, but for a given interval of any wanted width of any wanted variables, e.g. for Δ_{ijkl}

$$\Delta \bar{A}_{Direct}^{ijkl} = \frac{\int_{\Delta_{ijkl}} \frac{d^4 n_{rec}(Q_i^2, y_j, \dots)}{dQ^2 dy dp_T d\eta} dQ^2 dy dp_T d\eta}{\int_{\Delta_{ijkl}} \frac{d^4 n_{gen}(Q_i^2, y_j, \dots)}{dQ^2 dy dp_T d\eta} dQ^2 dy dp_T d\eta} \equiv \frac{n_{rec}^{ijkl}}{n_{gen}^{ijkl}},\tag{5.7}$$

so the corrected number of hadrons (5.6) would become:

$$\Delta n_{cor}^{\prime,ijkl} \equiv \frac{\int_{\Delta_{ijkl}} \frac{d^4 n_{meas}(Q^2,y,\ldots)}{dQ^2 dy dp_T d\eta} dQ^2 dy dp_T d\eta}{\bar{A}_{Direct}^{ijkl}} \equiv \frac{\Delta n_{meas}^{ijkl}}{\bar{A}_{Direct}^{ijkl}}.$$
(5.8)

Note the difference between the direct correction (5.8), where one average acceptance factor is calculated for the needed interval, and the tabulated correction (5.6), where each event and each hadron received a correction factor according to its kinematics.

With (5.5) and (5.6), the average tabulated correction factor within a given display interval Δ_{ijkl} is defined as

$$\bar{A}_{Tab}^{ijkl} = \frac{\Delta n_{meas}^{ijkl}}{\Delta n_{cor}^{ijkl}}.$$
(5.9)

These two acceptance correction methods, the direct and the tabulated, can be compared by means of the ratio of (5.8) and (5.6):

$$\frac{\Delta n_{cor}^{ijkl}}{\Delta n_{cor}^{\prime,ijkl}} = \frac{\bar{A}_{Direct}^{ijkl}}{\bar{A}_{Tab}^{ijkl}}.$$
(5.10)

Even if the Monte Carlo sample were made with an event generator that describes perfectly the hadron distribution, there could be a difference between the two acceptance factors i.e. $(5.9) \neq (5.7)$. Suppose there are regions where the detector acceptance is zero, but physics and Monte Carlo contain finite numbers of events. If the display interval contains such regions, the corrected number of events will differ for equation (5.6) and (5.8). Therefore, the comparison interval has to be carefully chosen. Indeed, in the integrand of the denominator of equation (5.9), i.e. n_{cor}^{ijkl} as defined by (5.6), there is a division by the acceptance factors from the table. For this equation to make sense, all intervals must be within a non-zero acceptance. This is easy when dealing with the tables variables $(Q^2, y, {}^{lab} p_T, {}^{lab} \eta)$, but it should be used with care with other variables e.g. $(x_{Bj}, p_T, \eta, z, ...)$. None-zero acceptance intervals can be verified in a way that does not depend on the Monte Carlo simulation by simply looking where there are data² as can be seen in figure 7.2.

Alternatively, if the semi-inclusive differential cross section is to be extrapolated into regions of zero detector acceptance, the Monte Carlo simulation has to agree with the true physics cross sections in order to be sure that the acceptance correction leads to the correct result. (But in this case, of an existing realistic Monte Carlo simulation, a further measurement would be unnecessary.)

The semi-inclusive hadron production absolute cross section for a given interval Δ^{ijkl} is determined by dividing (5.6) by the integrated luminosity, \mathcal{L} :

$$\Delta \sigma^{ijkl} = \frac{\Delta n_{cor}^{ijkl}}{\mathcal{L}} = \frac{1}{\mathcal{L}} \int_{\Delta^{ijkl}} \frac{\frac{d^4 n_{meas}(Q^2, y, \dots)}{dQ^2 dy dp_T d\eta}}{A(Q^2, y, p_T, \eta)} dQ^2 dy dp_T d\eta.$$
(5.11)

In this definition, the muon and the hadron production have been combined. There are some benefits of factorizing them such as isolating the hadron production and removing the dependence on the integrated luminosity. Here is a way to rewrite the corrected number of hadrons Δn_{cor}^{ijkl} by separating into inclusive and hadron part:

$$\Delta n_{cor}^{ijkl} \equiv \int_{\Delta_{ijkl}} \frac{\frac{d^4 n_{meas}(Q^2, y, \dots)}{dQ^2 dy dp_T d\eta}}{A(Q^2, y, p_T, \eta)} dQ^2 dy dp_T d\eta$$
(5.12)

$$= \int_{\Delta_{ij}} \frac{d^2 N_{meas}}{A_{incl}(Q^2, y) dQ^2 dy} dQ^2 dy \frac{\int_{\Delta_{ijkl}} \frac{d^4 n_{meas}}{A(Q^2, y, p_T, \eta) dQ^2 dy dp_T d\eta}}{\int_{\Delta_{ii}} \frac{d^2 N_{meas}}{A(Q^2, y, p_T, \eta)} dQ^2 dy}$$
(5.13)

$$=\Delta N_{cor}^{ij} \cdot \Delta D^{ijkl},\tag{5.14}$$

(5.15)

where the multiplicity for a given interval Δ^{ijkl} is defined as

²One should remember that the lack of data is not only a result of the acceptance but also of the available phase-space. The upper ${}^{lab}p_T$ limit shown by the curved line in the data distribution in figure 5.10 is a limit of the available energy by the hadron which cannot exceed that of the virtual photon.

$$\Delta D^{ijkl} = \frac{\int_{\Delta_{ijkl}} \frac{d^4 n_{meas}}{A(Q^2, y, p_T, \eta) dQ^2 dy dp_T d\eta} dQ^2 dy dp_T d\eta}{\int_{\Delta_{ij}} \frac{d^2 N_{meas}}{A(Q^2, y, p_T, \eta)} dQ^2 dy} = \frac{\Delta n^{ijkl}_{cor}}{\Delta N^{ij}_{cor}},$$
(5.16)

where the corrected number of muons for a given interval Δ^{ijkl} was introduced:

$$\Delta N_{cor}^{ij} \equiv \int_{\Delta_{ij}} \frac{\frac{d^2 N_{meas}(Q^2, y)}{dQ^2 dy}}{A_{incl}(Q^2, y)} dQ^2 dy, \qquad (5.17)$$

where the inclusive interval $\Delta^{ij} \equiv (\Delta Q_i^2, \Delta y_j)$ and N_{meas} refers to the measured number of events not to be confused with n_{meas} , the measured number of hadrons. Dividing ΔN_{cor}^{ij} by the integrated luminosity gives the inclusive cross section for the inclusive interval Δ^{ij} :

$$\Delta \sigma_{incl}^{ij} \equiv \frac{\Delta N_{cor}^{ij}}{\mathcal{L}}.$$
(5.18)

Now, from (5.15) and (5.18), the absolute semi-inclusive cross section can be rewritten as

$$\Delta \sigma^{ijkl} = \frac{1}{\mathcal{L}} \Delta N^{ij}_{cor} \cdot \Delta D^{ijkl} = \Delta \sigma^{ij}_{incl} \cdot \Delta D^{ijkl}.$$
(5.19)

The inclusive cross section σ_{incl} has been factored out of the hadron production cross section, $\sigma^{\mu \to \mu' h + X}$. The inclusive cross section is well known and has been thoroughly studied (see [18], [19], [6] and reference therein). This allows the determination of $\sigma^{\mu \to \mu' h + X}$ using inclusive cross section taken from published values. This formulation does not depends on the luminosity, which can be practical when it is not determined. Then, the hadron production will be studied with the multiplicity D^{ijkl} . The absolute hadron production cross section will be determine by including σ_{incl} to the multiplicity as in equation (5.19).

Figure 5.1 shows the acceptance tables used in the analysis. The acceptance correction table method assumes that the acceptance does only depends on two inclusive variables and two hadron variables³. Since the acceptance depends on the spectrometer characteristics, the choice of laboratory variables seems natural, so the transverse momentum with respect to the incoming muon, $^{lab}p_T$, and the polar angle, $^{lab}\theta$, are used. The choice of $^{lab}\theta$ is particularly convenient to take care of the acceptance cut due to the SMC magnet at $^{lab}\theta = 0.07$ rad. Actually, pseudorapidity, $^{lab}\eta$, which is directly related to the angle $(\eta = -ln(tan\frac{\theta}{2}))$ is used.

5.3 Reproduction of the simulated distribution

The first thing to verify is if this method can reproduce the generated distribution out of the reconstructed data from these generated events. It works very well for the inclusive

 $^{^3\}mathrm{Actually}$ it should be three, but rotational invariance around the beam axis (the azimuthal angle) is assumed.

variables as can be seen in figure 5.2 and 5.3 for all trigger data and figures 5.4 and 5.5 for inclusive middle trigger data. The verification is also excellent for the x_{Bj} intervals used for the F_2 analysis (cf. table 6.2) as shown in figure 5.6 and 5.7. This is an ideal case of course, because the generated distribution is exactly the same as the one used to create the acceptance correction.

Within acceptance limits

In the case of hadron p_T distribution, figure 5.8 shows that it works very well for z > 0.2. At lower z, a significant amount of hadrons is generated outside the spectrometer acceptance ($\theta < 0.07 \text{ rad}$) and cannot be corrected by the tables as explained in section 5.2. The number of such events increases as z decreases. The acceptance correction method works well for kinematics within the safe region (z > 0.2 and a safe p_T interval determined by the other kinematics).

All hadrons

Now that it is shown that the acceptance correction method works well within the safe acceptance limits, the same verification is done on intervals that will be used for the following analysis. Since the finale results should not be functions of laboratory variables $\binom{lab}{p_T}$, $^{lab}\eta$, it must be verified that the binning as function of physics variables (z, p_T^2) can still reproduce the generated acceptance reasonably. As shown in figure 5.9, the agreement is better than 5% for the comparison of all hadrons from all inclusive bins. The disagreement can be explained by the z > 0.2 limit which is too loose for some inclusive bin to select data away from the angular acceptance limit. As can be seen in figure 5.10, some bins have most of their data around the limit.

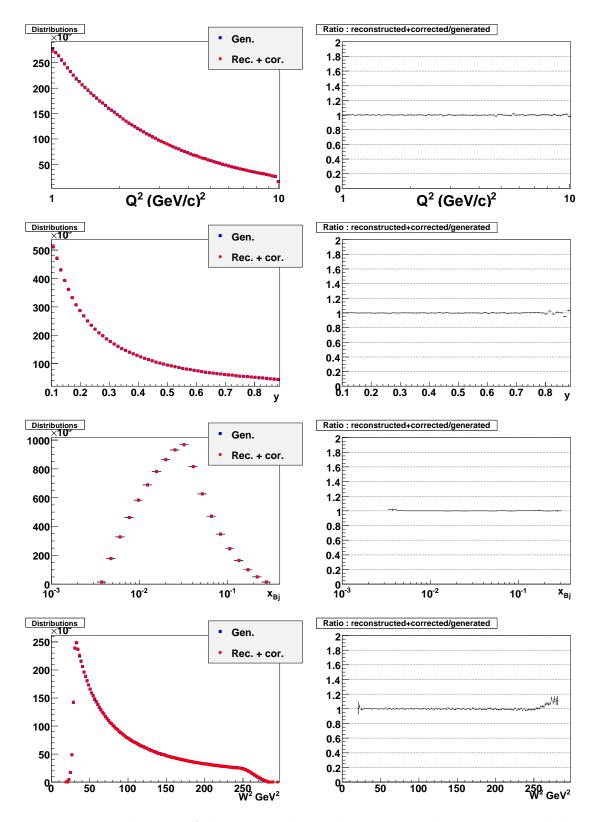


Figure 5.2: Reproduction of the generated distributions with the reconstructed data corrected for the acceptance. Left : distribution of generated and reconstructed (corrected for acceptance). Right : ratio reconstructed(and corrected)/generated. ALL trigger.

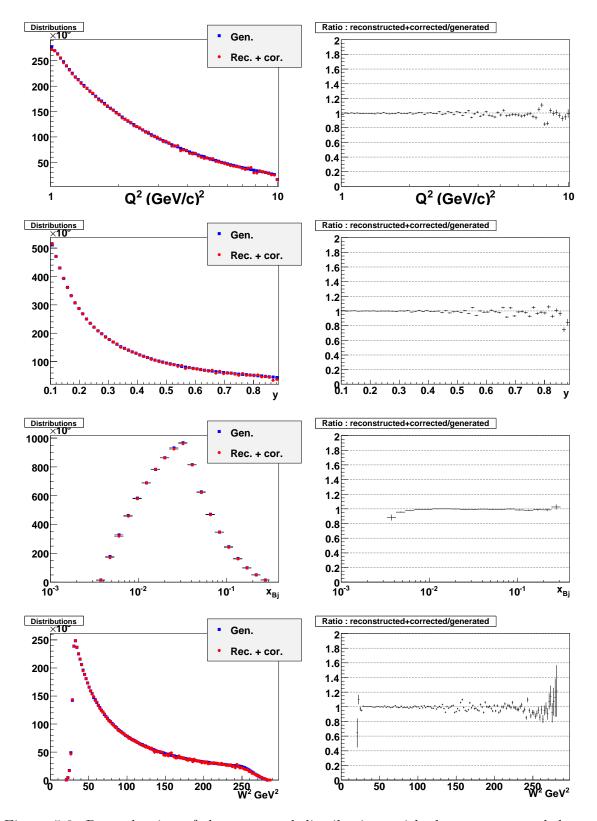


Figure 5.3: Reproduction of the generated distributions with the reconstructed data corrected for the acceptance. Left : distribution of generated and reconstructed (corrected for acceptance). Right : ratio reconstructed(and corrected)/generated. Inclusive middle trigger.

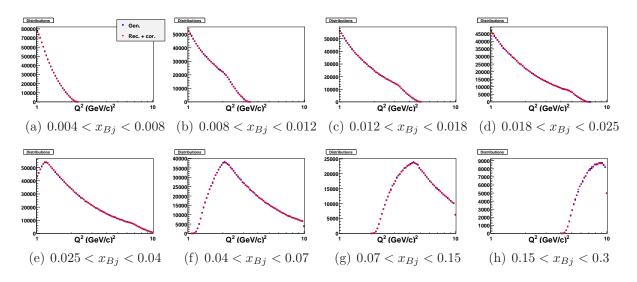


Figure 5.4: Reproduction of the generated distributions with the reconstructed data corrected for the acceptance for the F_2 analysis bins from table 6.2. ALL trigger.

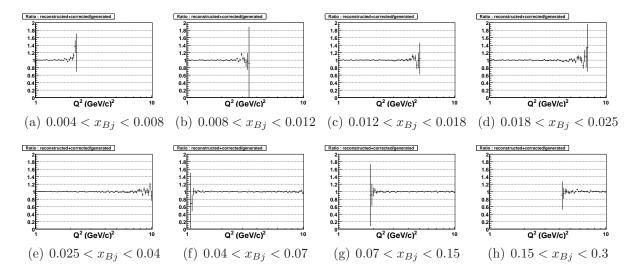


Figure 5.5: Ratio reconstructed (and corrected)/generated for the F_2 analysis bins from table 6.2. ALL trigger.

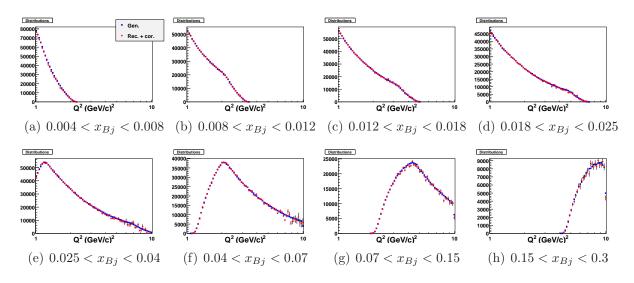


Figure 5.6: Reproduction of the generated distributions with the reconstructed data corrected for the acceptance for the F_2 analysis bins from table 6.2. Inclusive middle trigger.

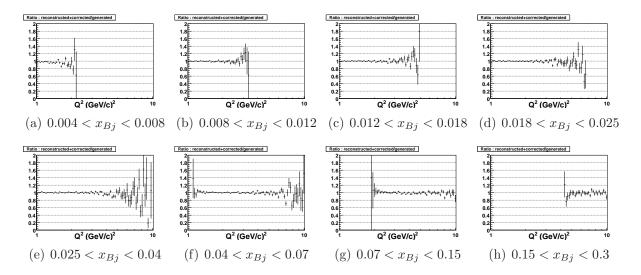


Figure 5.7: Ratio reconstructed (and corrected)/generated for the F_2 analysis bins from table 6.2. Inclusive middle trigger.

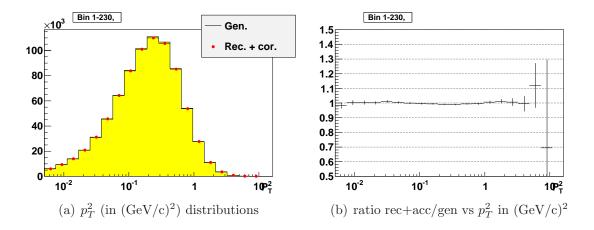


Figure 5.8: Simulated + acceptance corrected compared to generated distributions for z > 0.2 as function of p_T^2 within acceptance limits (see text).

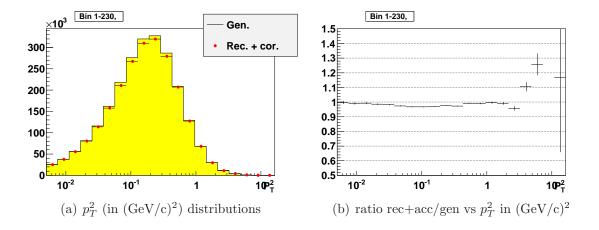
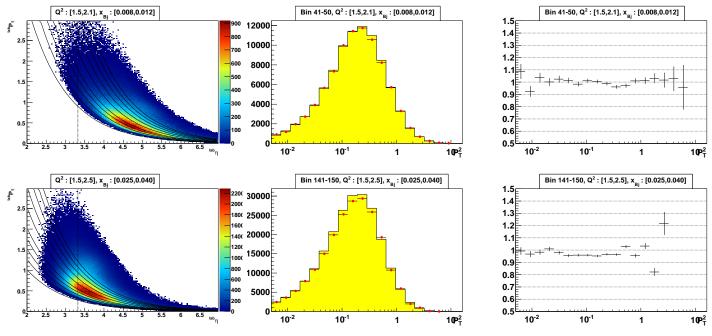


Figure 5.9: Simulated + acceptance corrected compared to generated distributions for z > 0.2 as function of p_T^2 for all hadrons (see text).



(a) Hadron distributions as function of (b) Generated (filled histogram) and re- (c) Ratio of reconstructed (corrected) and constructed (corrected) p_T^2 (in $(\text{GeV/c})^2$) generated vs p_T^2 in $(\text{GeV/c})^2$. distribution comparison.

Figure 5.10: Some bins have their data safely away from the limits as the one on the first row, but some have most of their data close to the limit as in the second row.

5.4 Direct and tabulated acceptance comparison

Now that it was shown that the method can reproduce the generated distributions, the direct and table acceptances from equations (5.9) and (5.7) are compared. See figure 5.11 and 5.14 for ALL trigger and figure 5.12 and 5.16 for inclusive middle trigger data. There are some disagreement, but as explained above, both methods do not have to perfectly agree. Nevertheless, comparing bin by bin in Q^2 and x_{Bj} , as shown in figure 5.14 and 5.16, the agreement is much better. This is in fact because the integrated direct acceptance is not as much integrated since it is in a fixed bin in x_{Bj} and Q^2 , so the two methods are quite similar here.

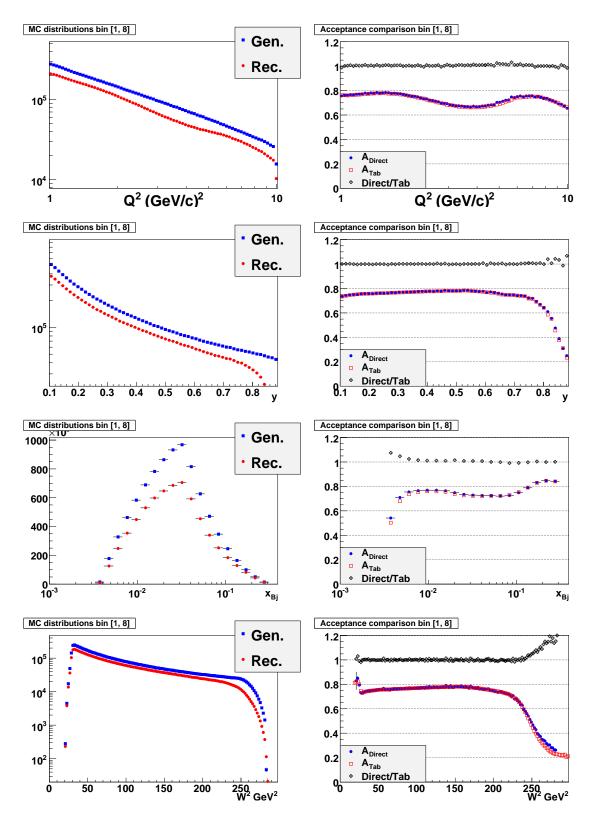


Figure 5.11: Acceptance plots for ALL trigger. Left : MC generated and reconstructed distributions. Right : Acceptances tabulated A_{Tab} and direct A_{Direct} and their ratio $\frac{A_{Direct}}{A_{Tab}}$.

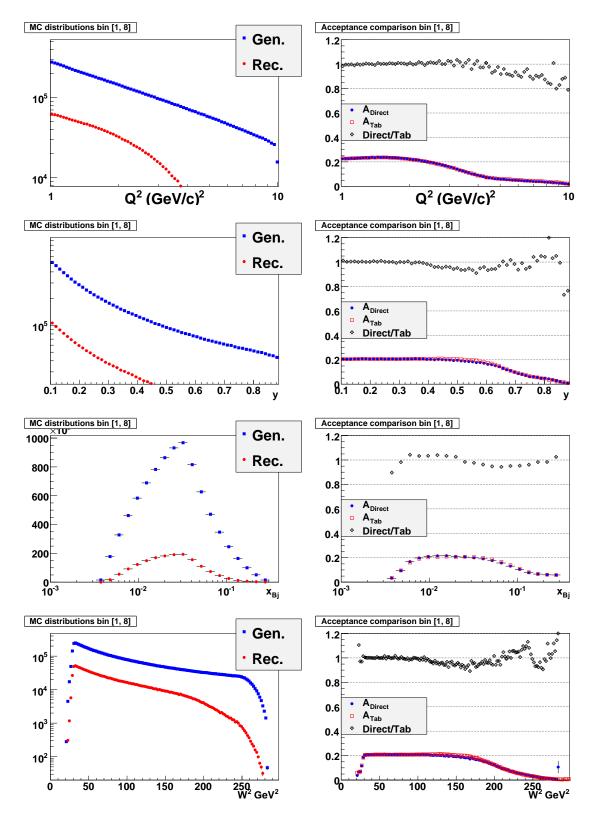


Figure 5.12: Acceptance plots for inclusive middle trigger. Left : MC generated and reconstructed distributions. Right : Acceptances tabulated A_{Tab} and direct A_{Direct} and their ratio $\frac{A_{Direct}}{A_{Tab}}$.

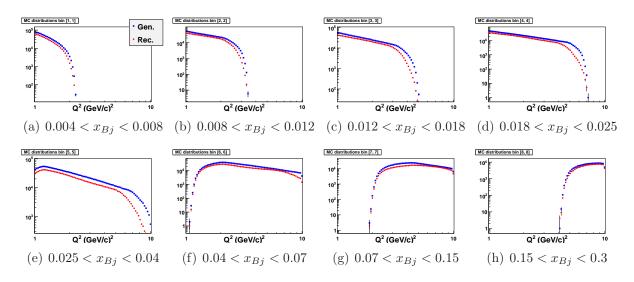


Figure 5.13: Monte Carlo generated and reconstructed distribution plots for ALL trigger in the F_2 analysis bins.

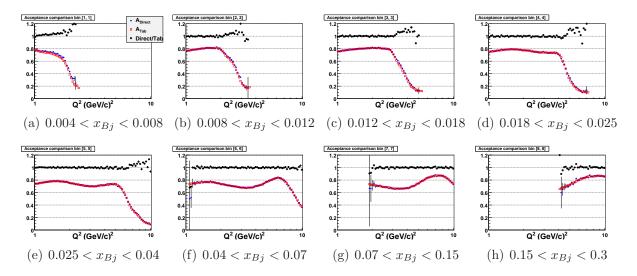


Figure 5.14: Direct and tabulated acceptance comparison for ALL trigger in the F_2 analysis bins.

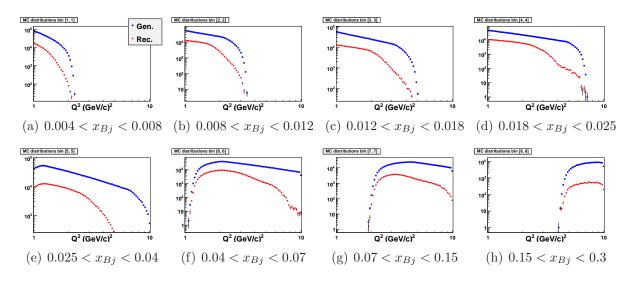


Figure 5.15: Monte Carlo generated and reconstructed distribution plots for inclusive middle trigger in the F_2 analysis bins.

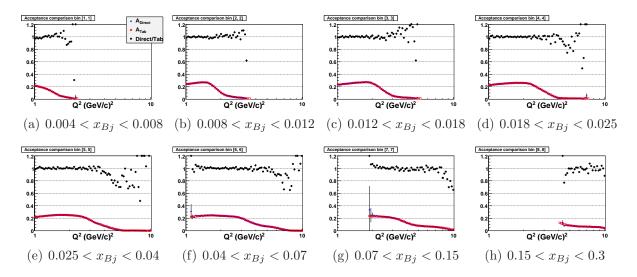


Figure 5.16: Direct and tabulated acceptance comparison for inclusive middle trigger in the F_2 analysis bins.

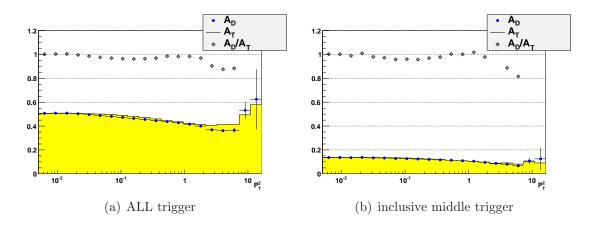


Figure 5.17: Comparison between direct (A_D) and tabulated (A_T) total acceptance as function of p_T^2 (in (GeV/c)²).

Chapter 6

Determination of the inclusive differential cross section

The deep inelastic differential inclusive cross section, $d^2 \sigma^{l+N \to l'+X}/dQ^2 dx_{Bj}$ where only the incoming/scattered lepton is observed has been measured already in the 1960s (see e.g. [62]). The measurement of this cross section allows the extraction of the structure function $F_2(x_{Bj}, Q^2)$ and $F_1(x_{Bj}, Q^2)$ from equation (4.34). The knowledge of those structure functions is increasing as more precise experiments cover larger kinematic domains. The COMPASS kinematic domain has been extensively studied. In the 1990s, the NMC experiment measured the inclusive cross section for the deuteron and used a parametrized fit to describe the F_2 structure function [18]. The following muon-nucleon target experiment at CERN, SMC, used the same parametrized function to fit data from several experiments; BCDMS, E665, NMC and SLAC (see [6] and reference therein).

From the experimental point of view, the cross section is determined by three values:

- \mathcal{L} the integrated luminosity
- A the acceptance correction
- N the number of events

In order to verify that those values were well determined, the structure function F_2 evaluated from COMPASS data is compared with the precise fit from SMC.

6.1 Luminosity

In the case of a fixed target experiment, the luminosity L is defined as the number of target particles (N_T) times the number of incident particles (N_B) per area of the beam/target crossing (\mathcal{A}) per unit time. The area \mathcal{A} must cover the surface of beam-target interaction region i.e. beam that do not cross the target area should be excluded and target regions that are not crossed by the beam should be excluded as well. The integrated luminosity, \mathcal{L} , is simply the luminosity integrated over a given time:

$$\mathcal{L} = \int L dt. \tag{6.1}$$

Target density

In COMPASS, the beam is about the size of the target so the number of target particles can be extracted from the weight of the target material m_T and the nucleon mass m_{nucl} :

$$N_T = \frac{m_T}{m_{nucl}} \tag{6.2}$$

and the area is simply the transverse section of the target πr^2 , where r = 1.5 cm is the radius of the cylindrical target cells. This is assuming that the target is completely filled with its material, ⁶LiD. The area must be corrected for the unfilled part of the target and possible edge effect with the target frame [55]. The area is then limited to r = 1.4 cm and y = 1 cm. The target density is known with a 2% precision.

Beam flux

The number of beam particles are counted for each spill by a scintillating fiber station in front of the target called scaler. But the luminosity is needed only for the beam muons oriented such that their (unscattered) trajectory stays within the limited target volume described above¹. Therefore, the number of beam muons counted by the scaler has to be corrected for the unwanted muons. The correction factor was calculated using a random trigger and counting how many reconstructed muons tracks hitting the counter scintillator hodoscope fulfilled the geometric criteria. The correction factor has been determined to be 0.58 (see [39] and [51]). The counting scintillating fiber station can also have an intrinsic efficiency which would lead to a lower luminosity determination. This effect was roughly estimated to have an upper limit of 10%.

Dead time

As explained in section 3.1.9, the data acquisition has a dead time when an event is recorded. The dead time was 5% for the data taking of 2004. It is to be noted that this value does not include the veto dead time which is included in the Monte Carlo simulation of the spectrometer with the COMGEANT program.

Taking all these effects into consideration, the resulting integrated luminosities for 2004 (longitudinal target spin configuration) are shown in table 6.1.

¹This is not needed for the case of unpolarized cross section, but in the polarized case, the cross section is determined with a difference of interaction in two spin configurations, the target cells. In order to have one luminosity for both polarized and unpolarized cross sections, the unpolarized analysis is done with the same selection.

Period	\mathcal{L}
W22	$93.3{\rm pb}^{-1}$
W23	$55.3\mathrm{pb}^{-1}$
W26	$60.1{\rm pb}^{-1}$
W27	$34.2{\rm pb}^{-1}$
W28	$33.0{\rm pb}^{-1}$
W29	$35.3{\rm pb}^{-1}$
W30	$54.1{\rm pb}^{-1}$
W31	$55.1{\rm pb}^{-1}$
W32	$78.6{ m pb}^{-1}$
W37	$88.5\mathrm{pb}^{-1}$
W38	$101.0{\rm pb}^{-1}$
W39	$53.2{\rm pb}^{-1}$
W40	$33.4\mathrm{pb^{-1}}$
Total	$775.1{\rm pb}^{-1}$

Table 6.1: Integrated luminosity \mathcal{L} excluding bad spills as calculated in [39]. The periods are all of longitudinal target spin configuration from 2004. There is a 2% uncertainty from the number of target particles measurement and 10% uncertainty from the beam counter measurement.

6.2 Data sample

The data for this analysis was taken in the year 2004, all of longitudinal data except period W28 and W29² (i.e. periods W22, W23, W26, W27, W30, W31, W32, W37, W38, W39 and W40) reconstructed with CORAL version 2005-4-12. The integrated luminosity is 706.8 pb^{-1} . Here is a list of the selection criteria:

- The event has at least 2 particles (μ and μ').
- The primary vertex must be inside the fiducial volume of the target (including $Y_{\text{primaryvertex}} < 1 \text{ cm}$).
- The scattered muon must not cross the yoke of SM2 where the magnetic field is not well known.
- The scattered muon must have detector hits after muon wall 2 (MW2).
- The extrapolated muon beam trajectory must cross both target cells.
- The events must be in the kinematic ranges:

$$-Q^2 > 1 \, ({\rm GeV/c})^2$$

$$-0.1 < y < 0.9$$

-140 < E < 180 (GeV/c), E being the energy of the incoming muon.

The selection statistics can be seen in the table 6.3. Distributions will be shown for two different samples, the ALL triggers sample and the inclusive middle trigger sample. As the names suggest, the ALL triggers data includes all events and the inclusive middle trigger is a subsample of data accepted by the inclusive middle trigger defined in section 3.1.8. The inclusive in the name means that the calorimeter was not part of the trigger logic. Plots of the data can be seen in figure 6.1 for ALL triggers, and in figure 6.2 for the inclusive middle trigger. These plots also show the x_{Bj} intervals used to the inclusive analysis listed in table 6.2. There are different Q^2 limits on every x_{Bj} intervals to make sure that the analysis always stays within the acceptance of the spectrometer. It is important to stay only within the kinematics covered by the spectrometer as the limits of the acceptance are influenced by edge effects of the detector which might not be well described by the Monte Carlo simulation. Furthermore, only the cross section measured by the experiment is to be determined, not the simulated one. When there are no data, the only cross section that can be extracted is from the simulation through the correction for acceptance. It was

 $^{^2}$ These two periods are excluded because the inclusive middle trigger was not prescaled (prescaling factor 1) during the data taking. For the other periods, the prescaling factor was set to 2. This means that for period W28 and W29, there were twice more data from the inclusive middle trigger. To be included, these two periods would need a different acceptance correction.

Bin	x_{Bj}	$Q_{\rm ALL}^2 ~[({\rm GeV/c})^2]$	$Q_{\rm InclMT}^2$ [(GeV/c) ²]
1	[0.004, 0.008]	[1, 1.2]	[1, 1.2]
2	[0.008, 0.012]	[1, 2.5]	[1, 2]
3	[0.012, 0.018]	[1, 3.5]	[1, 3.5]
4	[0.018, 0.025]	[1, 5]	[1, 4.5]
5	[0.025, 0.04]	[1.2, 7]	[1.2, 4.3]
6	[0.04, 0.07]	[2, 10]	[2, 6]
7	[0.07, 0.15]	[4.5, 10]	[4.5, 8]
8	[0.15, 0.3]	[8, 10]	[8, 10]

stated earlier that the acceptance correction method is only valid where the acceptance is non zero.

Table 6.2: Intervals for the inclusive analysis. Different Q^2 limits are given for ALL triggers data (Q^2_{ALL}) and the inclusive middle trigger (Q^2_{InclMT}) subsample because they have different acceptance. These intervals are graphically shown with the data in figure 6.1 and 6.2 for ALL triggers and inclusive middle trigger, respectively.

Selection	Number	ratio	red.
$\operatorname{All} \left(Q^2 > 1 (\mathrm{GeV/c})^2 \right)$	124938666	100.00%	0.00%
Event has enough particles	105303524	84.28%	15.72%
Vertex Z inside target	84846168	67.91%	19.43%
Beam momentum	84624246	67.73%	0.26%
SM2 yoke	83622333	66.93%	1.18%
Muon hit after MW2	78010986	62.44%	6.71%
Beam trajectory cross both cells	62744889	50.22%	19.57%
У	45805586	36.66%	27.00%

Table 6.3: Selection statistics for the data sample for all 2004 longitudinal data (except W28 and W29). The column "red." is the relative reduction with respect to the previous line.

6.3 Measured data and Monte Carlo comparison

Before applying the acceptance correction factors, the simulated events are compared with the measured ones. Figure 6.3 compares the Monte Carlo sample with the real data sample as a function of different inclusive variables for ALL triggers data and figure 6.4 for inclusive middle trigger data. In order to be compared with the Monte Carlo sample, the real data sample has been normalized by the factor $\frac{\mathcal{L}_{MC}}{\mathcal{L}_{RD}}$ where \mathcal{L}_{MC} and \mathcal{L}_{RD} are the luminosities

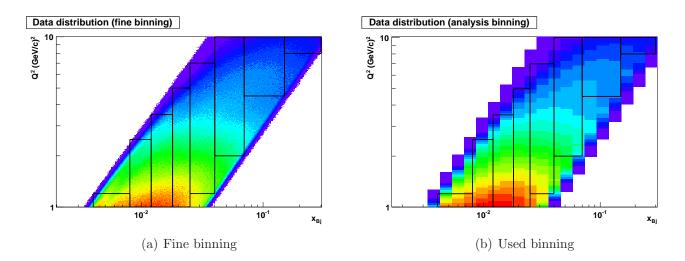


Figure 6.1: Measured data for ALL triggers. a) Fine bins in Q^2 and x_{Bj} to show the detailed structure of the data distribution. b) Bin sizes used for each x_{Bj} and Q^2 distributions. The lines show the (Q^2, x_{Bj}) intervals used for the inclusive analysis listed in table 6.2.

of the generated Monte Carlo sample and the real data sample, respectively. Since only one photon exchange is generated by the Lepto generator, radiative correction factors η have been included to the data to make them correspond also to one photon exchange (see section 6.6). The data from ALL triggers are, on average, 30-40% systematically below those from the Monte Carlo. In the case of the data only from the inclusive middle trigger, the comparison is much closer to unity within about 20%.

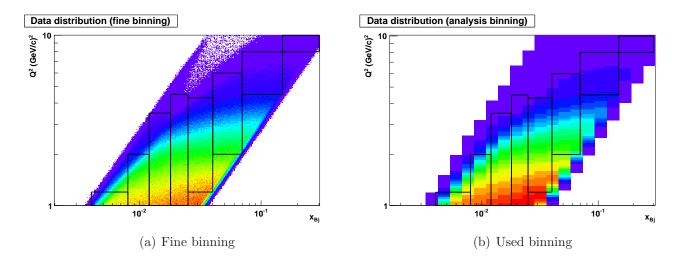


Figure 6.2: Measured data for inclusive middle trigger. a) Fine bins in Q^2 and x_{Bj} to show the detailed structure of the data distribution. b) Bin sizes used for each x_{Bj} and Q^2 distributions. The lines show the (Q^2, x_{Bj}) intervals used for the inclusive analysis listed in table 6.2.

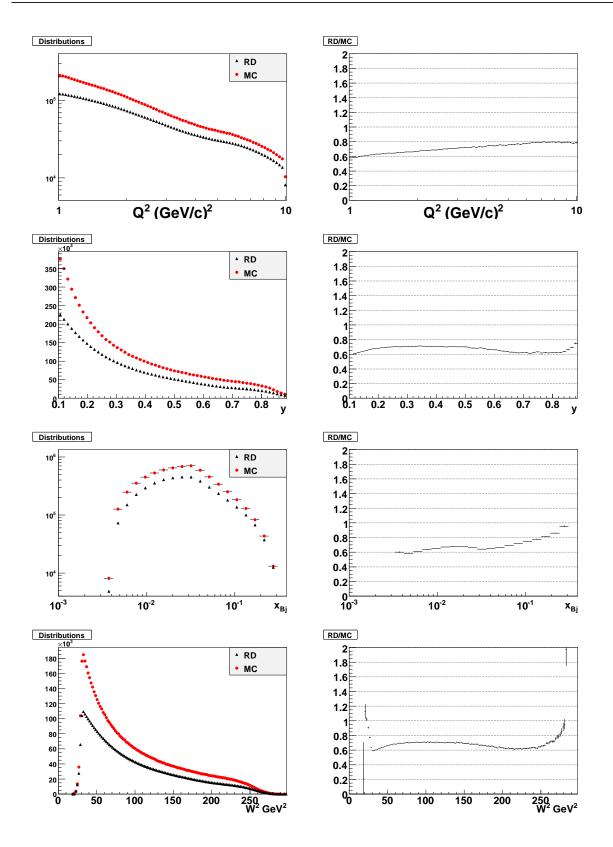


Figure 6.3: Real data vs Monte Carlo for ALL triggers. The real data distribution is normalized by the factor $\frac{\mathcal{L}_{MC}}{\mathcal{L}_{RD}}$ and by the radiative correction factor (see text). LEFT: Distributions. RIGHT: Ratio (Real/Simulated).

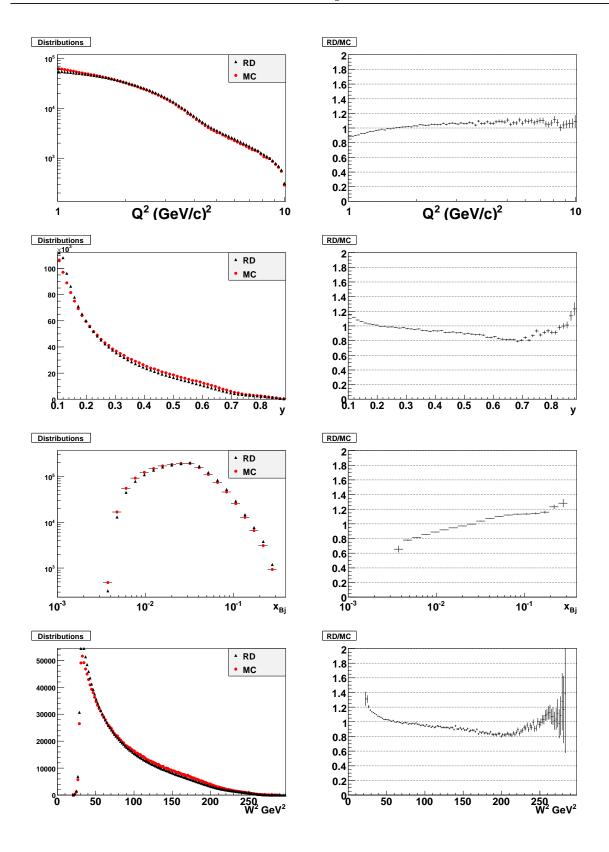


Figure 6.4: Real data vs Monte Carlo for inclusive middle trigger only. The real data distribution is normalized by the factor $\frac{\mathcal{L}_{MC}}{\mathcal{L}_{RD}}$ and by the radiative correction factor (see text). LEFT: Distributions. RIGHT: Ratio (Real/Simulated).

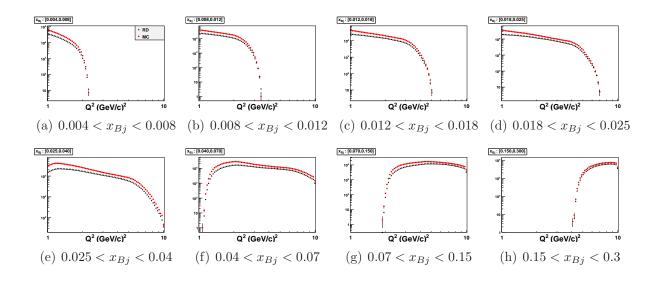


Figure 6.5: Real data vs Monte Carlo for ALL triggers in bins of x_{Bj} defined in table 6.2. The real data distribution is normalized by the factor $\frac{\mathcal{L}_{MC}}{\mathcal{L}_{RD}}$ and by the radiative correction factor (see text).

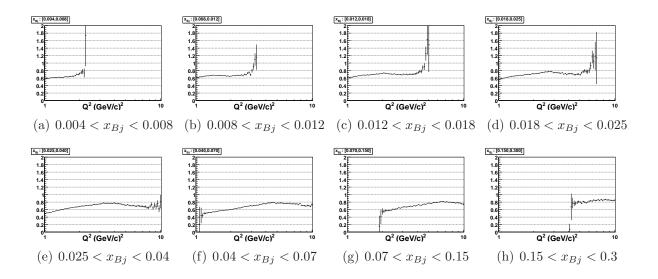


Figure 6.6: Ratio, Real/Simulated, for ALL triggers in bins of x_{Bj} defined in table 6.2. The real data distribution is normalized by the factor $\frac{\mathcal{L}_{MC}}{\mathcal{L}_{RD}}$ and by the radiative correction factor (see text).

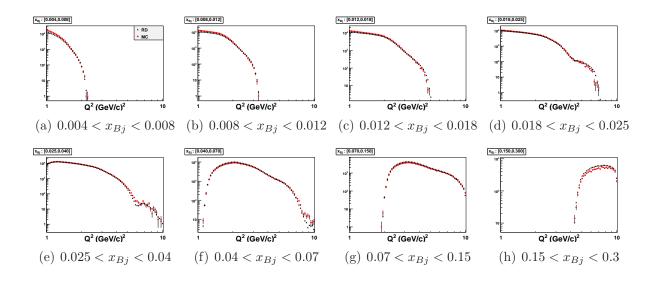


Figure 6.7: Real data vs Monte Carlo for inclusive middle trigger in bins of x_{Bj} defined in table 6.2. The real data distribution is normalized by the factor $\frac{\mathcal{L}_{MC}}{\mathcal{L}_{RD}}$ and by the radiative correction factor (see text).

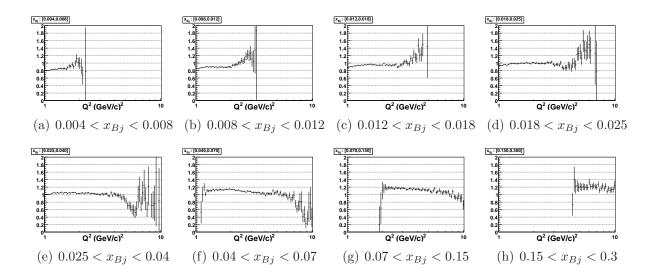


Figure 6.8: Ratio, Real/Simulated, for inclusive middle trigger in bins of x_{Bj} defined in table 6.2. The real data distribution is normalized by the factor $\frac{\mathcal{L}_{MC}}{\mathcal{L}_{RD}}$ and by the radiative correction factor (see text).

6.4 Cross section

All the information is now at hand to investigate how COMPASS data compares with well established data, namely the structure function F_2 from the inclusive cross section. COMPASS inclusive differential cross section in the interval Δ_{ij} is obtained by dividing the measured number of events corrected for acceptance, equation (5.17), by the integrated luminosity \mathcal{L} :

$$\Delta \sigma^{ij} \to d^2 \sigma^{ij}_{meas} \equiv \int_{\Delta_{ij}} \frac{d^2 \sigma_{incl}}{dQ^2 dx_{Bj}} dQ^2 dx_{Bj} = \frac{1}{\mathcal{L}} \int_{\Delta_{ij}} \frac{\frac{d^2 N_{meas}(Q^2, x_{Bj})}{dQ^2 dx_{Bj}}}{A_{incl}(Q^2, x_{Bj})} dQ^2 dx_{Bj}.$$
(6.3)

where the Δ symbol has been changed to the *d* symbol in order to be coherent with the conventional notation for cross sections. Figure 6.9 shows the differential cross section as function of various inclusive variables and figure 6.11 for different x_{Bj} bins for ALL triggers data. Figure 6.10 and 6.12 are for the inclusive middle trigger data.

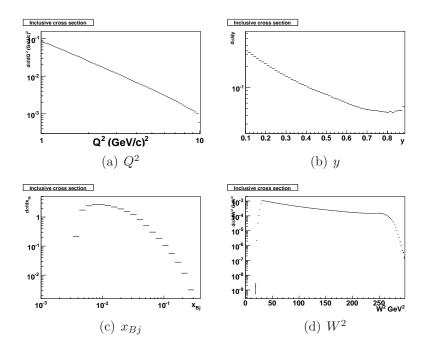


Figure 6.9: Measured and corrected cross sections (in μ b) as function of inclusive variables for ALL triggers.

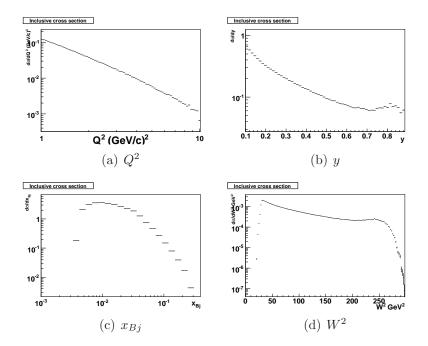


Figure 6.10: Measured and corrected cross sections (in μ b) as function of inclusive variables for inclusive middle trigger.

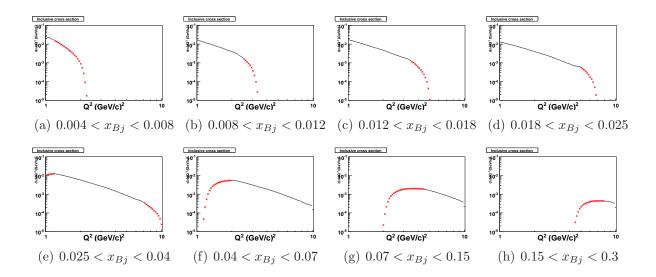


Figure 6.11: Measured and corrected cross sections (in μ b) as function of inclusive variables in the inclusive analysis bins for ALL triggers. The red X marker are points outside the validity bin defined in table 6.2.

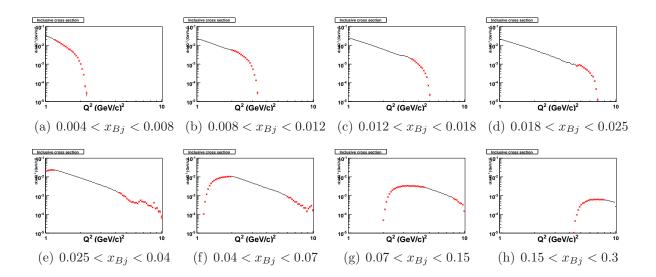


Figure 6.12: Measured and corrected cross sections (in μ b) as function of inclusive variables in the inclusive analysis bins for inclusive middle trigger. The red X marker are points outside the validity bin defined in table 6.2.

6.5 Structure function F_2

From relations (4.41) and (4.42), the general form of the differential cross section for one photon exchange, $\sigma_{1\gamma}$ (4.34), can be written in terms of the nucleon structure function $F_2(x_{Bj}, Q^2)$:

$$\frac{d^2\sigma_{1\gamma}}{dx_{Bj}dQ^2} = \frac{4\pi\alpha^2}{x_{Bj}Q^4} \left(1 - y - \frac{Q^2}{4E^2} + \left(1 - \frac{2m^2}{Q^2}\right)\frac{y^2 + Q^2/E^2}{2(1 + R(x_{Bj}, Q^2))}\right) F_2(x_{Bj}, Q^2), \quad (6.4)$$

where $R = \frac{\sigma_L}{\sigma_T}$ is the ratio of the virtual photon cross section longitudinally (σ_L) and transversely (σ_T) polarized as defined in (4.39). Neglecting the factors Q^2/E^2 , equation (6.4) can be reduced to:

$$\frac{d^2\sigma_{1\gamma}}{dx_{Bj}dQ^2} = \frac{4\pi\alpha^2}{x_{Bj}Q^4} \left(1 - y + \frac{(1 - \frac{2m^2}{Q^2})y^2}{2(1 + R(x_{Bj}, Q^2))}\right) F_2(x_{Bj}, Q^2).$$
(6.5)

This relation will be used to extract the structure function from the measured cross section and using R from [5].

6.6 Radiative correction

In order to determine the F_2 structure function from COMPASS data with equation (6.5), the one photon exchange cross section, $\sigma_{1\gamma}$, must be extracted from the measured cross section (6.3). As explained in section 4.1.5, the latter includes contributions from other electroweak process than the one photon exchange, $\sigma_{1\gamma}$. The other electroweak process cannot be excluded by some data selection. Therefore, the events are weighted with a factor depending on the kinematics, x_{Bj} and y, to correct for processes that are not from $\sigma_{1\gamma}$. This procedure is called radiative correction and is described in [24] and is summarized by the equation (4.44), where σ_{meas} is the measured cross section from eq.(6.3).

The measured cross section σ_{meas} comprise various radiative effects depending on the event selection. Indeed, if a hadron is required by the selection (or trigger), then an elastic event cannot be mistaken for a DIS event because it did not produce a hadron. This is the case for triggers that include calorimeter deposition in their logic. In the case of an event sample without hadron requirement, the factor relating the measured cross section and the single photon exchange will be η . For the measured cross section with a hadron required in the final state, the radiative correction factor will be η_h . In the case of inclusive triggers, only the scattered muon is observed, hence an elastic event can be mistaken for a DIS event. In the data sample from the inclusive middle trigger, the events were triggered by the observed muon only. Hence, to convert σ_{meas} into $\sigma_{1\gamma}$ for the inclusive middle trigger sample, the factor η must be applied. The ALL trigger sample is a mix of triggers and some of them have the calorimeter included in the logic, requiring hadron(s) in the final state. Hence, to convert σ_{meas} into $\sigma_{1\gamma}$ for the ALL trigger sample, a mix of η and η_h should be used. For the rest of this section, only the inclusive middle trigger data will be used because of the straight forward procedure to extract $\sigma_{1\gamma}$ and the structure function F_2 .

The η factors and the extracted single photon exchange cross sections are shown in figures and figures 6.13 and 6.15. These histograms are filled by the average η in a similar way as for the average acceptance factor from equation (5.9). Finally, it is to be noted that this factor is included in the data and Monte Carlo comparison of section 6.3.

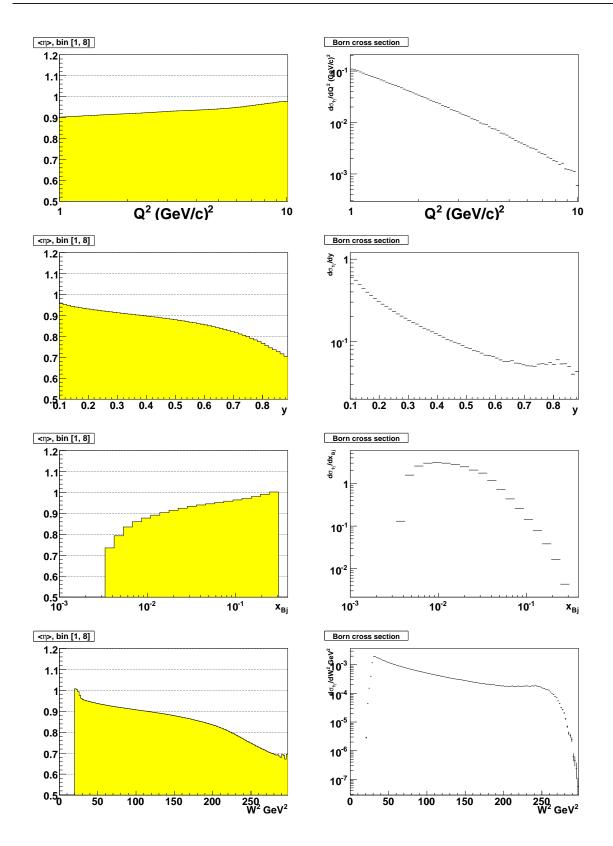


Figure 6.13: LEFT: Average radiative correction factor η for different inclusive variables. RIGHT: Extracted single photon exchange cross section (in μ b) for inclusive middle trigger.

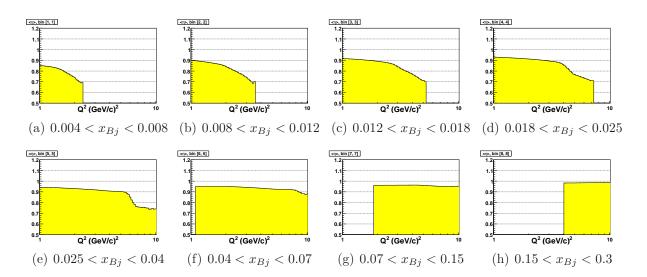


Figure 6.14: Average radiative correction factor η for various x_{Bj} intervals for inclusive middle trigger.

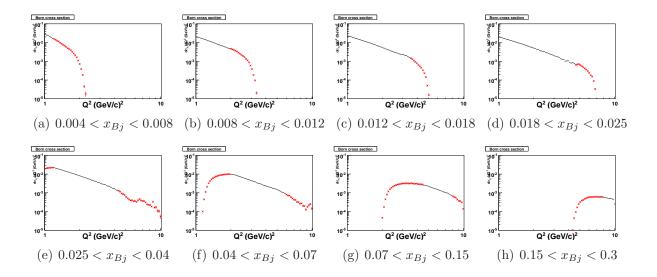


Figure 6.15: Extracted single photon exchange cross section (in μ b) for various x_{Bj} intervals for inclusive middle trigger. The red X marker are points outside the validity bin defined in table 6.2.

6.7 F_2 comparison with SMC

The most most recent determination of the structure function F_2 for the deuteron within COMPASS kinematic range was done by the Spin Muon Collaboration (SMC) [6]. They have parametrized the structure function using the following 15-parameters function:

$$F_2(x_{Bj}, Q^2) = A(x_{Bj}) \left(\frac{\ln(Q^2/\Lambda^2)}{Q_0^2/\Lambda^2}\right)^{B(x_{Bj})} \left(1 + \frac{C(x_{Bj})}{Q^2}\right),\tag{6.6}$$

with $Q_0^2 = 20 \,(\text{GeV/c})^2$, $\Lambda = 0.250 \,\text{GeV/c}$ and the functions A,B,C explicitly given in [18].

Since the parametrization is done on the structure function F_2 and not on the cross section, the SMC fit is compared with F_2 from COMPASS. The latter is calculated with the cross section evaluated with the data as in (6.3). Combining (6.5) and (4.44), it becomes:

$$F_2^{\text{COMP}}(x_{Bj}, Q^2) = \frac{x_{Bj}Q^4}{4\pi\alpha^2} \frac{\eta(x_{Bj}, Q^2)}{1 - y + \frac{(1 - \frac{2m^2}{Q^2})y^2}{2(1 + R(x_{Bj}, Q^2))}} \frac{d^2\sigma}{dx_{Bj}dQ^2},$$
(6.7)

which is shown as function of Q^2 in figure 6.16. Figure 6.17 contains the ratio of the structure functions F_2 from COMPASS (F_2^{COMP}) and the SMC fit (F_2^{SMC}). The analysis has also been performed period-by-period in appendix A.

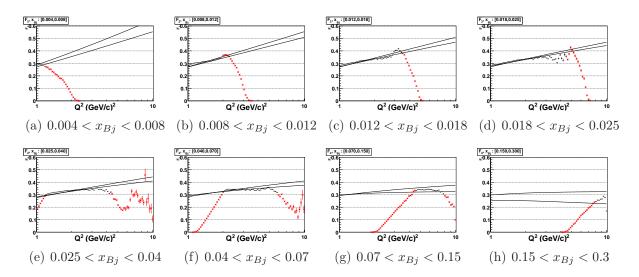


Figure 6.16: Structure function comparison for inclusive middle trigger. The red X marker are points outside the validity bin defined in table 6.2. F_2^{COMP} (points) and F_2^{SMC} (curve). The two curves represent SMC fit for the upper and lower edge of the x_{Bj} bin.

For inclusive middle trigger data, COMPASS F_2 is in excellent agreement within most of the validity ranges defined in table 6.2. The confidence to the inclusive middle trigger data is strengthened by the absolute agreement with the Monte Carlo data (normalized by

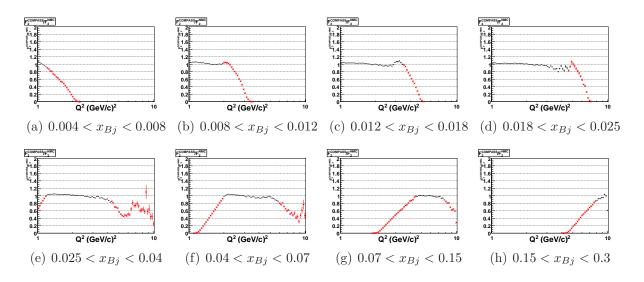


Figure 6.17: $\frac{F_2^{\text{COMP}}}{F_2^{\text{SMC}}}$ for different x_{Bj} bins for inclusive middle trigger. The red X marker are points outside the validity bin defined in table 6.2.

luminosity) which is closer to unity than the comparison for ALL trigger, a similar behavior to the F_2 comparison. This analysis thus suggest that the luminosity determined in [39] is the appropriate one. The same conclusions can be drawn looking at the F_2 comparison plots period-by-period in section A except for period W23 where COMPASS is almost always 20% below SMC.

Chapter 7

Semi-inclusive differential cross section hadron production

The inclusive $\mu + N \rightarrow \mu' + X$ cross section has been compared with published data. The next step is to investigate the rest of the final state particles of deep inelastic scattering. This analysis is restricted to charged hadrons which are mostly pions, about 70% of the selected hadron sample according to previous measurements and to the Monte Carlo simulation. COMPASS has particle identification capability with its RICH detector and calorimeters. A first analysis with charged hadrons is important because it is more reliable. The unidentified charged hadrons detection relies on the straightforward concept of magnetic deflection and absorption through matter. The particle identification is a more complex procedure as it relies on more detectors (RICH, calorimeters). These detectors have their own efficiency and acceptance effects that are convoluted with those already included with the charged hadron detection. For example, the RICH detector can identify pions of energy from 5 GeV to 43 GeV. The Monte Carlo simulation becomes more involved, and the acceptance correction relies on a good description of more parameters. Finally, a first analysis of charged hadrons is also important because many previous experiments published charged hadron distributions.

The following analyses will mostly be concerned about the p_T^2 differential distributions without considering the absolute normalization. The results will be provided in terms of multiplicity defined in (5.16). The absolute differential cross section can then be determined using relation (5.19). The the value for the differential inclusive cross section can be taken from table B.1, where the SMC F_2 has been transformed into the measured cross section taking into account QED radiative effects.

Just as it was done for the case of the inclusive cross section, it is useful to compare published results with COMPASS. Similarly to the inclusive analysis, this section begins with a sample description and measured data vs Monte Carlo comparison. Then, some distributions are compared with the EMC experiment. After these comparisons, the framework described in section 4.2.1 is used to fit the differential cross sections. The fit results are shown for different inclusive variables and compared with results from the HERMES experiment. Finally, a simple model including intrinsic transverse momentum is discussed in the light of these results.

7.1 The data samples

The reduction of the number of hadrons for every selection is shown in table 7.1. As explained above, the hadron identification is kept as simple as possible. The particles coming out of the primary vertex are either identified as muon or hadrons. From these hadrons, the selection requires that they create signals in detectors situated upstream and downstream of the magnet SM1. This ensures that the track momentum and charge are well defined by the bending of the magnetic field. The whole selection removes about 3% of the hadrons from the selected events. There is also a further implicit cut on the hadron energy compared to the virtual photon energy through the z intervals used in the analysis. The intervals do not cover hadrons with z lower than 0.2. This ensures that most of the hadrons are within the angular acceptance of the spectrometer and removes the electrons falsely identified as hadrons.

The following analysis of hadron kinematics will be repeated for different intervals of the inclusive variables Q^2 and x_{Bj} shown in figure 7.1. These intervals are similar to those of the inclusive analysis from the previous section, but with a further separation in x_{Bj} . This will allow to see the evolutions of the hadron production cross section as function of different inclusive variables.

Selection	# of hadrons	ratio	red.
Total number of hadrons	8348335	100.00%	0.00%
First hit before SM1	8147036	97.59%	2.41%
Last hit after SM1	7889605	94.51%	3.16%

Table 7.1: Hadron selection statistics for period 04W31. The column "red." is the relative reduction with respect to the previous line. The total number of hadrons only includes those from events that passed the inclusive selection criteria.

7.2 Real data and Monte Carlo comparison

The measured distributions (not corrected for acceptance) and simulated distributions of hadron kinematics are compared to investigate how accurately the simulated sample describes the measured data. The dependence on inclusive variables has been studied previously in section 6 and in [56]. It was shown that the simulation describes the inclusive kinematics well, so only the comparison for hadron variables will be shown in this section.

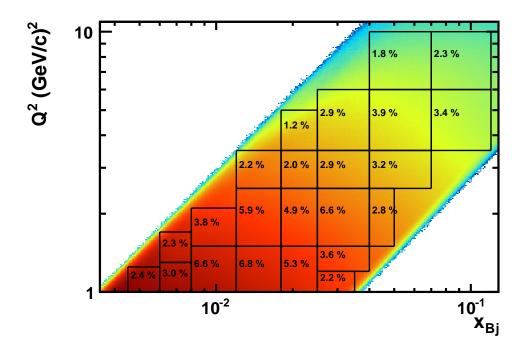


Figure 7.1: Event distribution in Q^2 (in $(\text{GeV/c})^2$) and x_{Bj} and the inclusive intervals of the hadron cross section analysis. Within each interval, the fraction of data in percent contained by the interval is indicated.

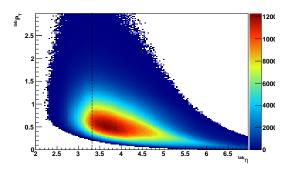


Figure 7.2: Hadron distribution as function of the *laboratory* variables ${}^{lab}p_T$ (in GeV/c) and ${}^{lab}\eta$. The dotted vertical line corresponds to the angular acceptance of 70 mrad.

Figure 7.3 compares the simulated with the real data for ALL triggers data and figures 7.4 for inclusive middle trigger data. In order to have an absolute comparison, the real data sample has been normalized by the factor $\frac{\mathcal{L}_{MC}}{\mathcal{L}_{RD}}$ where \mathcal{L}_{MC} and \mathcal{L}_{RD} are the luminosities of the generated Monte Carlo sample and the real data sample, respectively. The absolute difference between ALL triggers and inclusive middle trigger data was already observed at the inclusive level and it was also shown that the inclusive middle trigger data agrees well with previous experiments as explained in section 6. The disagreement at high z values could indicate radiative (QED) effects or a wrong description of pQCD (gluon radiation) since these effects could be more important at high z.

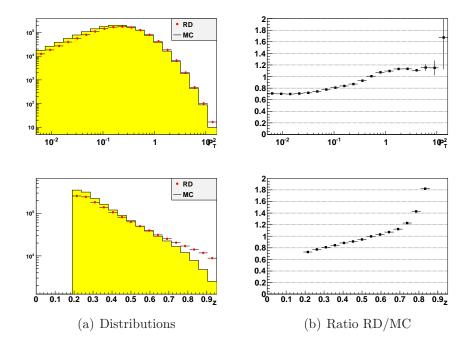


Figure 7.3: Measured data (red points) and Monte Carlo (yellow histogram) comparison for ALL triggers (left column). Ratio of the measured data and simulated data (right column). First row: comparison as function of p_T^2 (in (GeV/c)²). Second row: comparison as function of z. Only hadrons with 0.2 < z < 1 are shown since the hadrons with z < 0.2are excluded from the analysis. See text for more details.

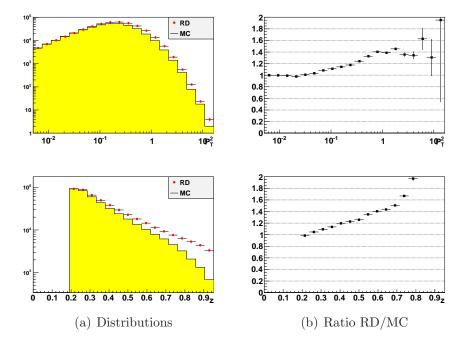


Figure 7.4: Measured data (red points) and Monte Carlo (yellow histogram) comparison for inclusive middle trigger. Ratio of the measured data and simulated data (right column). First row: comparison as function of p_T^2 (in (GeV/c)²). Second row: comparison as function of z. Only hadrons with 0.2 < z < 1 are shown since the hadrons with z < 0.2 are excluded from the analysis. See text for more details.

7.3 Comparison with EMC

Before studying the hadron production cross section in more details, some results can already be compared with other experiments. The previous experiment EMC published charged hadron p_T distributions in [21]. In order to reproduce their selection, the following two cuts have been modified:

- 0.2 < y < 0.8
- $2 < Q^2 < 10 \, (\text{GeV/c})^2$

Figure 7.5 shows the comparison of the differential multiplicities corrected for acceptance as defined by (5.16). The fitted function is the same as the one given in [21], $\propto 1/(m^2+p_T^2)^{\alpha}$ which is inspired by a propagator form. The ratio of COMPASS and EMC multiplicities is shown in figure 7.6. The fitted parameters m are in agreement with the quoted range in [21] (0.6-1.6 GeV/c² except for lower W^2). On the other hand, the parameters α are significantly higher (4-10 when for both COMPASS and EMC) whereas they quote the range 1.4-2.6. Nevertheless, this exercise is intended to compare the distributions and the fit is just a visual aid. The absolute agreement is reasonable for the lower invariant mass intervals ($W^2 < 90$ and $90 < W^2 < 150$ GeV²). The shapes also agree for the highest W^2 interval (150 < W^2 < 200 GeV²), but here, COMPASS multiplicity tends to decrease faster than those of EMC with increasing transverse momentum. It is to be noted that EMC mixes data from different beam energy (cf. table 1 from [21]), this might affect the mean W^2 of the interval and the width of the p_T^2 depends on the energy and/or W^2 as explained in [60]. Figure 7.7 shows the charged hadron multiplicity ratio h^+/h^- . The statistical error of the COMPASS data are significantly reduced as compared to EMC. The ratio is interesting because the acceptance is canceled to a good approximation¹.

¹ This is assuming that positive and negative hadrons have the same acceptance, which is a good approximation for COMPASS as can be seen in figure 5.1.

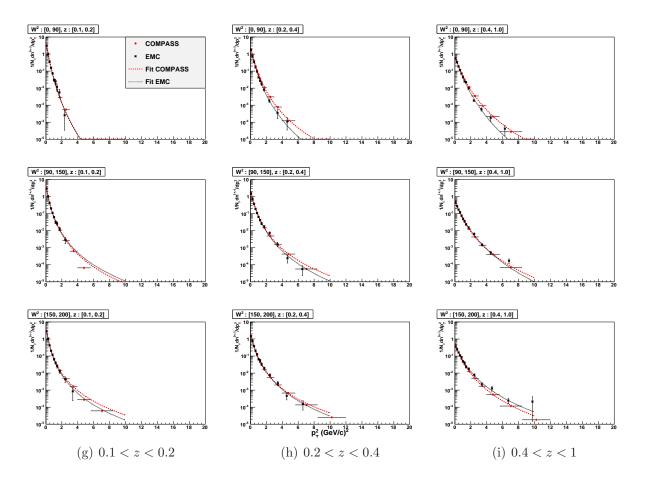


Figure 7.5: Differential multiplicities (corrected for acceptance) as function of p_T^2 in units of $(\text{GeV/c})^2$, $\frac{dn^{+,-}}{N_\mu dp_T^2}$ and fit $\propto 1/(m^2 + p_T^2)^{\alpha}$ (see text), comparison between COMPASS and EMC [21] for different bins of invariant mass W^2 and different z intervals. The red dot and dashed line are COMPASS data and fit, respectively. The black square and small dot line are EMC data and fit, respectively. The columns are, from left to right, the three z interval [0.1,0.2], [0.2,0.4], [0.4,1]. The rows are, from top to bottom, the three W^2 intervals [0,90],[90,150],[150,200] GeV².

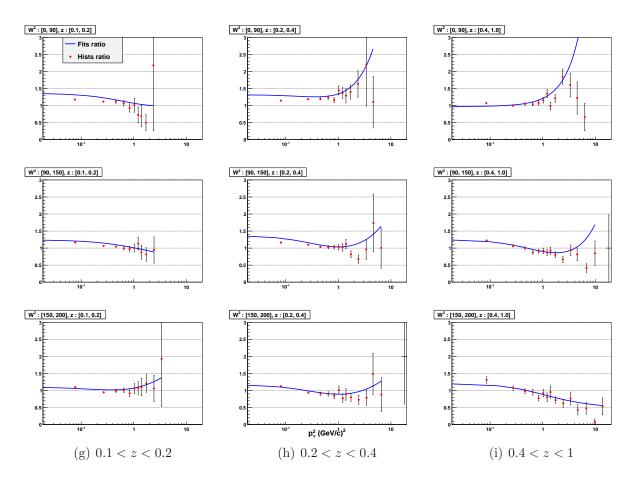


Figure 7.6: Differential multiplicity ratios (COMPASS/EMC) of histograms (red point) and fits (blue line), from figure 7.5, as function of p_T^2 .

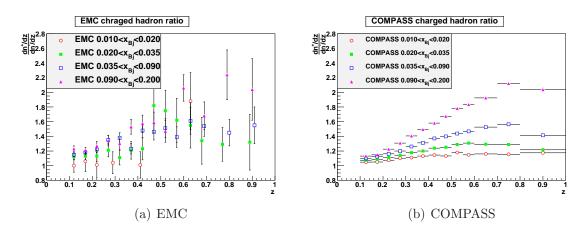


Figure 7.7: Charged hadron differential multiplicity ratios dn^+/dn^- as function of z for EMC and COMPASS.

7.4 Energy dependence of $\langle p_T^2 \rangle$

According to [60], the average intrinsic transverse momentum $\langle k_{\perp}^2 \rangle$ is expected to have a linear dependence on the center of mass energy² s [60]. The relation is:

$$\langle k_{\perp}^2(s) \rangle \approx \langle k_{\perp}^2(0) \rangle + C \cdot s,$$
(7.1)

where $\langle k_{\perp}^2(0) \rangle = 0.3 \ (\text{GeV/c})^2$ and $C = 0.7 \cdot 10^{-3}$. This relation was inferred in the framework of the Gauss ansatz as described in section 4.2.2.

Relation (7.1) is compared with the evolution of the measured hadron transverse momentum $\langle p_T^2 \rangle$ from experiments at different center of mass energies s. To make this relation, the authors of [60] make the assumption that the broadening of the transverse momenta acquired during the fragmentation process, $\langle p_{\perp}^2 \rangle$, also broadens with s at a similar rate (and that it is also Gaussian). In [60], the authors use the average hadron transverse momentum, $\langle p_T \rangle$, measured by COMPASS, *uncorrected for acceptance* taken from [8] and convert it to $\langle p_T^2 \rangle$ with the following relation:

$$\langle p_T(z) \rangle^2 = \frac{\pi}{4} \langle p_T^2(z) \rangle \tag{7.2}$$

valid for the Gaussian ansatz. This value is combined with values from HERMES ($s = 52 \,(\text{GeV/c})^2$) and JLab ($s = 12 \,(\text{GeV/c})^2$) as shown in figures 7.8 assuming that they have a common value of $z \,(0.5 < z < 0.6)$. They observe a reasonable agreement with a linear relation of $\langle p_T^2(z) \rangle$ as function of s. The authors extrapolate HERMES intrinsic momentum with relation (7.1) to COMPASS' center of mass energy. From this extrapolated intrinsic momentum, they determined the averaged transverse momentum of the hadron using relation 4.83. Assuming the transverse momentum acquired from fragmentation, $\langle p_{\perp}^2 \rangle$, independent of s, the resulting "predicted" $\langle p_T^2 \rangle \sim 0.30 \pm 0.03 \,(\text{GeV/c})^2$ for COMPASS is significantly smaller than the one they determined from [8]. The authors concluded that the broadening of the intrinsic transverse momentum is not enough to explain the increase of the hadron transverse momentum but there must also be a similar contribution from the transverse momentum acquired during fragmentation.

A proper acceptance corrected value of the average transverse momentum within the quoted z interval 0.5 < z < 0.6 can now be provided. The resulting p_T^2 distribution of hadrons is shown in figure 7.9. From this distribution, $\langle p_T^2 \rangle$ is determined to be $0.406 \,(\text{GeV/c})^2$. This corrected $\langle p_T^2 \rangle$ is compared to HERMES and JLab measurement and is in a better agreement with the linear s-dependence.

It is mentioned in [60] that the photon-hadron center of mass energy square, W^2 , would be more consistent to use than s in relation (7.1). The W^2 dependence of the mean p_T^2 is

² It should be a linear function of the photon-hadron center of mass energy, but the authors of [60] have made it a linear function of s (lepton-hadron) assuming the deviation from the linearity of s is negligible compared to other uncertainties.

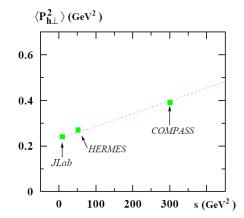


Figure 7.8: Mean p_T^2 in SIDIS for $z \sim 0.5$ as function of lepton-hadron center of mass energy square s from [60]. The COMPASS average p_T^2 was taken from an uncorrected $\langle p_T \rangle$ from [8] and converted to $\langle p_T^2 \rangle$ with relation (7.2) assuming the Gaussian ansatz.

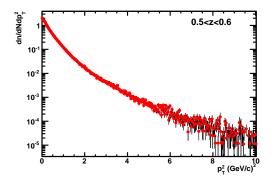


Figure 7.9: Hadron distribution corrected for acceptance from all inclusive bins and 0.5 < z < 0.6. The mean p_T^2 is 0.406 (GeV/c)² for all hadrons 0.5 < z < 0.6 (0.410 for positive and 0.401 for negative hadrons).

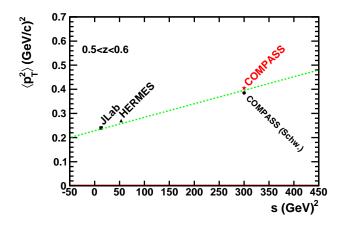


Figure 7.10: Mean p_T^2 vs *s* as shown in figure 7.8 with the the COMPASS estimated value from [60] and the corrected COMPASS value. The dashed line is the authors' fit of the values of their article (i.e. the COMPASS (Schw.) black point is fitted, not the corrected COMPASS red star).

then also proposed here. The results are shown in figure 7.11. The increase as function of W^2 is also observed, but the relation is not linear. There is also an increase of the mean p_T^2 as function of Q^2 . It must be noted that the Q^2 limits in the captions can vary because they are defined by the binning of figure 7.1. For example, the highest W^2 point in figure 7.11(a) comes from the Q^2 limits [1, 1.2] and not [1,1.5]. The average Q^2 have therefore been explicitly indicated for each point in the figures.

7.5 Fit of the cross sections

The differential multiplicity as function of p_T^2 is fitted with a Gaussian function $e^{-p_T^2/\langle p_T^2 \rangle}$ (cf. equation (4.82)) to extract $\langle p_T^2 \rangle$. Multiplicities and fits are shown, for example, in figure 7.12 at different z for different intervals in the inclusive variables Q^2 and x_{Bj} . The model at the origin of the fit does not include pQCD (i.e. gluon radiation is not taken into consideration). Indeed, according to the authors of the paper that provided the framework for this fit, [16], this model fails to describe experimental data for $p_T \gtrsim 1 \text{ GeV/c}$. They could cure the disagreement by including pQCD to their results [16]. This disagreement is also observed in this analysis. Therefore, the fit is performed over a low p_T interval [0.1, 0.85] GeV/c in order to stay away from the domain of pQCD (the lower limit is to stay away from the nuclear coherence effects). The hadron multiplicities determined at the highest z (> 0.8) did not have the Gaussian behavior of equation (4.82) and were excluded from the analysis.

The fitting process was repeated for every (Q^2, x_{Bj}) interval of figure 7.1. The results are

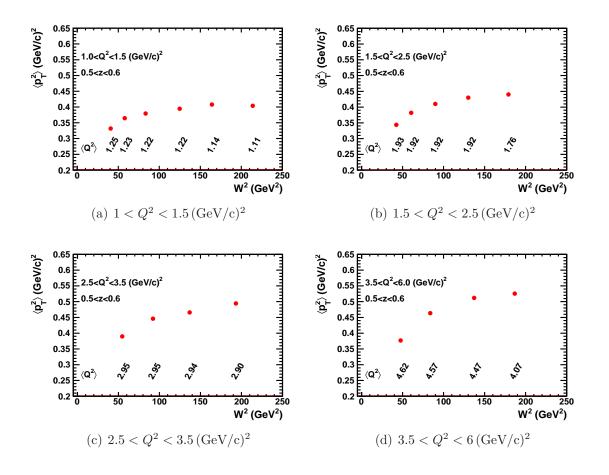


Figure 7.11: Mean p_T^2 as function of W^2 for different Q^2 intervals for 0.5 < z < 0.6. As explained in the text, the last (higher W^2) points of subfigure 7.11(b) and 7.11(d) and the last two points of 7.11(a) have an upper Q^2 limit smaller than the one given in the caption. They should be considered with care or removed since we see a dependence on Q^2 .

presented in figures 7.12, 7.13, 7.14, 7.15, 7.16 and 7.17 and numerically in appendix C. The behavior of $\langle p_T^2 \rangle$ as function of inclusive variable Q^2 for fixed x_{Bj} are shown in figures 7.18 and 7.19. There are two obvious features in these figures: First, the positive hadrons, h^+ , have higher $\langle p_T^2 \rangle$ than the negative hadrons, h^- , at higher z and they coincide at lower z. The second feature is the logarithmic increase of $\langle p_T^2 \rangle$ as function of Q^2 which is clear for higher z and is only marginal in some inclusive intervals at smaller z. According to [22], this Q^2 effect might be a W^2 dependence. Therefore, the same analysis was performed for fixed W^2 . The Q^2 dependence at high z remains as can be seen in figures 7.22 and 7.23.

The behavior of $\langle p_T^2 \rangle$ as function of inclusive variable x_{Bj} for fixed Q^2 is shown in figures 7.20 and 7.21. The $\langle p_T^2 \rangle$ dependence in x_{Bj} is flat for high z data and decreases with x_{Bj} for low z. This behaviors is also observed for $\langle p_T \rangle$ at HERMES in [47]³. Note that in their case, $\langle p_T \rangle$ is not taken from a fit, but by the average p_T . Therefore, the higher p_T are also included. This suggests that their observed dependence on x_{Bj} is not caused by gluon radiations.

Finally, it is interesting to compare the $\langle p_T^2 \rangle$ resulting from the fit and the mean p_T^2 from the previous section. Figure 7.11 shows the means of the full p_T^2 distributions, while figure 7.24 shows the fitted $\langle p_T^2 \rangle$ of the low p_T^2 part of the distributions. The former is a simple average and the latter is the width of a Gaussian fit. The fitted $\langle p_T^2 \rangle$ shown in figure 7.24 do not show a clear dependence on W^2 . Assuming that restricting the fit to low p_T^2 removes all effects of pQCD as explained above, the W^2 -dependence of figure 7.11 could be attributed to gluon radiation.

³ In the Gaussian ansatz, $\langle p_T \rangle$ is related to $\langle p_T^2 \rangle$ by equation (7.2).

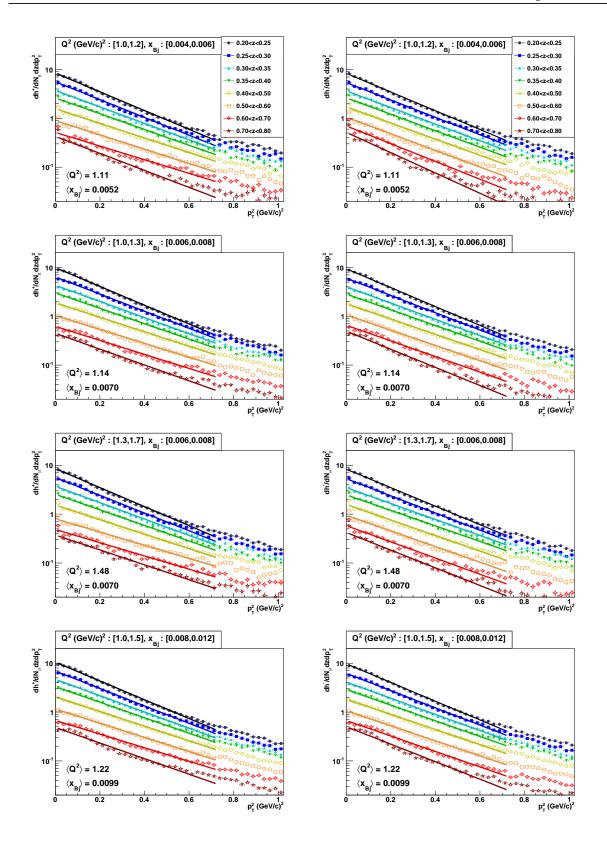


Figure 7.12: h^+ (left) and h^- (right) differential multiplicities and Gaussian fit. The fit result gives $\langle p_T^2 \rangle$ from the relation (4.82). Each row represents a different inclusive interval. Each figure shows the distributions and fits for different z intervals.

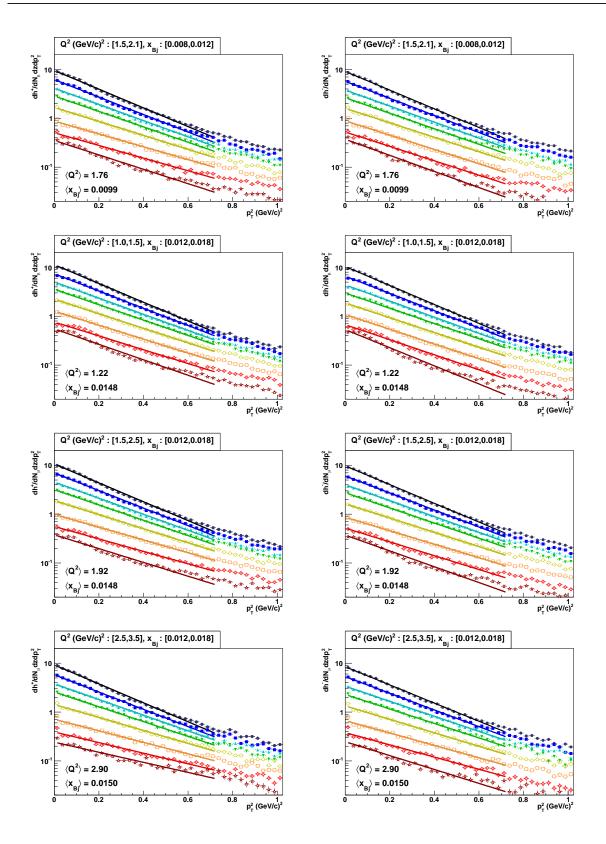


Figure 7.13: h^+ (left) and h^- (right) differential multiplicities and Gaussian fit. The fit result gives $\langle p_T^2 \rangle$ from the relation (4.82). Each row represents a different inclusive interval. Each figure shows the distributions and fits for different z intervals.

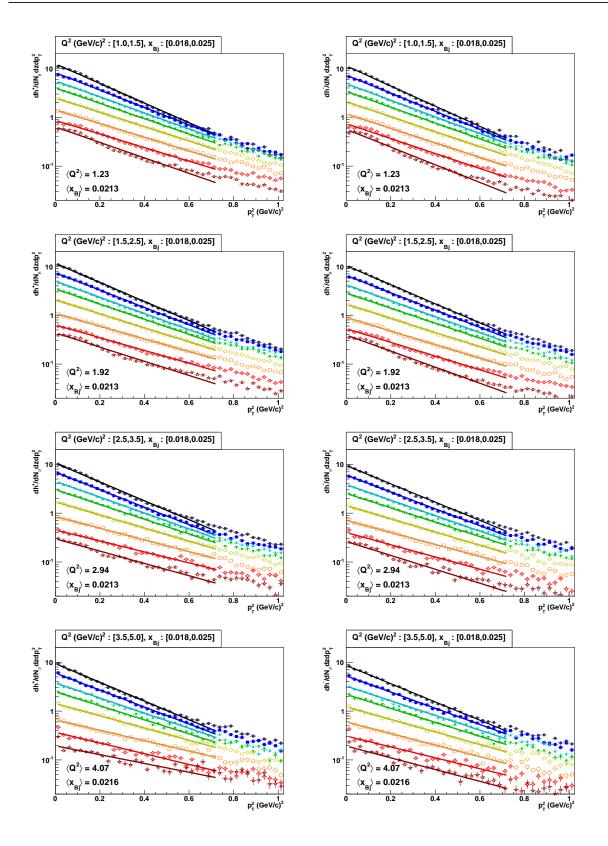


Figure 7.14: h^+ (left) and h^- (right) differential multiplicities and Gaussian fit. The fit result gives $\langle p_T^2 \rangle$ from the relation (4.82). Each row represents a different inclusive interval. Each figure shows the distributions and fits for different z intervals.

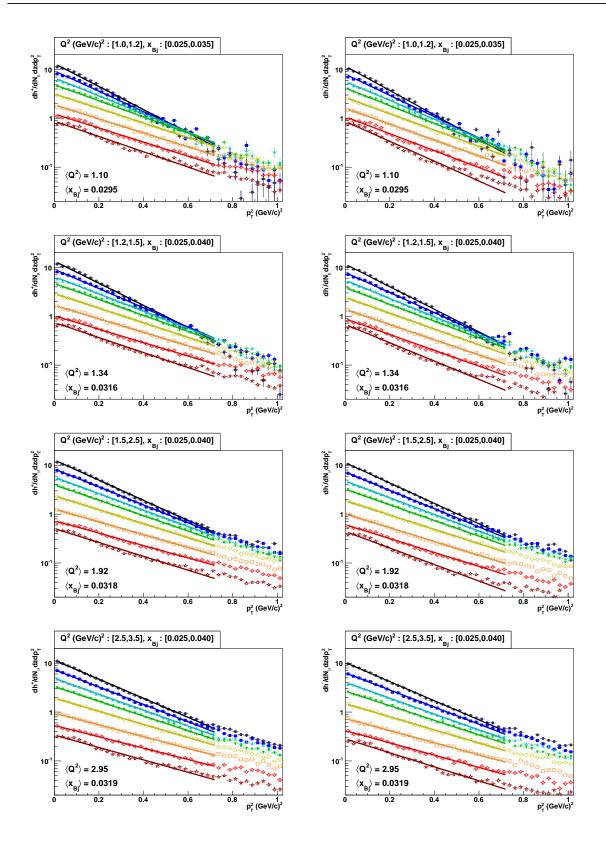


Figure 7.15: h^+ (left) and h^- (right) differential multiplicities and Gaussian fit. The fit result gives $\langle p_T^2 \rangle$ from the relation (4.82). Each row represents a different inclusive interval. Each figure shows the distributions and fits for different z intervals.

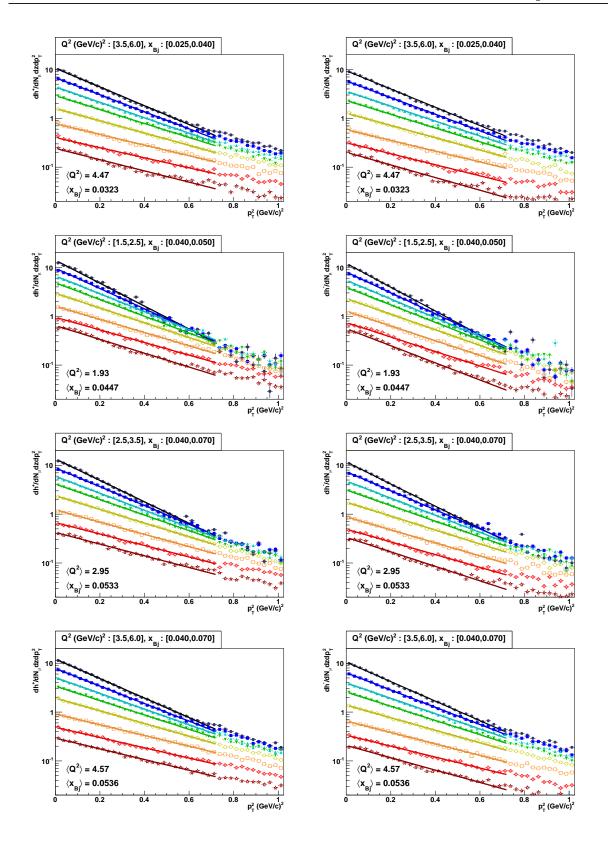


Figure 7.16: h^+ (left) and h^- (right) differential multiplicities and Gaussian fit. The fit result gives $\langle p_T^2 \rangle$ from the relation (4.82). Each row represents a different inclusive interval. Each figure shows the distributions and fits for different z intervals.

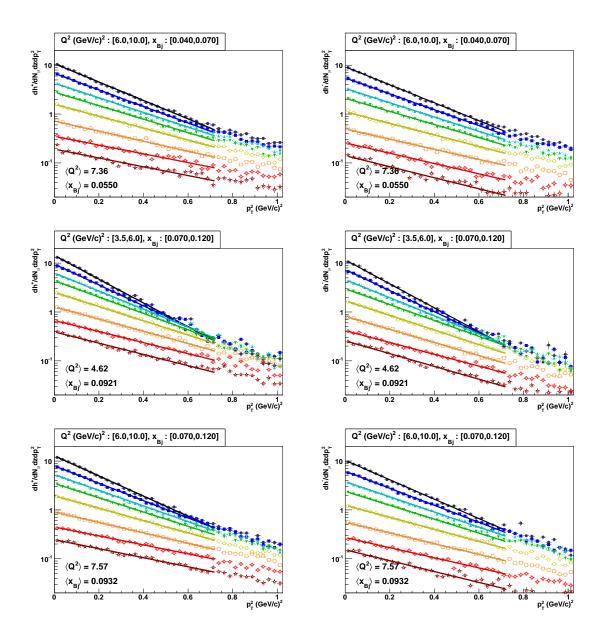


Figure 7.17: h^+ (left) and h^- (right) differential multiplicities and Gaussian fit. The fit result gives $\langle p_T^2 \rangle$ from the relation (4.82). Each row represents a different inclusive interval. Each figure shows the distributions and fits for different z intervals.

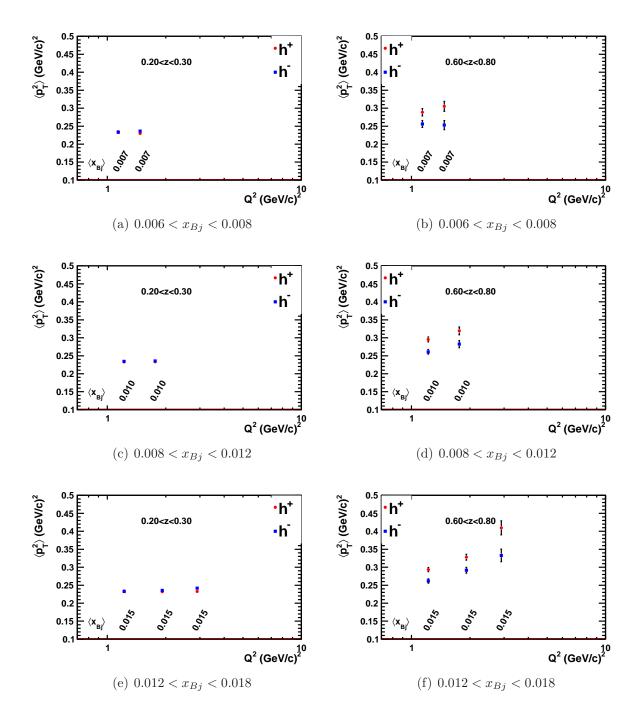


Figure 7.18: $\langle P_T^2 \rangle$ vs Q^2 in different x_{Bj} intervals for low (left column) and high (right column) z. The red points and blue square markers are for positive and negative hadrons, respectively. The separation between positive and negative hadrons for the high z hadrons was also observed at HERMES for $\langle P_T \rangle$ in [47].

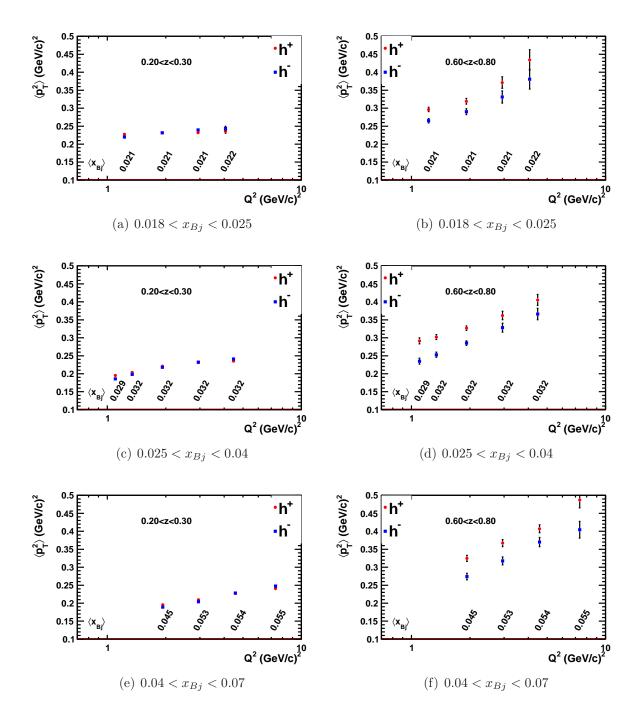


Figure 7.19: $\langle P_T^2 \rangle$ vs Q^2 in different x_{Bj} intervals for low (left column) and high (right column) z. The red points and blue square markers are for positive and negative hadrons, respectively. The separation between positive and negative hadrons for the high z hadrons was also observed at HERMES for $\langle P_T \rangle$ in [47].

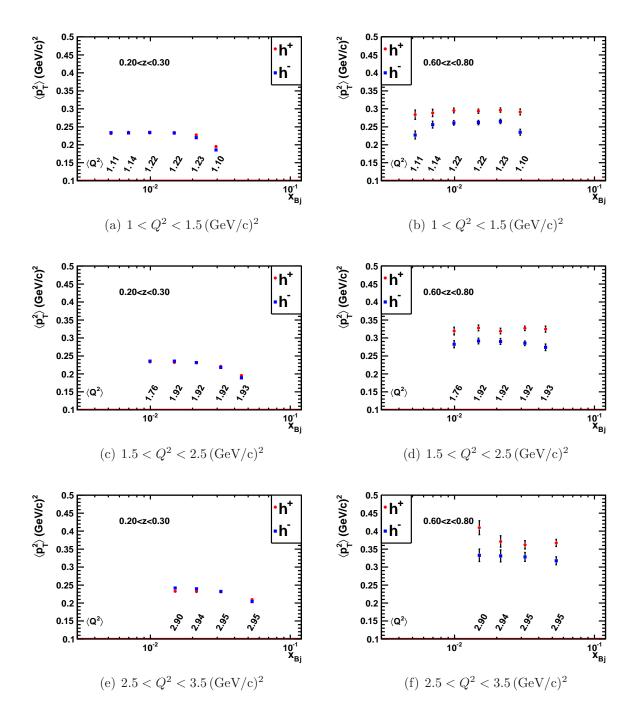


Figure 7.20: $\langle P_T^2 \rangle$ vs x_{Bj} in different Q^2 intervals for low (left column) and high (right column) z. The red points and blue square markers are for positive and negative hadrons, respectively. The separation between positive and negative hadrons for the high z hadrons was also observed at HERMES for $\langle P_T \rangle$ in [47].

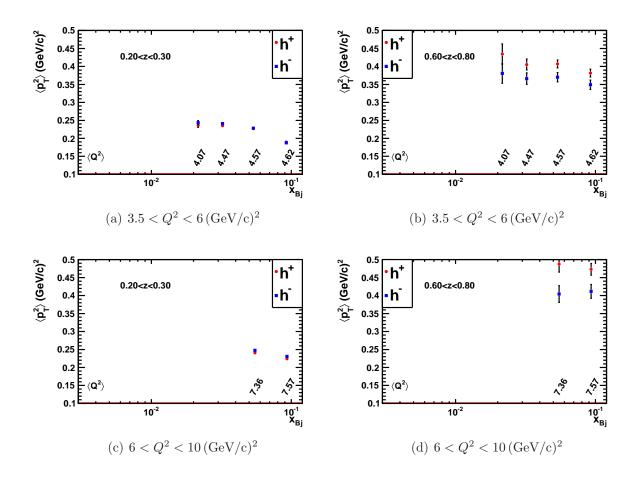


Figure 7.21: $\langle P_T^2 \rangle$ vs x_{Bj} in different Q^2 intervals for low (left column) and high (right column) z. The red points and blue square markers are for positive and negative hadrons, respectively. The separation between positive and negative hadrons for the high z hadrons was also observed at HERMES for $\langle P_T \rangle$ in [47].

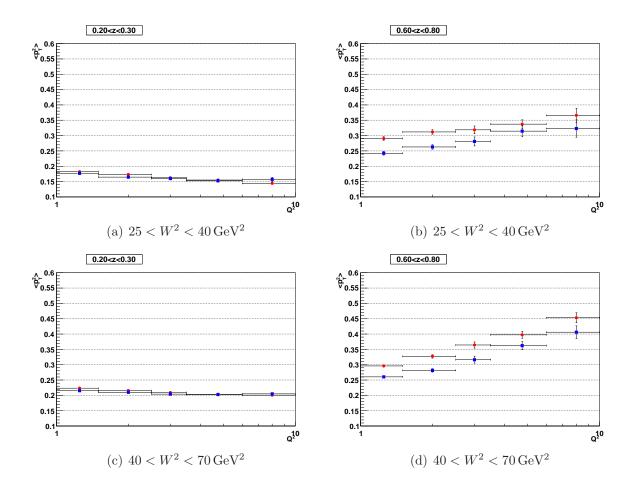


Figure 7.22: $\langle P_T^2 \rangle$ vs Q^2 (in units of $(\text{GeV/c})^2$) for low (left column) and high (right column) z in different invariant mass bins, W^2 : [25, 40], [40, 70] GeV². The red points and blue square markers are for positive and negative hadrons, respectively.

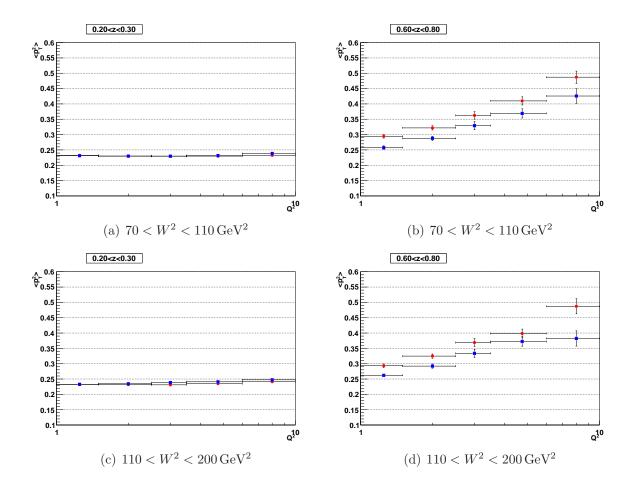


Figure 7.23: $\langle P_T^2 \rangle$ vs Q^2 (in units of $(\text{GeV/c})^2$) for low (left column) and high (right column) z in different invariant mass bins, W^2 : [70, 110], [110, 200] GeV². The red points and blue square markers are for positive and negative hadrons, respectively.

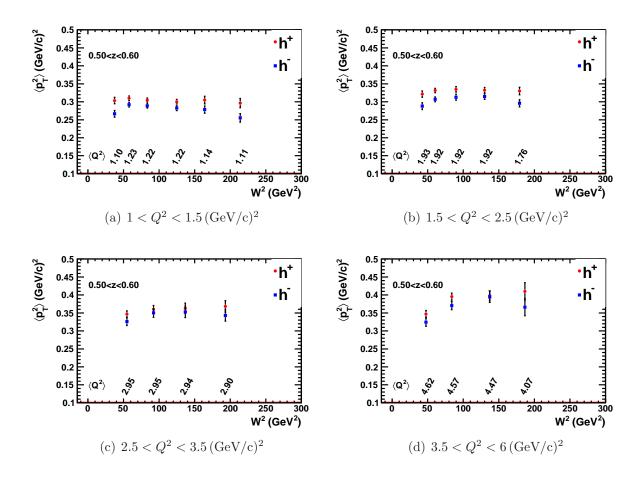


Figure 7.24: $\langle P_T^2 \rangle$ vs W^2 in fixed Q^2 intervals for middle z. The red points and blue square markers are for positive and negative hadrons, respectively. This is to be compared with figure 7.11 where the mean p_T^2 is plotted (i.e. all p_T^2 are considered). In the present figure, the $\langle P_T^2 \rangle$ result from a fit of the $p_T < 0.85$ GeV/c. This figure shows that there is no clear W^2 -dependence for the fitted $\langle P_T^2 \rangle$.

7.5.1 Dependence of $\langle p_T^2 \rangle$ on the hadron energy fraction z

The fitted $\langle p_T^2 \rangle$ was evaluated at different z intervals as shown, for example, in figure 7.25. The highest z intervals (z: [0.8, 0.9], [0.9, 1]) have been excluded because the p_T distributions did not followed the Gaussian behavior of equation (4.82). The $\langle p_T^2 \rangle$ fit was performed for every (Q^2, x_{Bi}) intervals and the results are shown in figures 7.25, 7.26, 7.27, 7.28, 7.29 and 7.30. It is obvious from these plots that the relation between $\langle p_T^2 \rangle$ and z^2 is not linear as in equation (4.83). For example, there is a flattening (even a decrease in some cases) of $\langle p_T^2 \rangle$ for the higher z. This behavior was also observed for $\langle p_T \rangle$ at HERMES [47]. As possible explanation is a z-dependence of the transverse momentum acquired during fragmentation. For $z \to 1$, the hadron carries almost all of the virtual photon momentum; it probably did not go through many fragmentation steps. The fewer fragmentation processes reduce the chances of the hadrons to acquire transverse momentum during fragmentation. This behavior is reproduced by introducing a factor $(1-z)^{\beta}$ in front of $\langle p_{\perp}^2 \rangle$. For the lower z, the hadron has very little energy and could not have gain much transverse momentum during fragmentation up to the extreme case of $z \to 0$ where there is no energy available for transverse momentum. This behavior is reproduced by including a factor z^{α} in front of $\langle p_{\perp}^2 \rangle$. With these two effects combined, relation (4.83) is rewritten as

$$\langle p_T^2 \rangle = z^{\alpha} (1-z)^{\beta} \langle p_{\perp}^2 \rangle + z^2 \langle k_{\perp}^2 \rangle.$$
(7.3)

where the values $\alpha = 0.5$ and $\beta = 1.5$ are modified fit results tuned to HERMES data [59].

7.5.2 Dependence of $\langle k_{\perp}^2 \rangle$ on inclusive variables

The intrinsic transverse momentum is extracted using (7.3) to fit the relation between $\langle p_T^2 \rangle$ and z^2 . Figure 7.31 shows the dependence of $\langle k_{\perp}^2 \rangle$ on different inclusive variables. Before commenting the results, it is to be noted that photon radiations (so called radiative effect) can also affect the transverse momentum. Since p_T is defined with respect to the virtual photon direction, a wrong determination of the photon direction leads to a wrong p_T . The photon direction is determined with the incoming and scattered muon, but if the muon radiates another photon between those two measurements (radiative effect as shown in figure 4.6), then the assumed photon kinematics are wrong. This effect has been investigated in [22] and was considered to be of the order of $\leq 0.02 \,\text{GeV}^2$ in $\langle p_T^2 \rangle$, but this was for a different beam energy (280 GeV) than COMPASS (160 GeV). With all these possible effects considered, some features of $\langle k_1^2 \rangle$ can be observed from 7.31:

- $\langle k_{\perp}^2 \rangle$ always increases with Q^2 .
- $\langle k_{\perp}^2 \rangle$ from positive hadrons is always higher than for negative hadrons usually by about 0.1 (GeV/c)².

As discussed above, the model used to extract $\langle k_{\perp}^2 \rangle$ is valid only up to $\mathcal{O}\left(\frac{k_{\perp}}{Q}\right)$. Therefore, the results are more reliable at high Q^2 , where positive hadrons h^+ have always higher $\langle k_{\perp}^2 \rangle$

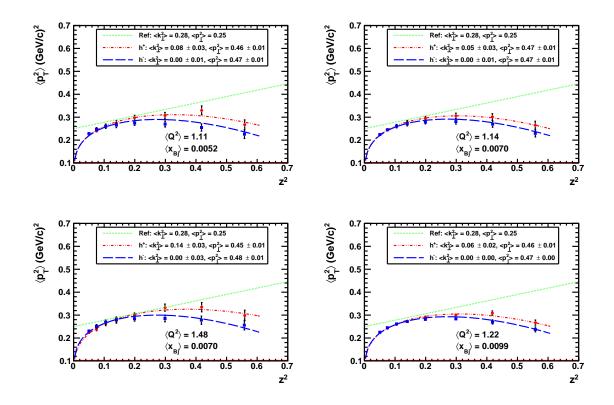


Figure 7.25: $\langle p_T^2 \rangle$ from the Gaussian fit of differential multiplicity as function of z^2 . The blue square and red dots are for negative and positive hadrons, respectively. The dotted green line is the parametrization of the linear relation (4.83) by [16]. The blue dashed line and the red dash-dotted line are the result of fitting the function (7.3) for the positive and negative hadrons, respectively.

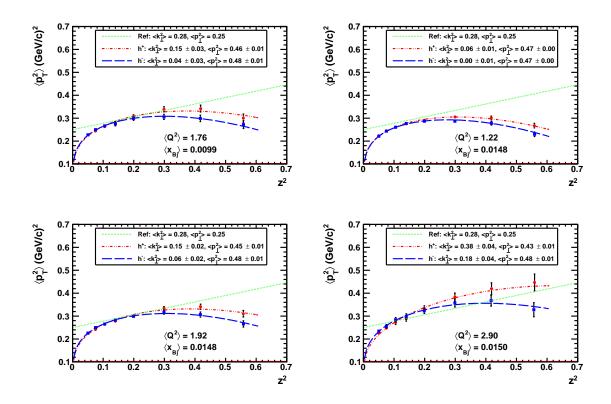


Figure 7.26: $\langle p_T^2 \rangle$ from the Gaussian fit of differential multiplicity as function of z^2 . The blue square and red dots are for negative and positive hadrons, respectively. The dotted green line is the parametrization of the linear relation (4.83) by [16]. The blue dashed line and the red dash-dotted line are the result of fitting the function (7.3) for the positive and negative hadrons, respectively.

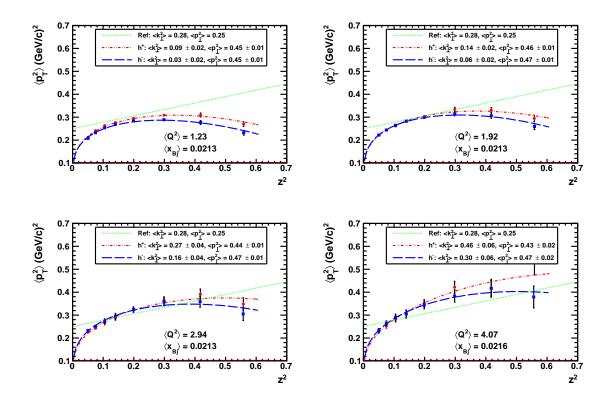


Figure 7.27: $\langle p_T^2 \rangle$ from the Gaussian fit of differential multiplicity as function of z^2 . The blue square and red dots are for negative and positive hadrons, respectively. The dotted green line is the parametrization of the linear relation (4.83) by [16]. The blue dashed line and the red dash-dotted line are the result of fitting the function (7.3) for the positive and negative hadrons, respectively.

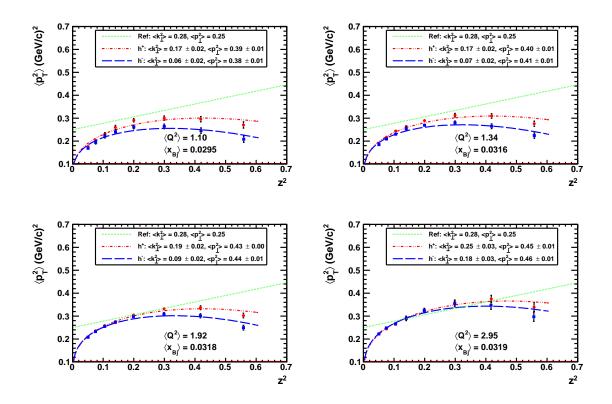


Figure 7.28: $\langle p_T^2 \rangle$ from the Gaussian fit of differential multiplicity as function of z^2 . The blue square and red dots are for negative and positive hadrons, respectively. The dotted green line is the parametrization of the linear relation (4.83) by [16]. The blue dashed line and the red dash-dotted line are the result of fitting the function (7.3) for the positive and negative hadrons, respectively.

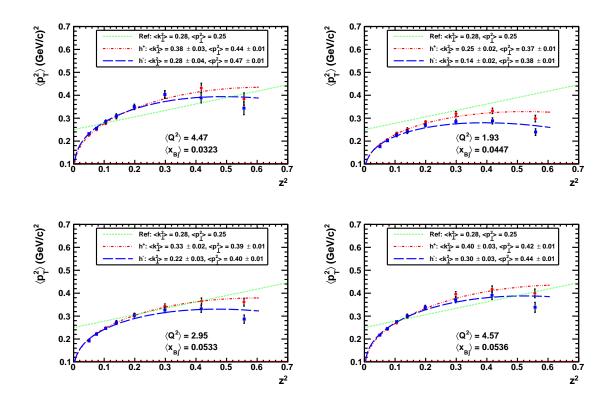


Figure 7.29: $\langle p_T^2 \rangle$ from the Gaussian fit of differential multiplicity as function of z^2 . The blue square and red dots are for negative and positive hadrons, respectively. The dotted green line is the parametrization of the linear relation (4.83) by [16]. The blue dashed line and the red dash-dotted line are the result of fitting the function (7.3) for the positive and negative hadrons, respectively.

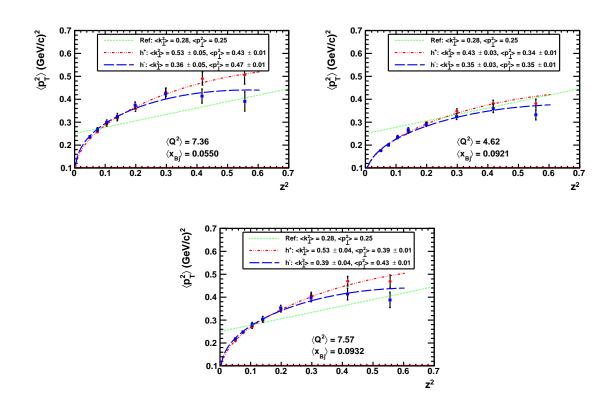


Figure 7.30: $\langle p_T^2 \rangle$ from the Gaussian fit of differential multiplicity as function of z^2 . The blue square and red dots are for negative and positive hadrons, respectively. The dotted green line is the parametrization of the linear relation (4.83) by [16]. The blue dashed line and the red dash-dotted line are the result of fitting the function (7.3) for the positive and negative hadrons, respectively.

than negative hadrons h^- and do not show a clear dependence on x_{Bj} . The dependence on Q^2 is not expected from a simple interpretation, but it could be explained if gluon radiation plays a role even at these low p_T ⁴. Such effect could indeed give a Q^2 dependence on k_{\perp} as suggested in [30]. The difference of $\langle k_{\perp}^2 \rangle$ between positive and negative hadrons, observed for all kinematic intervals of this analysis, could be a sign of flavor dependence of the transverse momentum dependent distribution functions (TMDs). The standard collinear PDFs are not flavor independent so there is no reason to expect the TMDs to be flavor independent (see e.g. [23]). Flavor dependence was also suggested for valence quarks from the interpretation of the JLab results [53].

⁴As explained above, the distributions were fitted only up to $P_T = 0.85$ GeV/c to avoid pQCD effect, as suggested in [17] and [16].

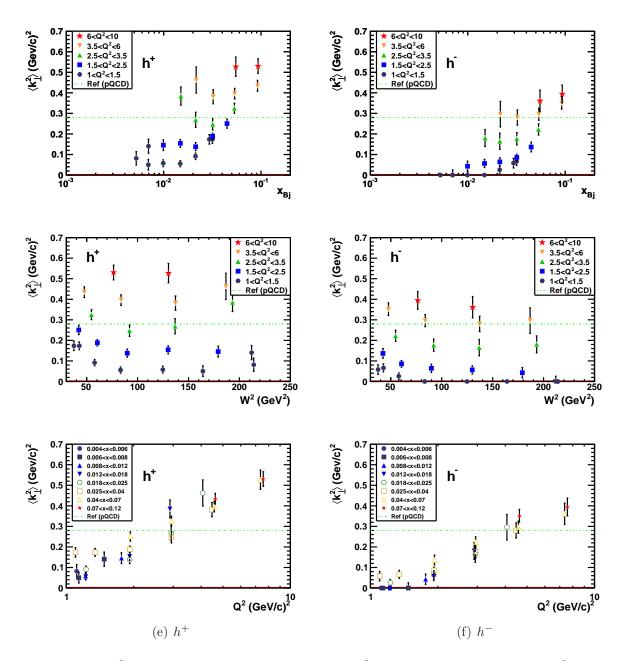


Figure 7.31: $\langle k_{\perp}^2 \rangle$ dependence on x_{Bj} (first row), W^2 (second row) for different Q^2 intervals and Q^2 (third row). The $\langle k_{\perp}^2 \rangle$ are extracted from fitted $\langle p_T^2 \rangle$ at different z using the relation (7.3). The dotted green line is the parametrization of the linear relation (4.83) by [16].

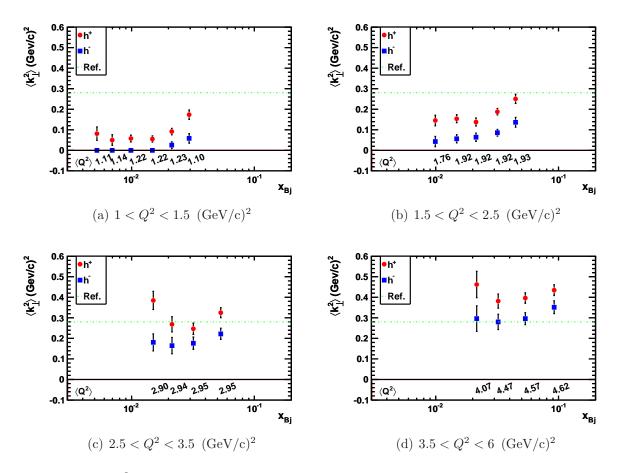


Figure 7.32: $\langle k_{\perp}^2 \rangle$ dependence on x_{Bj} for positive and negative hadron comparison. The $\langle k_{\perp}^2 \rangle$ are extracted from fitted $\langle p_T^2 \rangle$ at different z using the relation (7.3). The dotted green line is the parametrization of the linear relation (4.83) by [16].

Chapter 8

Conclusion and outlook

The differential multiplicities and cross sections as function of transverse momentum of hadrons produced by muons on a ⁶LiD target have been measured. They can be used to verify models of nucleon structure and interactions. If the model only includes single photon exchange, each multiplicity has to be scaled by the appropriate radiative correction factor.

The differential multiplicities have been determined at different z such that the intrinsic transverse momentum could be extracted according a given model. This model assumes Gaussian distributions for both the intrinsic transverse momentum of partons and the acquired transverse momentum of hadron during the fragmentation. It has been shown that the resulting linear relation between the hadron average transverse momentum and z^2 is too simple to describe the data. A simple modification of the linear relation taking into account a z dependence of the acquired transverse momentum during fragmentation can reproduce the data very well. From this modified model, the intrinsic transverse momentum has been extracted for different intervals of the exchange photon kinematics. This extraction is based on the single photon exchange approximation. The radiative effects were determined to be small for the muon nucleon scattering EMC experiment at 280 GeV. The work to verify if these effects might be more significant at COMPASS energy (160 GeV) is in progress.

Although this model is quite simple, the results presented here provide new insights into the partonic structure of the nucleon. The higher extracted intrinsic momentum for positive hadrons might be an effect of flavor dependence. Indeed, a positively charged hadron has more chance to comprise the struck positive (mostly up) quark. Similarly, a negative hadron has more chance to comprise a negative quark (mostly down) quark. Hadrons with higher z have more chance to contain the struck quark, so a flavor dependence is expected to be stronger for those hadrons. That is exactly what is observed in this thesis.

Based on these results, there are many further studies and further improvements that could be suggested. As mentioned above, this analysis does not use all the power of the COM-PASS spectrometer. The next natural step is to determine the differential cross section for identified hadrons, namely pions and kaons. Now that the charged hadron acceptance is well understood, the inclusion of the RICH detector acceptance can be determined on firm grounds. Cross sections of identified hadrons are very interesting because they are easier to compare with theoretical models. They also provide a cleaner insight to the structure of the nucleon. For example, when a kaon is observed, especially at high z, there are good chances that it contains a strange quark from the nucleon. This would be a great opportunity to verify the flavor dependence of the intrinsic transverse momentum of the partons.

Another suggestion is to measure the azimuthal distribution of the multiplicities. This would require a more detailed study of the azimuthal description of the spectrometer simulation to correct for the acceptance. These studies would be very interesting because they provide a different way to access the intrinsic momentum. A confirmation of the present results would increase confidence in the conclusions of this thesis. Moreover, the azimuthal dependence of the cross section is linear as function of z, rather than function of z^2 here, which is more robust for fitting.

The transverse momentum dependent (TMD) distribution functions are natural extensions of the standard collinear PDFs from one to three dimensions in momentum space. The study of TMD is a flourishing subject both on the theoretical and experimental side. They can be extracted from experimental data, as was demonstrated in this analysis, and allow theoreticians to make predictions for hard-scattering experiments involving nucleons. The study of TMDs reveals crucial aspects of the dynamics of confined partons. COMPASS is a key player to these studies because of its unique kinematic coverage. This study of TMDs through intrinsic momentum is then a direct contribution to a main goal of COMPASS, to improve our knowledge of the nucleon structure.

In a near future, COMPASS intends to have a muon beam on a polarized hydrogen target for deeply virtual Compton scattering studies. This will be an opportunity to further study semi-inclusive deep inelastic scattering. The conditions are even more favorable since the target will be pure protons.

Appendix A F_2 comparison period by period

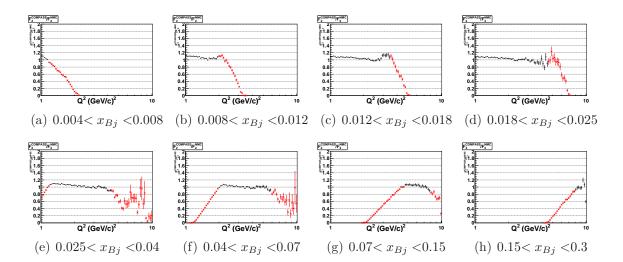


Figure A.1: F_2 comparison (COMPASS/SMC) for inclusive middle trigger. Same as for figure 6.16, but only data from period W22

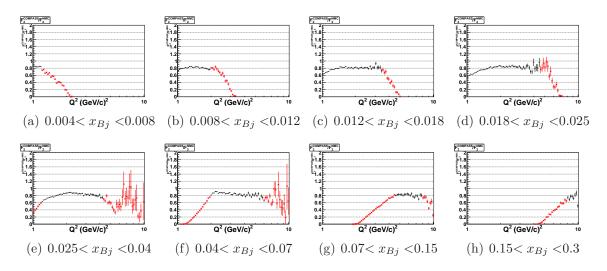


Figure A.2: F_2 comparison (COMPASS/SMC) for inclusive middle trigger. Same as for figure 6.16, but only data from period W23

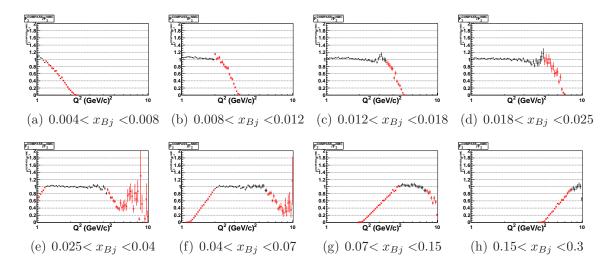


Figure A.3: F_2 comparison (COMPASS/SMC) for inclusive middle trigger. Same as for figure 6.16, but only data from period W26

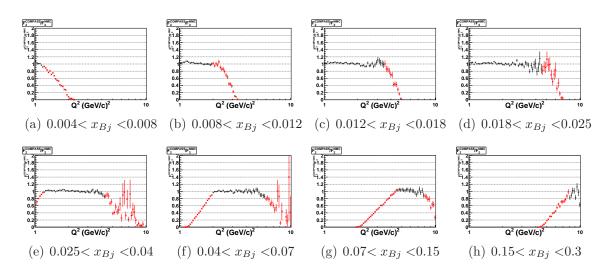


Figure A.4: F_2 comparison (COMPASS/SMC) for inclusive middle trigger. Same as for figure 6.16, but only data from period W27

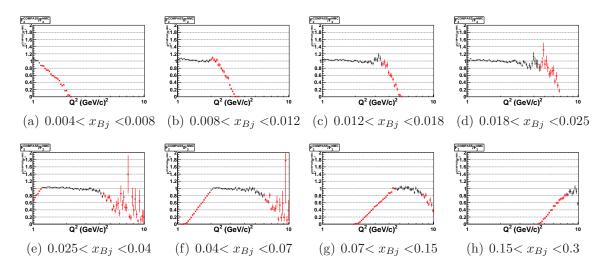


Figure A.5: F_2 comparison (COMPASS/SMC) for inclusive middle trigger. Same as for figure 6.16, but only data from period W30

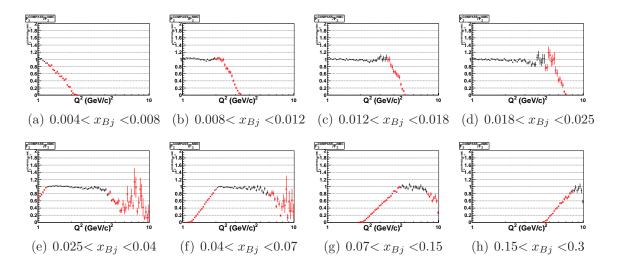


Figure A.6: F_2 comparison (COMPASS/SMC) for inclusive middle trigger. Same as for figure 6.16, but only data from period W31

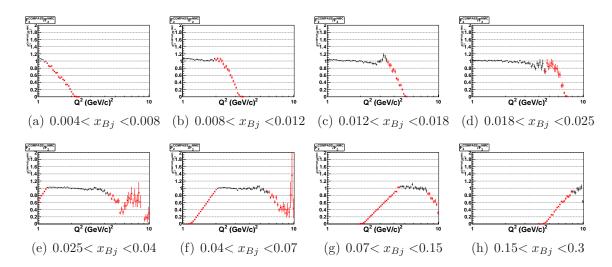


Figure A.7: F_2 comparison (COMPASS/SMC) for inclusive middle trigger. Same as for figure 6.16, but only data from period W32

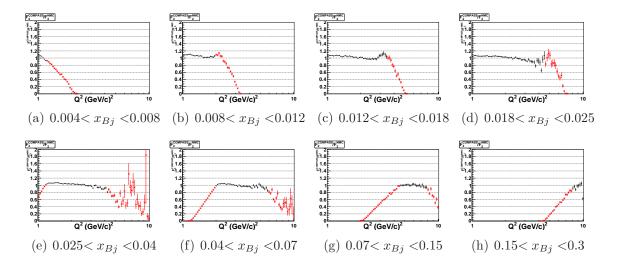


Figure A.8: F_2 comparison (COMPASS/SMC) for inclusive middle trigger. Same as for figure 6.16, but only data from period W37

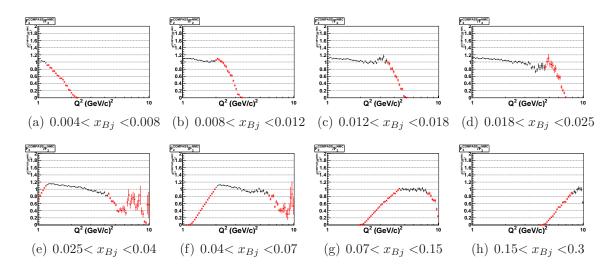


Figure A.9: F_2 comparison (COMPASS/SMC) for inclusive middle trigger. Same as for figure 6.16, but only data from period W38

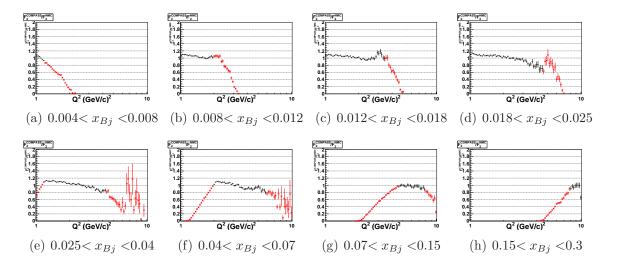


Figure A.10: F_2 comparison (COMPASS/SMC) for inclusive middle trigger. Same as for figure 6.16, but only data from period W39

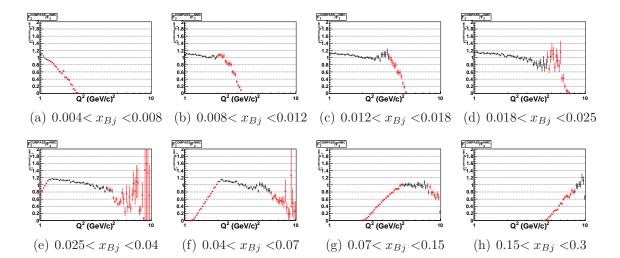


Figure A.11: F_2 comparison (COMPASS/SMC) for inclusive middle trigger. Same as for figure 6.16, but only data from period W40

Appendix B

Information about the inclusive cross section

	Bin	$\langle Q^2 \rangle$	$\langle x_{Bj} \rangle$	$\langle W^2 \rangle$	F_2	$d^2\sigma_{1\gamma}/dQ^2dx_{Bj}$	η	η_h	$d^2\sigma_{meas}/dQ^2dx_{Bj}$	Incl. Frac
ĺ	10	1.113391	0.005230	213.989583	0.293896	0.014154	0.811289	0.872112	0.017048	68.9%
	20	1.137434	0.006965	164.150764	0.289890	0.012047	0.866023	0.890972	0.013725	53.1%
	30	1.476151	0.006988	211.957669	0.321926	0.006674	0.820774	0.869704	0.008021	76.9%
	40	1.219922	0.009883	124.798256	0.292939	0.008640	0.892170	0.903912	0.009619	48.6%
	50	1.762530	0.009923	179.155740	0.333617	0.003868	0.861093	0.884515	0.004457	71.7%
	60	1.221604	0.014799	83.328595	0.290994	0.006627	0.912322	0.917979	0.007240	46.6%
	70	1.917223	0.014827	130.014259	0.334189	0.002612	0.894804	0.903902	0.002907	61.7%
	80	2.902372	0.015035	193.182492	0.372908	0.001011	0.854621	0.877439	0.001178	86.2%
	90	1.225755	0.021265	57.808954	0.292310	0.005026	0.926480	0.930132	0.005414	49.3%
	100	1.918099	0.021299	89.836072	0.329453	0.002061	0.914506	0.918612	0.002250	56.6%
	110	2.935501	0.021332	136.787054	0.363415	0.000822	0.895168	0.903030	0.000916	76.7%
	120	4.066024	0.021574	186.692070	0.388249	0.000383	0.864194	0.881540	0.000443	92.4%
	130	1.098759	0.029452	37.419096	0.286444	0.004750	0.940570	0.943814	0.005043	58.1%
	140	1.343157	0.031648	42.752374	0.301846	0.003063	0.939457	0.942021	0.003256	56.6%
	150	1.920943	0.031791	60.484356	0.326517	0.001515	0.931753	0.933925	0.001624	56.9%
	160	2.946580	0.031859	92.121209	0.354210	0.000624	0.919109	0.922020	0.000678	72.1%
	170	4.468403	0.032262	137.209132	0.379214	0.000245	0.900212	0.906288	0.000272	87.1%
	180	1.931619	0.044724	42.311941	0.325266	0.001126	0.945119	0.946815	0.001191	62.2%
	190	2.948099	0.053286	54.708268	0.344541	0.000413	0.942503	0.943883	0.000438	74.5%
	200	4.572572	0.053602	83.781432	0.363020	0.000162	0.929663	0.931579	0.000174	82.0%
	210	7.357470	0.055026	130.305320	0.380071	0.000054	0.910652	0.914856	0.000060	94.3%
	220	4.621906	0.092060	47.660472	0.345310	0.000099	0.956632	0.957904	0.000104	85.8%
	230	7.568745	0.093185	76.424263	0.354741	0.000034	0.942501	0.944113	0.000036	91.5%

Table B.1: SMC inclusive cross section and the parameters used for its determination. The structure function F_2 is taken from the SMC fit [6], the radiative correction factors are taken from [24]. The last column (Incl. Frac.) is the fraction of events that were triggered without requiring calorimeter signals. The measured differential cross section was determined by an appropriate mix of η and η_h based on the fraction of inclusive events (Incl. Frac.). The fraction of inclusive events as function of Q^2 and x_{Bj} is shown in figure B.1.

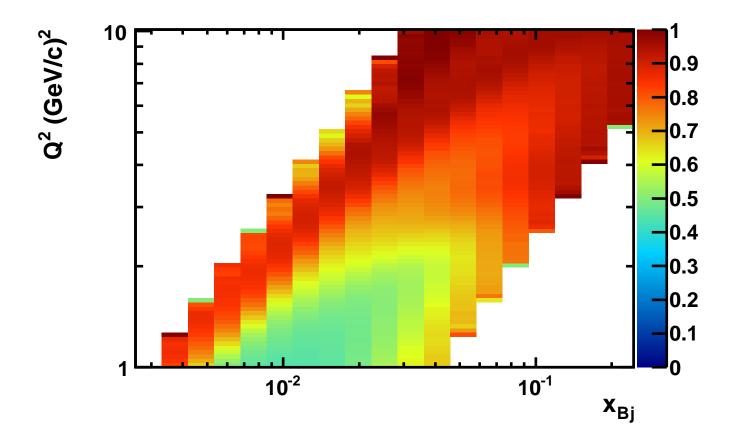


Figure B.1: Fraction of events that were triggered without requiring calorimeter signals as function of Q^2 and x_{Bj} .

Appendix C

Fit tables

Bin	$\langle z^2 \rangle_{h^+}$	$\langle P_T^2 \rangle_{h^+}$	A_{h^+}	$\chi^2_{h^+}/ndf$	$\langle z^2 \rangle_{h^-}$	$\langle P_T^2 \rangle_{h^-}$	A_{h^-}	$\chi^2_{h^-}/ndf$
1	0.05	0.23 ± 0.006	8.51 ± 0.059	8.4	0.05	0.23 ± 0.006	8.25 ± 0.058	5.3
2	0.07	0.24 ± 0.007	5.56 ± 0.048	6.1	0.07	0.25 ± 0.007	5.30 ± 0.045	3.1
3	0.11	0.26 ± 0.009	3.67 ± 0.037	2.6	0.10	0.26 ± 0.009	3.54 ± 0.037	3.0
4	0.14	0.27 ± 0.011	2.56 ± 0.031	2.1	0.14	0.27 ± 0.011	2.53 ± 0.031	2.2
5	0.20	0.30 ± 0.010	1.52 ± 0.016	2.5	0.20	0.27 ± 0.010	1.63 ± 0.018	3.9
6	0.30	0.31 ± 0.014	0.86 ± 0.012	3.4	0.30	0.27 ± 0.013	0.98 ± 0.014	3.5
7	0.42	0.33 ± 0.020	0.48 ± 0.009	3.6	0.42	0.26 ± 0.016	0.64 ± 0.011	4.8
8	0.56	0.27 ± 0.021	0.39 ± 0.009	2.5	0.56	0.23 ± 0.019	0.46 ± 0.010	4.5

Table C.1: Fit results for $0.0045 < x_{Bj} < 0.006$ and $1 < Q^2 < 1.25 (\text{GeV/c})^2$. All variables are defined in the text except $A_{h^{+,-}}$, the fitted Gaussian amplitude. Only statistical error were used for the fit, this explains the high χ^2 in the low z intervals were the statistical error is very small.

Bin	$\langle z^2 \rangle_{h^+}$	$\langle P_T^2 \rangle_{h^+}$	A_{h^+}	$\chi^2_{h^+}/ndf$	$\langle z^2 \rangle_{h^-}$	$\langle P_T^2 \rangle_{h^-}$	A_{h^-}	$\chi^2_{h^-}/ndf$
11	0.05	0.22 ± 0.004	10.01 ± 0.056	7.4	0.05	0.22 ± 0.005	9.43 ± 0.054	9.0
12	0.07	0.25 ± 0.006	6.46 ± 0.044	5.3	0.07	0.25 ± 0.006	6.05 ± 0.042	5.3
13	0.10	0.26 ± 0.007	4.34 ± 0.036	3.5	0.11	0.26 ± 0.007	4.01 ± 0.034	3.7
14	0.14	0.28 ± 0.009	3.00 ± 0.029	2.6	0.14	0.27 ± 0.009	2.83 ± 0.029	3.9
15	0.20	0.30 ± 0.008	1.87 ± 0.016	3.5	0.20	0.28 ± 0.008	1.79 ± 0.016	4.3
16	0.30	0.31 ± 0.011	1.03 ± 0.012	3.3	0.30	0.28 ± 0.011	1.05 ± 0.012	2.8
17	0.42	0.30 ± 0.015	0.63 ± 0.009	4.3	0.42	0.27 ± 0.014	0.66 ± 0.010	3.7
18	0.56	0.26 ± 0.017	0.45 ± 0.009	3.7	0.56	0.23 ± 0.016	0.51 ± 0.010	3.9

Table C.2: Fit results for $0.006 < x_{Bj} < 0.008$ and $1 < Q^2 < 1.3$. All variables are defined in the text except $A_{h^{+,-}}$, the fitted Gaussian amplitude. Only statistical error were used for the fit, this explains the high χ^2 in the low z intervals were the statistical error is very small.

Bin	$\langle z^2 \rangle_{h^+}$	$\langle P_T^2 \rangle_{h^+}$	A_{h^+}	$\chi^2_{h^+}/ndf$	$\langle z^2 \rangle_{h^-}$	$\langle P_T^2 \rangle_{h^-}$	A_{h^-}	$\chi^2_{h^-}/ndf$
21	0.05	0.22 ± 0.006	8.57 ± 0.062	9.6	0.05	0.23 ± 0.006	8.29 ± 0.059	5.4
22	0.07	0.24 ± 0.007	5.62 ± 0.049	5.2	0.07	0.25 ± 0.008	5.22 ± 0.046	2.3
23	0.11	0.26 ± 0.009	3.65 ± 0.038	2.0	0.10	0.27 ± 0.009	3.45 ± 0.036	2.3
24	0.14	0.28 ± 0.011	2.51 ± 0.031	1.2	0.14	0.28 ± 0.012	2.41 ± 0.030	1.7
25	0.20	0.30 ± 0.011	1.49 ± 0.017	1.4	0.20	0.28 ± 0.011	1.50 ± 0.017	3.0
26	0.30	0.33 ± 0.016	0.77 ± 0.012	2.5	0.30	0.29 ± 0.014	0.89 ± 0.013	3.9
27	0.42	0.33 ± 0.020	0.46 ± 0.009	3.1	0.42	0.28 ± 0.018	0.54 ± 0.010	3.1
28	0.56	0.30 ± 0.023	0.35 ± 0.008	1.8	0.56	0.26 ± 0.021	0.39 ± 0.009	1.8

Table C.3: Fit results for $0.006 < x_{Bj} < 0.008$ and $1.3 < Q^2 < 1.7$. All variables are defined in the text except $A_{h^{+,-}}$, the fitted Gaussian amplitude. Only statistical error were used for the fit, this explains the high χ^2 in the low z intervals were the statistical error is very small.

Bin	$\langle z^2 \rangle_{h^+}$	$\langle P_T^2 \rangle_{h^+}$	A_{h^+}	$\chi^2_{h^+}/ndf$	$\langle z^2 \rangle_{h^-}$	$\langle P_T^2 \rangle_{h^-}$	A_{h^-}	$\chi^2_{h^-}/ndf$
31	0.05	0.22 ± 0.003	10.67 ± 0.037	15.7	0.05	0.23 ± 0.003	9.84 ± 0.036	12.6
32	0.07	0.24 ± 0.004	6.96 ± 0.030	10.9	0.07	0.24 ± 0.004	6.25 ± 0.028	8.5
33	0.11	0.26 ± 0.004	4.71 ± 0.024	3.6	0.11	0.26 ± 0.005	4.14 ± 0.023	5.5
34	0.14	0.27 ± 0.006	3.31 ± 0.020	5.1	0.14	0.27 ± 0.006	2.89 ± 0.019	5.8
35	0.20	0.29 ± 0.005	2.03 ± 0.011	4.4	0.20	0.28 ± 0.005	1.82 ± 0.011	6.0
36	0.30	0.30 ± 0.007	1.15 ± 0.008	5.1	0.30	0.28 ± 0.007	1.06 ± 0.008	5.6
37	0.42	0.31 ± 0.009	0.68 ± 0.006	6.1	0.42	0.27 ± 0.009	0.69 ± 0.007	7.1
38	0.56	0.27 ± 0.011	0.50 ± 0.006	11.5	0.56	0.24 ± 0.011	0.52 ± 0.006	10.8

Table C.4: Fit results for $0.008 < x_{Bj} < 0.012$ and $1 < Q^2 < 1.5 (\text{GeV/c})^2$. All variables are defined in the text except $A_{h^{+,-}}$, the fitted Gaussian amplitude. Only statistical error were used for the fit, this explains the high χ^2 in the low z intervals were the statistical error is very small.

Bin	$\langle z^2 \rangle_{h^+}$	$\langle P_T^2 \rangle_{h^+}$	A_{h^+}	$\chi^2_{h^+}/ndf$	$\langle z^2 \rangle_{h^-}$	$\langle P_T^2 \rangle_{h^-}$	$A_{h^{-}}$	$\chi^2_{h^-}/ndf$
41	0.05	0.23 ± 0.004	9.54 ± 0.049	11.8	0.05	0.23 ± 0.004	9.09 ± 0.047	9.4
42	0.07	0.24 ± 0.005	6.17 ± 0.039	7.3	0.07	0.25 ± 0.006	5.69 ± 0.036	5.0
43	0.11	0.26 ± 0.007	4.10 ± 0.031	2.9	0.11	0.27 ± 0.007	3.76 ± 0.029	3.2
44	0.14	0.28 ± 0.008	2.83 ± 0.025	2.4	0.14	0.28 ± 0.009	2.62 ± 0.024	3.5
45	0.20	0.31 ± 0.008	1.65 ± 0.013	2.8	0.20	0.30 ± 0.008	1.57 ± 0.013	3.6
46	0.30	0.34 ± 0.011	0.85 ± 0.009	1.9	0.30	0.31 ± 0.011	0.86 ± 0.010	2.3
47	0.42	0.34 ± 0.015	0.49 ± 0.007	2.4	0.42	0.30 ± 0.014	0.52 ± 0.007	3.1
48	0.56	0.30 ± 0.018	0.35 ± 0.006	3.9	0.56	0.27 ± 0.017	0.36 ± 0.007	2.2

Table C.5: Fit results for $0.008 < x_{Bj} < 0.012$ and $1.5 < Q^2 < 2.1$. All variables are defined in the text except $A_{h^{+,-}}$, the fitted Gaussian amplitude. Only statistical error were used for the fit, this explains the high χ^2 in the low z intervals were the statistical error is very small.

Bin	$\langle z^2 \rangle_{h^+}$	$\langle P_T^2 \rangle_{h^+}$	A_{h^+}	$\chi^2_{h^+}/ndf$	$\langle z^2 \rangle_{h^-}$	$\langle P_T^2 \rangle_{h^-}$	A_{h^-}	$\chi^2_{h^-}/ndf$
51	0.05	0.22 ± 0.003	11.57 ± 0.037	9.6	0.05	0.22 ± 0.003	10.57 ± 0.036	10.5
52	0.07	0.24 ± 0.003	7.48 ± 0.029	5.7	0.07	0.24 ± 0.004	6.71 ± 0.028	6.8
53	0.11	0.26 ± 0.004	5.07 ± 0.023	3.3	0.11	0.26 ± 0.004	4.44 ± 0.022	4.3
54	0.14	0.28 ± 0.005	3.57 ± 0.020	3.1	0.14	0.28 ± 0.005	3.02 ± 0.018	4.4
55	0.20	0.29 ± 0.005	2.23 ± 0.011	4.4	0.20	0.29 ± 0.005	1.87 ± 0.010	5.8
56	0.30	0.31 ± 0.006	1.26 ± 0.008	6.1	0.30	0.29 ± 0.007	1.09 ± 0.008	6.0
57	0.42	0.30 ± 0.008	0.78 ± 0.007	9.7	0.42	0.28 ± 0.008	0.69 ± 0.006	8.2
58	0.56	0.27 ± 0.010	0.57 ± 0.006	13.5	0.56	0.23 ± 0.010	0.55 ± 0.006	14.1

Table C.6: Fit results for $0.012 < x_{Bj} < 0.018$ and $1 < Q^2 < 1.5 (\text{GeV/c})^2$. All variables are defined in the text except $A_{h^{+,-}}$, the fitted Gaussian amplitude. Only statistical error were used for the fit, this explains the high χ^2 in the low z intervals were the statistical error is very small.

Bin	$\langle z^2 \rangle_{h^+}$	$\langle P_T^2 \rangle_{h^+}$	A_{h^+}	$\chi^2_{h^+}/ndf$	$\langle z^2 \rangle_{h^{-}}$	$\langle P_T^2 \rangle_{h^-}$	$A_{h^{-}}$	$\chi^2_{h^-}/ndf$
61	0.05	0.22 ± 0.003	10.65 ± 0.040	14.4	0.05	0.23 ± 0.003	9.79 ± 0.038	10.2
62	0.07	0.24 ± 0.004	6.96 ± 0.032	7.1	0.07	0.25 ± 0.004	6.04 ± 0.029	4.8
63	0.11	0.26 ± 0.005	4.53 ± 0.025	4.8	0.10	0.27 ± 0.005	4.04 ± 0.023	3.4
64	0.14	0.28 ± 0.006	3.16 ± 0.021	2.2	0.14	0.28 ± 0.006	2.72 ± 0.019	2.5
65	0.20	0.30 ± 0.006	1.90 ± 0.011	2.3	0.20	0.30 ± 0.006	1.62 ± 0.010	2.3
66	0.30	0.33 ± 0.008	0.98 ± 0.008	2.0	0.30	0.32 ± 0.009	0.86 ± 0.007	2.7
67	0.42	0.34 ± 0.011	0.56 ± 0.006	3.9	0.42	0.31 ± 0.011	0.52 ± 0.006	5.7
68	0.56	0.31 ± 0.014	0.37 ± 0.005	8.4	0.56	0.27 ± 0.014	0.38 ± 0.006	8.8

Table C.7: Fit results for $0.012 < x_{Bj} < 0.018$ and $1.5 < Q^2 < 2.5 \text{ (GeV/c)}^2$. All variables are defined in the text except $A_{h^{+,-}}$, the fitted Gaussian amplitude. Only statistical error were used for the fit, this explains the high χ^2 in the low z intervals were the statistical error is very small.

Bin	$\langle z^2 \rangle_{h^+}$	$\langle P_T^2 \rangle_{h^+}$	A_{h^+}	$\chi^2_{h^+}/ndf$	$\langle z^2 \rangle_{h^-}$	$\langle P_T^2 \rangle_{h^-}$	A_{h^-}	$\chi^2_{h^-}/ndf$
71	0.05	0.23 ± 0.006	9.17 ± 0.063	5.7	0.05	0.23 ± 0.006	8.43 ± 0.059	3.8
72	0.07	0.25 ± 0.007	5.76 ± 0.049	2.5	0.07	0.26 ± 0.008	5.29 ± 0.046	2.1
73	0.11	0.27 ± 0.009	3.75 ± 0.038	1.2	0.10	0.28 ± 0.010	3.35 ± 0.035	1.0
74	0.14	0.29 ± 0.011	2.55 ± 0.031	0.8	0.14	0.30 ± 0.012	2.25 ± 0.029	1.1
75	0.20	0.33 ± 0.012	1.40 ± 0.016	1.5	0.20	0.32 ± 0.012	1.30 ± 0.015	2.1
76	0.30	0.38 ± 0.018	0.68 ± 0.011	1.5	0.30	0.36 ± 0.017	0.64 ± 0.010	1.2
77	0.42	0.42 ± 0.026	0.37 ± 0.008	1.3	0.42	0.37 ± 0.024	0.36 ± 0.008	1.0
78	0.56	0.45 ± 0.037	0.23 ± 0.006	2.2	0.56	0.33 ± 0.031	0.23 ± 0.007	2.2

Table C.8: Fit results for $0.012 < x_{Bj} < 0.018$ and $2.5 < Q^2 < 3.5 \text{ (GeV/c)}^2$. All variables are defined in the text except $A_{h^{+,-}}$, the fitted Gaussian amplitude. Only statistical error were used for the fit, this explains the high χ^2 in the low z intervals were the statistical error is very small.

Bin	$\langle z^2 \rangle_{h^+}$	$\langle P_T^2 \rangle_{h^+}$	A_{h^+}	$\chi^2_{h^+}/ndf$	$\langle z^2 \rangle_{h^{-}}$	$\langle P_T^2 \rangle_{h^-}$	A_{h^-}	$\chi^2_{h^-}/ndf$
81	0.05	0.21 ± 0.003	12.77 ± 0.046	7.6	0.05	0.21 ± 0.004	11.52 ± 0.045	5.2
82	0.08	0.24 ± 0.004	8.35 ± 0.034	5.7	0.08	0.23 ± 0.004	7.39 ± 0.033	3.9
83	0.11	0.26 ± 0.005	5.63 ± 0.027	2.3	0.11	0.25 ± 0.005	4.93 ± 0.026	4.2
84	0.14	0.28 ± 0.006	4.00 ± 0.023	2.6	0.14	0.27 ± 0.006	3.39 ± 0.021	3.4
85	0.20	0.30 ± 0.005	2.50 ± 0.013	2.4	0.20	0.28 ± 0.005	2.08 ± 0.012	5.4
86	0.30	0.31 ± 0.007	1.43 ± 0.009	4.6	0.30	0.29 ± 0.007	1.20 ± 0.009	4.0
87	0.42	0.31 ± 0.008	0.88 ± 0.007	5.7	0.42	0.28 ± 0.009	0.77 ± 0.007	7.0
88	0.56	0.27 ± 0.010	0.65 ± 0.007	11.0	0.56	0.23 ± 0.010	0.60 ± 0.007	11.2

Table C.9: Fit results for $0.018 < x_{Bj} < 0.025$ and $1 < Q^2 < 1.5 \ (\text{GeV/c})^2$. All variables are defined in the text except $A_{h^{+,-}}$, the fitted Gaussian amplitude. Only statistical error were used for the fit, this explains the high χ^2 in the low z intervals were the statistical error is very small.

Bin	$\langle z^2 \rangle_{h^+}$	$\langle P_T^2 \rangle_{h^+}$	A_{h^+}	$\chi^2_{h^+}/ndf$	$\langle z^2 \rangle_{h^{-}}$	$\langle P_T^2 \rangle_{h^-}$	A_{h^-}	$\chi^2_{h^-}/ndf$
91	0.05	0.22 ± 0.003	11.56 ± 0.044	7.0	0.05	0.22 ± 0.003	10.39 ± 0.042	5.8
92	0.08	0.24 ± 0.004	7.44 ± 0.034	3.9	0.07	0.24 ± 0.004	6.56 ± 0.033	4.3
93	0.11	0.26 ± 0.005	5.00 ± 0.028	2.4	0.11	0.26 ± 0.005	4.23 ± 0.025	2.2
94	0.14	0.28 ± 0.006	3.45 ± 0.023	1.5	0.14	0.28 ± 0.007	2.83 ± 0.020	1.9
95	0.20	0.30 ± 0.006	2.07 ± 0.012	2.5	0.20	0.30 ± 0.006	1.69 ± 0.011	2.8
96	0.30	0.33 ± 0.008	1.09 ± 0.009	2.2	0.30	0.32 ± 0.009	0.89 ± 0.008	2.4
97	0.42	0.33 ± 0.011	0.64 ± 0.007	3.0	0.42	0.31 ± 0.012	0.54 ± 0.006	4.3
98	0.56	0.29 ± 0.013	0.44 ± 0.006	6.3	0.56	0.26 ± 0.013	0.40 ± 0.006	4.8

Table C.10: Fit results for $0.018 < x_{Bj} < 0.025$ and $1.5 < Q^2 < 2.5 \text{ (GeV/c)}^2$. All variables are defined in the text except $A_{h^{+,-}}$, the fitted Gaussian amplitude. Only statistical error were used for the fit, this explains the high χ^2 in the low z intervals were the statistical error is very small.

Bin	$\langle z^2 \rangle_{h^+}$	$\langle P_T^2 \rangle_{h^+}$	A_{h^+}	$\chi^2_{h^+}/ndf$	$\langle z^2 \rangle_{h^-}$	$\langle P_T^2 \rangle_{h^-}$	$A_{h^{-}}$	$\chi^2_{h^-}/ndf$
101	0.05	0.22 ± 0.005	10.59 ± 0.068	7.4	0.05	0.23 ± 0.006	9.37 ± 0.063	5.1
102	0.08	0.24 ± 0.007	6.90 ± 0.053	2.1	0.07	0.25 ± 0.007	6.01 ± 0.049	1.6
103	0.11	0.27 ± 0.008	4.51 ± 0.042	1.5	0.10	0.27 ± 0.009	3.83 ± 0.039	1.4
104	0.14	0.29 ± 0.010	3.00 ± 0.034	0.9	0.14	0.30 ± 0.012	2.53 ± 0.031	1.2
105	0.20	0.32 ± 0.010	1.71 ± 0.018	1.0	0.20	0.32 ± 0.011	1.41 ± 0.016	0.7
106	0.30	0.36 ± 0.016	0.85 ± 0.012	1.2	0.30	0.36 ± 0.017	0.70 ± 0.011	1.2
107	0.42	0.39 ± 0.022	0.45 ± 0.009	1.4	0.42	0.36 ± 0.024	0.39 ± 0.008	2.2
108	0.56	0.35 ± 0.027	0.30 ± 0.007	1.7	0.56	0.30 ± 0.029	0.26 ± 0.007	2.8

Table C.11: Fit results for $0.018 < x_{Bj} < 0.025$ and $2.5 < Q^2 < 3.5 \text{ (GeV/c)}^2$. All variables are defined in the text except $A_{h^{+,-}}$, the fitted Gaussian amplitude. Only statistical error were used for the fit, this explains the high χ^2 in the low z intervals were the statistical error is very small.

Bin	$\langle z^2 \rangle_{h^+}$	$\langle P_T^2 \rangle_{h^+}$	A_{h^+}	$\chi^2_{h^+}/ndf$	$\langle z^2 \rangle_{h^-}$	$\langle P_T^2 \rangle_{h^-}$	$A_{h^{-}}$	$\chi^2_{h^-}/ndf$
111	0.05	0.23 ± 0.008	9.23 ± 0.085	2.7	0.05	0.23 ± 0.008	8.55 ± 0.080	2.0
112	0.07	0.25 ± 0.010	5.89 ± 0.065	0.8	0.07	0.26 ± 0.010	5.18 ± 0.060	1.6
113	0.11	0.28 ± 0.012	3.73 ± 0.050	1.1	0.11	0.29 ± 0.014	3.23 ± 0.047	1.4
114	0.14	0.30 ± 0.016	2.48 ± 0.040	1.5	0.14	0.31 ± 0.017	2.18 ± 0.037	1.3
115	0.20	0.35 ± 0.016	1.41 ± 0.021	1.1	0.20	0.34 ± 0.017	1.20 ± 0.019	0.8
116	0.30	0.42 ± 0.026	0.64 ± 0.014	1.0	0.30	0.38 ± 0.026	0.57 ± 0.013	1.0
117	0.42	0.42 ± 0.034	0.35 ± 0.010	1.6	0.42	0.42 ± 0.039	0.29 ± 0.009	1.5
118	0.56	0.54 ± 0.063	0.18 ± 0.007	2.1	0.56	0.38 ± 0.048	0.18 ± 0.008	1.3

Table C.12: Fit results for $0.018 < x_{Bj} < 0.025$ and $3.5 < Q^2 < 5 \text{ (GeV/c)}^2$. All variables are defined in the text except $A_{h^{+,-}}$, the fitted Gaussian amplitude. Only statistical error were used for the fit, this explains the high χ^2 in the low z intervals were the statistical error is very small.

Bin	$\langle z^2 \rangle_{h^+}$	$\langle P_T^2 \rangle_{h^+}$	A_{h^+}	$\chi^2_{h^+}/ndf$	$\langle z^2 \rangle_{h^-}$	$\langle P_T^2 \rangle_{h^-}$	A_{h^-}	$\chi^2_{h^-}/ndf$
121	0.05	0.18 ± 0.007	14.09 ± 0.093	7.1	0.05	0.17 ± 0.007	12.28 ± 0.086	10.1
122	0.08	0.20 ± 0.007	9.70 ± 0.069	7.9	0.08	0.19 ± 0.007	8.34 ± 0.064	7.2
123	0.11	0.23 ± 0.007	6.93 ± 0.053	6.8	0.11	0.22 ± 0.008	5.77 ± 0.050	3.3
124	0.14	0.26 ± 0.009	4.97 ± 0.042	3.1	0.14	0.24 ± 0.009	4.16 ± 0.040	2.1
125	0.20	0.29 ± 0.008	3.17 ± 0.023	1.8	0.20	0.26 ± 0.008	2.66 ± 0.022	2.3
126	0.30	0.30 ± 0.010	1.91 ± 0.017	3.2	0.30	0.26 ± 0.010	1.63 ± 0.017	2.1
127	0.42	0.30 ± 0.012	1.26 ± 0.014	3.0	0.42	0.25 ± 0.012	1.11 ± 0.014	6.6
128	0.56	0.27 ± 0.014	0.90 ± 0.012	6.1	0.56	0.21 ± 0.014	0.90 ± 0.014	6.1

Table C.13: Fit results for $0.025 < x_{Bj} < 0.035$ and $1 < Q^2 < 1.2$. All variables are defined in the text except $A_{h^{+,-}}$, the fitted Gaussian amplitude. Only statistical error were used for the fit, this explains the high χ^2 in the low z intervals were the statistical error is very small.

Bin	$\langle z^2 \rangle_{h^+}$	$\langle P_T^2 \rangle_{h^+}$	A_{h^+}	$\chi^2_{h^+}/ndf$	$\langle z^2 \rangle_{h^-}$	$\langle P_T^2 \rangle_{h^-}$	A_{h^-}	$\chi^2_{h^-}/ndf$
131	0.05	0.19 ± 0.005	14.02 ± 0.067	13.3	0.05	0.18 ± 0.005	12.01 ± 0.062	8.1
132	0.08	0.22 ± 0.005	9.35 ± 0.050	5.3	0.08	0.21 ± 0.006	7.96 ± 0.046	5.0
133	0.11	0.24 ± 0.006	6.55 ± 0.039	4.1	0.11	0.23 ± 0.006	5.54 ± 0.036	2.0
134	0.14	0.26 ± 0.007	4.73 ± 0.032	3.6	0.14	0.25 ± 0.008	3.83 ± 0.029	2.0
135	0.20	0.29 ± 0.006	2.93 ± 0.017	1.8	0.20	0.27 ± 0.007	2.42 ± 0.016	2.0
136	0.30	0.31 ± 0.008	1.69 ± 0.012	3.0	0.30	0.28 ± 0.008	1.38 ± 0.012	2.1
137	0.42	0.31 ± 0.010	1.05 ± 0.010	4.4	0.42	0.26 ± 0.010	0.91 ± 0.010	5.4
138	0.56	0.28 ± 0.011	0.77 ± 0.009	6.3	0.56	0.22 ± 0.012	0.71 ± 0.009	8.5

Table C.14: Fit results for $0.025 < x_{Bj} < 0.04$ and $1.2 < Q^2 < 1.5 \text{ (GeV/c)}^2$. All variables are defined in the text except $A_{h^{+,-}}$, the fitted Gaussian amplitude. Only statistical error were used for the fit, this explains the high χ^2 in the low z intervals were the statistical error is very small.

Bin	$\langle z^2 \rangle_{h^+}$	$\langle P_T^2 \rangle_{h^+}$	A_{h^+}	$\chi^2_{h^+}/ndf$	$\langle z^2 \rangle_{h^-}$	$\langle P_T^2 \rangle_{h^-}$	$A_{h^{-}}$	$\chi^2_{h^-}/ndf$
141	0.05	0.21 ± 0.003	13.07 ± 0.042	6.7	0.05	0.21 ± 0.003	11.39 ± 0.040	5.3
142	0.08	0.24 ± 0.003	8.44 ± 0.032	3.6	0.07	0.23 ± 0.004	7.26 ± 0.030	3.3
143	0.11	0.26 ± 0.004	5.71 ± 0.025	1.5	0.11	0.25 ± 0.005	4.74 ± 0.023	2.1
144	0.14	0.28 ± 0.005	3.98 ± 0.021	1.9	0.14	0.27 ± 0.006	3.22 ± 0.019	2.3
145	0.20	0.30 ± 0.005	2.37 ± 0.011	2.0	0.20	0.30 ± 0.005	1.88 ± 0.010	3.0
146	0.30	0.33 ± 0.007	1.27 ± 0.008	3.0	0.30	0.31 ± 0.007	1.01 ± 0.007	3.8
147	0.42	0.34 ± 0.009	0.75 ± 0.006	5.0	0.42	0.30 ± 0.009	0.62 ± 0.006	5.1
148	0.56	0.30 ± 0.010	0.51 ± 0.005	9.1	0.56	0.25 ± 0.010	0.46 ± 0.005	8.7

Table C.15: Fit results for $0.025 < x_{Bj} < 0.04$ and $1.5 < Q^2 < 2.5 \text{ (GeV/c)}^2$. All variables are defined in the text except $A_{h^{+,-}}$, the fitted Gaussian amplitude. Only statistical error were used for the fit, this explains the high χ^2 in the low z intervals were the statistical error is very small.

Bin	$\langle z^2 \rangle_{h^+}$	$\langle P_T^2 \rangle_{h^+}$	A_{h^+}	$\chi^2_{h^+}/ndf$	$\langle z^2 \rangle_{h^-}$	$\langle P_T^2 \rangle_{h^-}$	A_{h^-}	$\chi^2_{h^-}/ndf$
151	0.05	0.22 ± 0.004	11.55 ± 0.057	3.1	0.05	0.22 ± 0.005	10.37 ± 0.054	2.6
152	0.07	0.24 ± 0.005	7.41 ± 0.044	2.5	0.07	0.25 ± 0.006	6.35 ± 0.041	2.6
153	0.11	0.27 ± 0.007	4.88 ± 0.035	1.0	0.10	0.27 ± 0.007	4.11 ± 0.032	1.0
154	0.14	0.29 ± 0.008	3.33 ± 0.028	0.7	0.14	0.29 ± 0.009	2.69 ± 0.025	2.0
155	0.20	0.32 ± 0.008	1.94 ± 0.015	1.6	0.20	0.33 ± 0.009	1.48 ± 0.013	1.3
156	0.30	0.36 ± 0.012	0.96 ± 0.010	1.1	0.30	0.35 ± 0.013	0.73 ± 0.009	1.2
157	0.42	0.37 ± 0.016	0.53 ± 0.007	0.9	0.42	0.35 ± 0.018	0.42 ± 0.007	1.6
158	0.56	0.34 ± 0.020	0.34 ± 0.006	2.9	0.56	0.30 ± 0.020	0.29 ± 0.006	2.5

Table C.16: Fit results for $0.025 < x_{Bj} < 0.04$ and $2.5 < Q^2 < 3.5 \text{ (GeV/c)}^2$. All variables are defined in the text except $A_{h^{+,-}}$, the fitted Gaussian amplitude. Only statistical error were used for the fit, this explains the high χ^2 in the low z intervals were the statistical error is very small.

Bin	$\langle z^2 \rangle_{h^+}$	$\langle P_T^2 \rangle_{h^+}$	A_{h^+}	$\chi^2_{h^+}/ndf$	$\langle z^2 \rangle_{h^-}$	$\langle P_T^2 \rangle_{h^-}$	$A_{h^{-}}$	$\chi^2_{h^-}/ndf$
161	0.05	0.23 ± 0.004	10.66 ± 0.056	5.1	0.05	0.23 ± 0.005	9.42 ± 0.052	5.8
162	0.08	0.25 ± 0.006	6.78 ± 0.043	2.2	0.07	0.26 ± 0.006	5.80 ± 0.040	2.4
163	0.11	0.28 ± 0.007	4.38 ± 0.034	1.2	0.10	0.28 ± 0.008	3.58 ± 0.031	2.5
164	0.14	0.31 ± 0.009	2.89 ± 0.027	1.4	0.14	0.31 ± 0.010	2.31 ± 0.024	0.6
165	0.20	0.35 ± 0.009	1.58 ± 0.014	0.8	0.20	0.35 ± 0.010	1.26 ± 0.012	1.4
166	0.30	0.41 ± 0.015	0.76 ± 0.009	1.6	0.30	0.40 ± 0.017	0.57 ± 0.008	1.3
167	0.42	0.43 ± 0.021	0.39 ± 0.007	1.2	0.42	0.39 ± 0.022	0.31 ± 0.006	1.4
168	0.56	0.38 ± 0.027	0.24 ± 0.005	2.3	0.56	0.34 ± 0.028	0.20 ± 0.005	2.1

Table C.17: Fit results for $0.025 < x_{Bj} < 0.04$ and $3.5 < Q^2 < 6 \text{ (GeV/c)}^2$. All variables are defined in the text except $A_{h^{+,-}}$, the fitted Gaussian amplitude. Only statistical error were used for the fit, this explains the high χ^2 in the low z intervals were the statistical error is very small.

Bin	$\langle z^2 \rangle_{h^+}$	$\langle P_T^2 \rangle_{h^+}$	A_{h^+}	$\chi^2_{h^+}/ndf$	$\langle z^2 \rangle_{h^-}$	$\langle P_T^2 \rangle_{h^-}$	A_{h^-}	$\chi^2_{h^-}/ndf$
171	0.05	0.18 ± 0.005	14.42 ± 0.080	12.6	0.05	0.18 ± 0.005	12.31 ± 0.074	4.4
172	0.08	0.21 ± 0.006	9.82 ± 0.060	5.2	0.08	0.20 ± 0.006	8.15 ± 0.055	3.5
173	0.11	0.24 ± 0.007	6.78 ± 0.047	1.9	0.11	0.23 ± 0.007	5.46 ± 0.043	3.7
174	0.14	0.25 ± 0.008	4.92 ± 0.038	1.8	0.14	0.24 ± 0.008	3.93 ± 0.035	1.3
175	0.20	0.29 ± 0.007	2.98 ± 0.020	1.7	0.20	0.27 ± 0.008	2.32 ± 0.018	2.1
176	0.30	0.32 ± 0.010	1.62 ± 0.014	2.1	0.30	0.28 ± 0.010	1.28 ± 0.013	2.5
177	0.42	0.33 ± 0.012	0.97 ± 0.010	2.1	0.42	0.29 ± 0.013	0.76 ± 0.010	3.4
178	0.56	0.30 ± 0.014	0.67 ± 0.009	2.9	0.56	0.24 ± 0.014	0.59 ± 0.009	3.4

Table C.18: Fit results for $0.04 < x_{Bj} < 0.05$ and $1.5 < Q^2 < 2.5 \text{ (GeV/c)}^2$. All variables are defined in the text except $A_{h^{+,-}}$, the fitted Gaussian amplitude. Only statistical error were used for the fit, this explains the high χ^2 in the low z intervals were the statistical error is very small.

Bin	$\langle z^2 \rangle_{h^+}$	$\langle P_T^2 \rangle_{h^+}$	A_{h^+}	$\chi^2_{h^+}/ndf$	$\langle z^2 \rangle_{h^{-}}$	$\langle P_T^2 \rangle_{h^-}$	$A_{h^{-}}$	$\chi^2_{h^-}/ndf$
181	0.05	0.20 ± 0.004	13.70 ± 0.067	5.1	0.05	0.19 ± 0.005	11.76 ± 0.063	2.5
182	0.08	0.22 ± 0.005	8.93 ± 0.050	2.4	0.07	0.22 ± 0.006	7.47 ± 0.047	3.1
183	0.11	0.25 ± 0.006	6.01 ± 0.039	1.8	0.11	0.25 ± 0.007	4.82 ± 0.035	1.7
184	0.14	0.27 ± 0.007	4.14 ± 0.031	1.4	0.14	0.27 ± 0.008	3.13 ± 0.027	0.9
185	0.20	0.31 ± 0.007	2.40 ± 0.016	1.1	0.20	0.30 ± 0.008	1.77 ± 0.014	2.7
186	0.30	0.34 ± 0.010	1.24 ± 0.011	1.6	0.30	0.33 ± 0.012	0.88 ± 0.010	1.8
187	0.42	0.37 ± 0.013	0.68 ± 0.008	1.8	0.42	0.33 ± 0.015	0.50 ± 0.007	1.4
188	0.56	0.36 ± 0.017	0.43 ± 0.006	2.8	0.56	0.29 ± 0.018	0.34 ± 0.006	2.6

Table C.19: Fit results for $0.04 < x_{Bj} < 0.07$ and $2.5 < Q^2 < 3.5 \, (\text{GeV/c})^2$. All variables are defined in the text except $A_{h^{+,-}}$, the fitted Gaussian amplitude. Only statistical error were used for the fit, this explains the high χ^2 in the low z intervals were the statistical error is very small.

Bin	$\langle z^2 \rangle_{h^+}$	$\langle P_T^2 \rangle_{h^+}$	A_{h^+}	$\chi^2_{h^+}/ndf$	$\langle z^2 \rangle_{h^-}$	$\langle P_T^2 \rangle_{h^-}$	A_{h^-}	$\chi^2_{h^-}/ndf$
191	0.05	0.22 ± 0.004	12.22 ± 0.052	2.4	0.05	0.22 ± 0.004	10.60 ± 0.049	4.2
192	0.08	0.24 ± 0.005	7.82 ± 0.039	1.2	0.07	0.25 ± 0.005	6.40 ± 0.036	1.8
193	0.11	0.27 ± 0.006	5.07 ± 0.030	0.9	0.10	0.28 ± 0.007	3.94 ± 0.027	1.7
194	0.14	0.29 ± 0.007	3.40 ± 0.024	1.3	0.14	0.30 ± 0.008	2.55 ± 0.021	1.2
195	0.20	0.34 ± 0.007	1.91 ± 0.012	1.1	0.20	0.34 ± 0.008	1.38 ± 0.011	1.9
196	0.30	0.40 ± 0.011	0.91 ± 0.008	1.3	0.30	0.37 ± 0.012	0.66 ± 0.007	1.2
197	0.42	0.42 ± 0.015	0.48 ± 0.006	1.1	0.42	0.39 ± 0.018	0.33 ± 0.005	1.2
198	0.56	0.40 ± 0.019	0.29 ± 0.005	0.9	0.56	0.34 ± 0.022	0.21 ± 0.004	1.7

Table C.20: Fit results for $0.04 < x_{Bj} < 0.07$ and $3.5 < Q^2 < 6 \text{ (GeV/c)}^2$. All variables are defined in the text except $A_{h^{+,-}}$, the fitted Gaussian amplitude. Only statistical error were used for the fit, this explains the high χ^2 in the low z intervals were the statistical error is very small.

Bin	$\langle z^2 \rangle_{h^+}$	$\langle P_T^2 \rangle_{h^+}$	A_{h^+}	$\chi^2_{h^+}/ndf$	$\langle z^2 \rangle_{h^{-}}$	$\langle P_T^2 \rangle_{h^-}$	$A_{h^{-}}$	$\chi^2_{h^-}/ndf$
201	0.05	0.23 ± 0.006	10.75 ± 0.070	3.6	0.05	0.24 ± 0.006	9.22 ± 0.064	2.5
202	0.07	0.26 ± 0.007	6.77 ± 0.053	1.5	0.07	0.27 ± 0.008	5.45 ± 0.047	1.5
203	0.10	0.29 ± 0.009	4.28 ± 0.041	1.5	0.10	0.30 ± 0.010	3.32 ± 0.035	0.9
204	0.14	0.32 ± 0.012	2.77 ± 0.032	1.4	0.14	0.32 ± 0.014	2.10 ± 0.028	1.5
205	0.20	0.36 ± 0.011	1.57 ± 0.016	1.0	0.20	0.37 ± 0.014	1.09 ± 0.014	1.9
206	0.30	0.43 ± 0.019	0.71 ± 0.010	1.6	0.30	0.42 ± 0.023	0.49 ± 0.009	0.9
207	0.42	0.49 ± 0.029	0.35 ± 0.007	1.9	0.42	0.41 ± 0.031	0.26 ± 0.006	1.3
208	0.56	0.51 ± 0.041	0.18 ± 0.005	1.4	0.56	0.39 ± 0.042	0.14 ± 0.005	1.2

Table C.21: Fit results for $0.04 < x_{Bj} < 0.07$ and $6 < Q^2 < 10 \ (\text{GeV/c})^2$. All variables are defined in the text except $A_{h^{+,-}}$, the fitted Gaussian amplitude. Only statistical error were used for the fit, this explains the high χ^2 in the low z intervals were the statistical error is very small.

Bin	$\langle z^2 \rangle_{h^+}$	$\langle P_T^2 \rangle_{h^+}$	A_{h^+}	$\chi^2_{h^+}/ndf$	$\langle z^2 \rangle_{h^{-}}$	$\langle P_T^2 \rangle_{h^-}$	A_{h^-}	$\chi^2_{h^-}/ndf$
211	0.05	0.18 ± 0.004	14.59 ± 0.076	8.2	0.05	0.18 ± 0.005	11.79 ± 0.069	6.7
212	0.08	0.20 ± 0.005	9.64 ± 0.056	6.1	0.08	0.20 ± 0.006	7.49 ± 0.050	3.1
213	0.11	0.23 ± 0.006	6.30 ± 0.043	3.1	0.11	0.23 ± 0.007	4.60 ± 0.037	3.1
214	0.14	0.26 ± 0.007	4.38 ± 0.034	1.4	0.14	0.27 ± 0.009	3.01 ± 0.028	2.7
215	0.20	0.30 ± 0.007	2.53 ± 0.017	2.5	0.20	0.29 ± 0.009	1.70 ± 0.014	2.0
216	0.30	0.35 ± 0.010	1.27 ± 0.012	2.0	0.30	0.32 ± 0.013	0.82 ± 0.009	1.1
217	0.42	0.38 ± 0.015	0.67 ± 0.008	1.5	0.42	0.36 ± 0.018	0.41 ± 0.007	1.4
218	0.56	0.38 ± 0.019	0.39 ± 0.006	1.8	0.56	0.33 ± 0.022	0.26 ± 0.005	1.4

Table C.22: Fit results for $0.07 < x_{Bj} < 0.12$ and $3.5 < Q^2 < 6 \text{ (GeV/c)}^2$. All variables are defined in the text except $A_{h^{+,-}}$, the fitted Gaussian amplitude. Only statistical error were used for the fit, this explains the high χ^2 in the low z intervals were the statistical error is very small.

Bin	$\langle z^2 \rangle_{h^+}$	$\langle P_T^2 \rangle_{h^+}$	A_{h^+}	$\chi^2_{h^+}/ndf$	$\langle z^2 \rangle_{h^-}$	$\langle P_T^2 \rangle_{h^-}$	$A_{h^{-}}$	$\chi^2_{h^-}/ndf$
221	0.05	0.21 ± 0.005	12.90 ± 0.072	2.9	0.05	0.22 ± 0.005	10.38 ± 0.064	3.6
222	0.08	0.25 ± 0.006	7.95 ± 0.052	1.7	0.07	0.25 ± 0.007	6.23 ± 0.046	1.9
223	0.11	0.27 ± 0.008	5.27 ± 0.041	1.7	0.10	0.28 ± 0.009	3.76 ± 0.034	1.0
224	0.14	0.30 ± 0.009	3.46 ± 0.032	1.7	0.14	0.30 ± 0.011	2.40 ± 0.026	0.8
225	0.20	0.34 ± 0.009	1.94 ± 0.016	1.4	0.20	0.35 ± 0.012	1.24 ± 0.013	0.8
226	0.30	0.41 ± 0.014	0.91 ± 0.010	0.6	0.30	0.40 ± 0.018	0.56 ± 0.008	0.6
227	0.42	0.47 ± 0.021	0.45 ± 0.007	1.0	0.42	0.41 ± 0.026	0.28 ± 0.006	1.3
228	0.56	0.47 ± 0.029	0.25 ± 0.005	1.1	0.56	0.39 ± 0.034	0.15 ± 0.004	1.8

Table C.23: Fit results for $0.07 < x_{Bj} < 0.12$ and $6 < Q^2 < 10 \ (\text{GeV/c})^2$. All variables are defined in the text except $A_{h^{+,-}}$, the fitted Gaussian amplitude. Only statistical error were used for the fit, this explains the high χ^2 in the low z intervals were the statistical error is very small.

Appendix D

Acronyms and Abbreviations

CATCH COMPASS Accumulate, Transfer and Control Hardware

- CEA Cambridge Electron Accelerator
- CERN European Organization for Nuclear Research (originally: Conseil Europén pour la Recherche Nucléaire)
- CHEOPS CHarm Experiment with Omni-Purpose Setup
- COMPASS COmmon Muon and Proton Apparatus for Structure and Spectroscopy
 - DAQ Data acquisition system
 - DESY Deutsches Elektronen-Synchrotron
 - DIS Deep inelastic scattering
 - EB Event builder
 - ECAL Electromagnetic calorimeter
 - EMC European Muon Collaboration
 - FF Fragmentation function
 - GeSiCA GEM and Silicon Control and Acquisition
 - GPD Generalized parton distribution functions
 - HCAL Hadronic calorimeter
 - HMC Hadron Muon Collaboration
 - inclMT Inclusive middle trigger
 - JLab Jefferson laboratory

LAS	Large angle spectrometer
LO	Leading order
MC	Monte Carlo
mDST	mini Data Summary Tape
ME	Matrix element
MWPC	Multiwire proportional chamber
NMC	New Muon Collaboration
PDF	Parton Distribution Function
PGF	Photon Gluon Fusion
PHAST	PHysics Analysis Software Tools
pQCD	perturbative Quantum ChromoDynamics
QCD	Quantum ChromoDynamics
QED	Quantum ElectroDynamics
QPM	Quark parton model
RICH	Ring imaging Cherenkov (detector)
ROB	Readout buffer
SAS	Small angle spectrometer
SciFi	Scintillating fiber
SIDIS	semi-inclusive Deep inelastic scattering
SLAC	Stanford Linear Accelerator Center
SMC	Spin Muon Collaboration
SPS	Super Proton Synchrotron (at CERN)
TCS	Trigger control system
TDC	Time to digital converter
TMD	Transverse momentum distribution

Bibliography

- [1] Comgeant homepage. http://valexakh.web.cern.ch/valexakh/wwwcomg/index.html.
- [2] Coral homepage. http://coral.web.cern.ch/coral/.
- [3] Geant homepage. http://wwwasd.web.cern.ch/wwwasd/geant/index.html.
- [4] Root homepage. http://root.cern.ch/.
- [5] K. Abe et al. Measurements of R = sigma(L)/sigma(T) for 0.03 < x < 0.1 and fit to world data. *Phys. Lett.*, B452:194–200, 1999.
- [6] B. Adeva et al. Spin asymmetries A(1) and structure functions g1 of the proton and the deuteron from polarized high energy muon scattering. *Phys. Rev.*, D58:112001, 1998.
- [7] E. S. Ageev et al. Gluon polarization in the nucleon from quasi-real photoproduction of high-p(T) hadron pairs. *Phys. Lett.*, B633:25–32, 2006.
- [8] E. S. Ageev et al. A new measurement of the Collins and Sivers asymmetries on a transversely polarised deuteron target. *Nucl. Phys.*, B765:31–70, 2007.
- [9] A. Alekseev. Observation of a $J^{PC} = 1^{-+}$ exotic resonance in diffractive dissociation of 190 GeV/c π^- into $\pi^- \pi^- \pi^+$. 2009.
- [10] M. Alekseev et al. The Polarised Valence Quark Distribution from semi- inclusive DIS. *Phys. Lett.*, B660:458–465, 2008.
- [11] M. Alekseev et al. Collins and Sivers asymmetries for pions and kaons in muondeuteron DIS. *Phys. Lett.*, B673:127–135, 2009.
- [12] M. Alekseev et al. Flavour Separation of Helicity Distributions from Deep Inelastic Muon-Deuteron Scattering. *Phys. Lett.*, B680:217–224, 2009.
- [13] M G Alekseev et al. Measurement of the Collins and Sivers asymmetries on transversely polarised protons. 2010.
- [14] V. Yu. Alexakhin et al. The Deuteron Spin-dependent Structure Function g1d and its First Moment. *Phys. Lett.*, B647:8–17, 2007.

- [15] Bo Andersson, G. Gustafson, G. Ingelman, and T. Sjostrand. Parton Fragmentation and String Dynamics. *Phys. Rept.*, 97:31–145, 1983.
- [16] M. Anselmino, M. Boglione, A. Prokudin, and C. Turk. Semi-inclusive deep inelastic scattering processes from small to large P(T). *Eur. Phys. J.*, A31:373–381, 2007.
- [17] M. Anselmino et al. The role of Cahn and Sivers effects in deep inelastic scattering. *Phys. Rev.*, D71:074006, 2005.
- [18] M. Arneodo et al. Measurement of the proton and the deuteron structure functions, F2(p) and F2(d). Phys. Lett., B364:107–115, 1995.
- [19] M. Arneodo et al. Measurement of the proton and deuteron structure functions, F2(p) and F2(d), and of the ratio sigma(L)/sigma(T). Nucl. Phys., B483:3–43, 1997.
- [20] J. Ashman et al. A measurement of the spin asymmetry and determination of the structure function g(1) in deep inelastic muon proton scattering. *Phys. Lett.*, B206:364, 1988.
- [21] J. Ashman et al. Forward produced hadrons in mu p and mu d scattering and investigation of the charge structure of the nucleon. Z. Phys., C52:361–388, 1991.
- [22] J. J. Aubert et al. Transverse momentum of charged hadrons observed in deep inelastic muon scattering. *Phys. Lett.*, B95:306, 1980.
- [23] Alessandro Bacchetta. What can we learn from TMD measurements? AIP Conf. Proc., 1149:447–452, 2009.
- [24] B. Badelek, Dmitri Yu. Bardin, K. Kurek, and C. Scholz. Radiative correction schemes in deep inelastic muon scattering. Z. Phys., C66:591–600, 1995.
- [25] Guenter Baum et al. COMPASS: A Proposal for a Common Muon and Proton Apparatus for Structure and Spectroscopy. 1996. CERN-SPSLC-96-14.
- [26] Mats Bengtsson and Torbjorn Sjostrand. PARTON SHOWERS IN LEPTOPRO-DUCTION EVENTS. Z. Phys., C37:465, 1988.
- [27] J. D. Bjorken. Asymptotic Sum Rules at Infinite Momentum. Phys. Rev., 179:1547– 1553, 1969.
- [28] V. N. Bychkov et al. The large size straw drift chambers of the COMPASS experiment. Nucl. Instrum. Meth., A556:66–79, 2006.
- [29] Robert N. Cahn. Azimuthal Dependence in Leptoproduction: A Simple Parton Model Calculation. *Phys. Lett.*, B78:269, 1978.
- [30] Federico A. Ceccopieri and Luca Trentadue. An application of transverse-momentumdependent evolution equations in QCD. *Phys. Lett.*, B660:43–48, 2008.

- [31] John C. Collins. Fragmentation of transversely polarized quarks probed in transverse momentum distributions. Nucl. Phys., B396:161–182, 1993.
- [32] Daniel de Florian, Rodolfo Sassot, and Marco Stratmann. Global analysis of fragmentation functions for pions and kaons and their uncertainties. *Phys. Rev.*, D75:114010, 2007.
- [33] David M. Dennison. A Note on the Specific Heat of the Hydrogen Molecule. Proc. R. Soc., A115:483–486, 1927.
- [34] Markus Diefenthaler. HERMES measurements of Collins and Sivers asymmetries from a transversely polarised hydrogen target. Munich 2007, Deep-inelastic scattering, pages 579–582, 2007.
- [35] N. Doble, L. Gatignon, G. von Holtey, and F. Novoskoltsev. The Upgraded muon beam at the SPS. Nucl. Instrum. Meth., A343:351–362, 1994.
- [36] E. Nappi et al. Semi-inclusive muon scattering from a polarised target. 1995. CERN-SPSLC-95-27. SPSLC-I-202.
- [37] Y. Bedfer et al. Memorandum, 2008. COMPASS High pt group note.
- [38] Yu.Alexandrow et al. Charm experiment with omnipurpose setup. 1996. CERN-SPSLC-96-14.
- [39] S. Koblitz F.-H. Heinsius. Compass luminosity for 2002-2004, 2006. COMPASS note 2006-5.
- [40] Jerome I. Friedman. Deep inelastic scattering: Comparisons with the quark model. *Rev. Mod. Phys.*, 63:615–629, 1991.
- [41] L. Gatignon. M2 user guide. http://gatignon.web.cern.ch/gatignon/M2manual.html.
- [42] S. Gerassimov. Phast homepage. http://ges.web.cern.ch/ges/phast/.
- [43] Transversity group. Collins and sivers asymmetries from 2007 proton transverse run, 2008. COMPASS note 2008-10.
- [44] A. Guskov. Analysis of the charged pion polarizability measurement method at COM-PASS experiment. PhD thesis, Universita degli Studi di Torino, 2010.
- [45] Francis Halzen and Alan Douglas Martin. Quarks and leptons: an introductory course in modern particle physics. Wiley, New York, NY, 1984.
- [46] G. Ingelman, A. Edin, and J. Rathsman. LEPTO 6.5 A Monte Carlo Generator for Deep Inelastic Lepton-Nucleon Scattering. Comput. Phys. Commun., 101:108–134, 1997.

- [47] Anton Jgoun. Measurement of the z- and x-dependence of the mean transverse momentum of charged hadrons, charged pions and K0(S) at HERMES. 2001.
- [48] W. Kaefer. Measurements of Unpolarized Azimuthal Asymmetries at COMPASS. Proceedings of Transversity 2008: 2nd International Workshop on Transverse Polarization Phenomena in Hard Processes, 2008.
- [49] H. W. Kendall. Deep inelastic scattering: Experiments on the proton and the observation of scaling. In *Fraengsmyr, T. (ed.), Ekspong, G. (ed.): Nobel lectures* 676-708.
- [50] Bernd A. Kniehl, G. Kramer, and B. Potter. Fragmentation functions for pions, kaons, and protons at next-to-leading order. *Nucl. Phys.*, B582:514–536, 2000.
- [51] S. Koblitz. Determination of the Gluon Polarisation from Open Charm Production at COMPASS. PhD thesis, Johannes Gutenberg-Universitt Mainz, 2008.
- [52] A. D. Martin, W. J. Stirling, and R. S. Thorne. MRST partons generated in a fixed-flavour scheme. *Phys. Lett.*, B636:259–264, 2006.
- [53] H. Mkrtchyan et al. Transverse momentum dependence of semi-inclusive pion production. *Phys. Lett.*, B665:20–25, 2008.
- [54] K. Platzer. Ein Roentgen-CCD Apparat zur Eichung grossflaechiger Driftkammern. PhD thesis, Fakultaet fuer Physik der Lugwig-Maximilians-Universitaet Muenchen, 2004.
- [55] S. Procureur. Détermination de la polarisation des gluons dans le nucléon par la production de hadrons à grande implusion transverse à COMPASS. PhD thesis, Université Paris XI, 2006.
- [56] J.F. Rajotte and M. Faessler. COMPASS' inclusive cross section $\mu N \rightarrow \mu' N$ for $Q^2 > 1 \,(\text{GeV/c})^2$, 2008. COMPASS note 2008-6.
- [57] J.F. Rajotte and A. Zvyagin. Time calibration of individual readout cards of straw drift chambers, 2007. COMPASS note 2007-11.
- [58] Marta Sans Merce. Development of drift chambers and physics simulations for the COMPASS experiment. PhD thesis, Fakultaet fuer Physik der Lugwig-Maximilians-Universitaet Muenchen, 2001.
- [59] Gunar Schnell. GMC TRANS, A Monte Carlo Generator for TMDs. *PKU-RBRC* Workshop on Transverse Spin Physics, 2008.
- [60] P. Schweitzer, T. Teckentrup, and A. Metz. Intrinsic transverse parton momenta in deeply inelastic reactions. *Phys. Rev.*, D81:094019, 2010.

- [61] Dennis W. Sivers. Single Spin Production Asymmetries from the Hard Scattering of Point-Like Constituents. *Phys. Rev.*, D41:83, 1990.
- [62] Richard E. Taylor. Deep inelastic scattering: The Early years. *Rev. Mod. Phys.*, 63:573–595, 1991.

Danksagung

I would first like to thank my *Doktorvater*, Professor Martin Faessler, who I first met at a Summer School in Munich six years ago... already! I learned very much from him, maybe the most important is to be a physicist in the society. I also want to acknowledge the first two persons I worked with in particle physics, Reiner Geyer and Alexander "Sasha" Yurievich Zvyagin. I was lucky to share my office at CERN with Sasha who joyfully introduced to the computing world the barely-able-to-switch-on-a-computer man that I was.

There are many people who helped me produce the results presented in this thesis. The most notable ones are Aram Kotzinian, Yann Bedfer, the high-pt group (especially Konrad Klimaszewski) and Nour Makke. Outside COMPASS, I am grateful for the nice discussions and email exchanges with Dr. Alessandro Bacchetta who helped me interpret my results.

I also want to thank my colleagues from Garching who allowed me to practice my German during lunch time. I have appreciated their tolerance regarding my lack of capability to understand German humor (I am getting there). In particular, I would like to thank Meike Dlaboha who eased the difficulties of a foreigner making its way through cryptic bureaucracy. In my Garching office, I enjoyed the company of two nice Diploma students, Sabine and Hauke, who taught me all sorts of cultural references, most notably the *Rumpelstilzchen*. I will miss the beloved sciacquone breaks with my fellow *Kommilitone*, Massimo and Tobias.

At last, I would like to thank Christiana for our time in Geneva. You helped me forget the rough patches. Allez petite, on a presque tenu le coup, c'est déjà pas pire.

Comment ça vaut, ça... calcule! Chu déjà millionnaire.¹

¹ "...et j'ai couché dans mon char", Richard Desjardins

Lebenslauf

Persönliche Daten

NameRajotteVornameJean-FrançoisGeburtsdatum03. Januar 1978

Geburtsort Sherbrooke, Québec, Kanada

Werdegang

- 1999-2002 Physik-Studium (Bachelor) an der Université de Montréal
- 2003-2005 Physik-Studium (Master) an der Université de Montréal
- 2005-2010 Wissenschaftlicher Mitarbeiter der Ludwig-Maximilians-Universität München, davon die ersten 2 Jahre an das CERN in Genf abgeordnet